

AD-A169 947

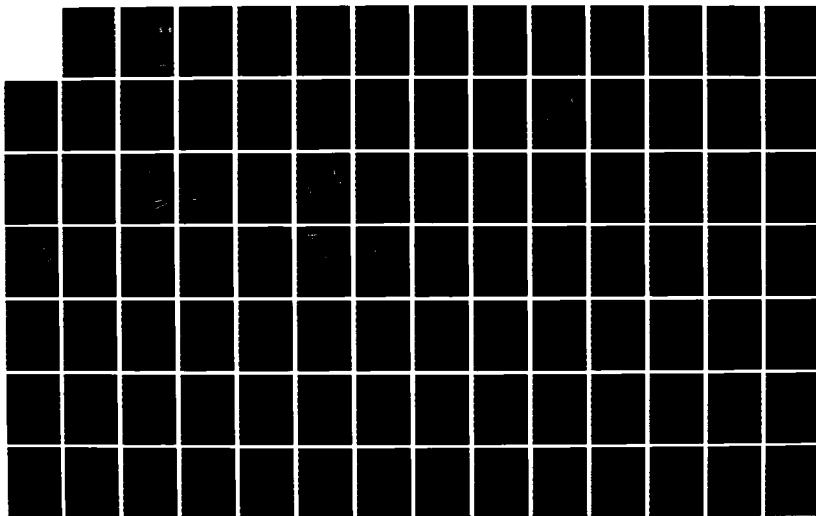
TECHNICAL REQUIREMENTS FOR BENCHMARK SIMULATOR-BASED
TERMINAL INSTRUMENT. (U) ANALYTICAL MECHANICS
ASSOCIATES INC MOUNTAIN VIEW CA A V PHATAK ET AL.

1/2

UNCLASSIFIED

MAY 86 AHA-86-2-1 NASA-CR-177407 NAS2-11973 F/G 17/7

NL





1.0



1.1



1.25



1.4



1.6

1.8
2.0
2.2
2.5
2.8
3.15
3.5
4.0
4.5



2.8



2.5



2.2



2.0



1.8

DOT/FAA/PM-86/14
NASA CR-177407

Program Engineering
and Maintenance Service
Washington, D.C. 20591

Technical Requirements for Benchmark Simulator-Based Terminal Instrument Procedures (TERPS) Evaluation

AD-A169 947

DTIC
ELECTE
JUL 23 1986
S D

A.V. Phatak
John A. Sorensen

Analytical Mechanics Associates, Inc.
2483 Old Middlefield Way
Mountain View, California 94035

May 1986

Final Report

This Document is available to the public
through the National Technical Information
Service, Springfield, Virginia 22161.

DTIC FILE COPY

DISTRIBUTION STATEMENT A

Approved for public release
Distribution Unlimited



U.S. Department of Transportation
Federal Aviation Administration



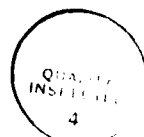
National Aeronautics and
Space Administration

Ames Research Center
Moffett Field, California 94035

1. Report No. DOT/FAA/PM-86/14 NASA CR 177407		2. Government Accession No.		3. Recipient's Catalog No.	
4. Title and Subtitle Technical Requirements for Benchmark Simulator-Based TERPS Evaluation				5. Report Date May, 1986	
				6. Performing Organization Code	
7. Author(s) A. V. Phatak and J. A. Sorensen				8. Performing Organization Report No. AMA Report No. 86-2-I	
				10. Work Unit No.	
9. Performing Organization Name and Address Analytical Mechanics Associates, Inc. 2483 Old Middlefield Way Mountain View, CA 94043				11. Contract or Grant No. NAS 2-11973	
				13. Type of Report and Period Covered Contractor Report	
12. Sponsoring Agency Name and Address NASA-Ames Research Center Moffett Field, CA 94035				FAA Technical Field Office P.O. Box 25 Moffett Field, CA 94035	
14. Sponsoring Agency Code					
15. Supplementary Notes POINT OF CONTACT Barry C. Scott M/S 210-2 FAA/Ames Research Center, Moffett Field, CA 94035 (415) 694-6379 or FTS 464-6379					
16. Abstract In order to take full advantage of the helicopter's unique flight characteristics, enhanced terminal instrument procedures (TERPS) need to be developed for a variety of non-standard operational situations. These include non-standard landing navigation aids, precision and non-precision approach profiles, landing sites, and avionics systems. Currently, TERPS criteria are largely established by extensive flight testing. This study examined the requirements for using helicopter cockpit simulators in place of flight testing to generate data necessary for enhanced TERPS development. Specifically, this report identifies and defines which parts of TERPS may be evaluated with the present state of the art in simulator technology. The report also recommends a test plan for benchmark simulator-based TERPS evaluation of standard ILS and MLS approaches using NASA Ames helicopter simulators. Included as part of this investigation were a survey and summary of the current state in modeling of navigation systems, environmental disturbances and helicopter dynamics plus visual and motion simulation; these summaries are included as appendices.					
17. Key Words (Suggested by Author(s)) TERPS, Helicopter flight cockpit simulator flight test operational approach profiles				18. Distribution Statement UNCLASSIFIED - UNLIMITED STAR CATEGORY 1	
19. Security Classif. (of this report) Unclassified		20. Security Classif. (of this page) Unclassified		21. No. of Pages 115	
22. Price*					

TABLE OF CONTENTS

	Page
INTRODUCTION.....	1
SIMULATION-BASED APPROACH TO TERPS EVALUATION AND ENHANCEMENT	3
TEST PLAN FOR SIMULATOR-BASED TERPS EVALUATION.....	7
CONCLUDING REMARKS.....	13
APPENDIX A NAVIGATION SYSTEMS.....	15
APPENDIX B MODELS FOR ENVIRONMENTAL DISTURBANCES.....	69
APPENDIX C VISUAL SIMULATION.....	93
APPENDIX D MOTION SIMULATION.....	97
APPENDIX E HELICOPTER DYNAMICS.....	105
APPENDIX F PILOT MODELS FOR OFF-LINE TERPS EVALUATION.....	109
REFERENCES.....	111



Accession For	
NTIS CRA&I	<input checked="" type="checkbox"/>
DTIC TAB	<input type="checkbox"/>
Unannounced	<input type="checkbox"/>
Justification	
By	
Distribution /	
Availability Codes	
Dist	Avail and/or Special
A-1	

SYMBOLS AND ABBREVIATIONS

AGL	Above Ground Level
ARC	Ames Research Center
ARWS	Advanced Rotary Wing Simulator
ATE	Along Track Error
C/A CODE	Course/Acquisition Code For GPS
CEP	Circular Error Probability
CTE	Cross Track Error
CTOL	Conventional Take-Off and Landing
CW	Continuous Wave
DFS	Dynamic Flight Simulator
DME	UHF Standard Distance Measuring Equipment
DOF	Degrees of Freedom
DRMS	Diagonal Root Mean Square Error
FAA	Federal Aviation Authority
FLIR	Forward-Looking Infra-Red
FTE	Flight Technical Error
GDOP	Geometrical Dilution of Position
GPS	Global Positioning System
GRI	Group Repetition Interval
G/S	Glideslope
ICAO	International Civil Aviation Organization
IFR	Instrument Flight Rules
ILS	Instrument Landing System
IMC	Instrument Meteorological Conditions
INS	Inertial Navigation System
JAWS	Joint Airport Weather Studies
LAMARS	Large Amplitude Multi-Mode Aerospace Simulator
LOP	Line of Position
MLS	Microwave Landing System
NASA	National Aeronautics and Space Administration
Navaid	Navigation Aid
NCAR	National Center for Atmospheric Research
NOE	Nap-of-the-earth

NSE	Navigation System Error
OM, MM, IM	Outer, Middle, Inner Marker
P Code	Precise Code for GPS
PPS	Precision Positioning Service for GPS (P code)
RFI	Radio Frequency Interference
RODAAS	Rotorcraft Digital Advanced Avionic System
RSIS	Rotorcraft Systems Integrator Simulator
SCAS	Stability and Control Augmentation System
SF, ASF	Secondary factor; additional secondary factor for LORAN-C errors
SMS, LMS	Small and Large Motion Systems
SPS	Standard Positioning Service for GHPS (CA code)
SSV	Standard Service Volumes
STC	Supplemental Type Certificate
TACAN	Tactical Air Navigation System
TD	Time Difference
TERPS	Terminal Instrument Procedures
TSE	Total System Error
VFR	Visual Flight Rules
VLF, VHF	Very Low, Very High Frequency
VMS	Vertical Motion Simulator
VOR	VHF Omnidirectional Radio Range
VORTAC	Colocated VOR and TACAN

INTRODUCTION

The demand for helicopter IFR operations is expected to grow rapidly over the next two decades. However, at the present time, helicopters under Instrument Meteorological Conditions (IMC) are forced to operate as though they were a fixed-wing aircraft, and pilots must abide by the FAA's standard IFR regulations corresponding to the prevailing weather conditions (i.e., ceiling and runway visual range). As a result, current helicopter IFR terminal area operations are limited to conventional runways at airports equipped with the standard 3° glide-slope Instrument Landing System (ILS). However, what distinguishes a helicopter from a conventional take-off and landing (CTOL) aircraft is its ability to climb and descend vertically, and to fly complex, curved, steep descending, and decelerating approach profiles to a hover into confined and unprepared landing sites. It is this unique capability that makes the helicopter such an attractive alternative mode of transportation (and sometimes the only choice) for a host of civilian applications. At present, rotorcraft effectiveness is severely hampered by the constraints imposed by the existing FAA regulations. Therefore, in order to take full advantage of the helicopter's unique characteristics, enhanced terminal instrument procedures (TERPS) need to be developed for a variety of non-standard operational situations, which may arise due to one or more of the following factors:

- o Non-standard landing navigation aids
 - VOR/DME, MLS, GPS, LORAN C, OMEGA
- o Non-standard precision approach profiles
 - Steep glide-slope straight-in approaches
 - Curved path and steep glide-slope approaches
 - Curved path, steep glide-slope and decelerating approaches
- o Non-standard, non-precision, and point-in-space approaches for prescribed visibility minimums and minimum descent altitudes
- o Non-standard landing sites
 - Airport runway adjacent helipads
 - Remote off-shore oil rig platforms
 - Remote and unprepared overland sites
 - City center building top helipads
 - Mountain pinnacle sites
- o Non-standard avionics systems
 - Different types of stability-control augmentation systems (i.e., rate, attitude, velocity, or position SCAS)
 - Different levels of display sophistication (i.e., integrated panel or heads-up electronic displays)

- Different levels of guidance systems (i.e., raw glide-slope/localizer data and advanced 4-cue flight directors)

The current approach towards enhancement of the TERPS operating procedures and criteria for non-standard situations is based upon the analyses of test data obtained from controlled flight investigations, carried out on an individual case basis. For example, since 1979, NASA together with the FAA, has conducted two major flight-test programs to evaluate the effectiveness of the MLS for allowing helicopters to fly non-standard approach profiles.

The first program in 1979-1980 was aimed towards investigating the feasibility of flying 3° , 6° and 9° straight-in MLS approaches, with a Bell UH-1H helicopter, using "raw data" or "angle only" information.^{1,2} The second and most recent test program completed in 1983-1984³⁻⁵ gathered and evaluated test data for 18 pilots flying curved path and steep glide-slope MLS approaches in a UH-1H helicopter using a 3-cue flight director. Three approach profiles--a baseline straight-in steep glide-slope (9° and 12°) approach, a U-turn (6° and 9°) approach and an S-turn (6° and 9°) approach--were selected for operational evaluation. The definition of the approach profile segments and parameters (i.e., intercept or capture angles, lengths of straight-segments, radius of curved segments, etc.) was arrived at by NASA Test Pilots through subjective evaluation during preliminary flight tests. Certain "rules of thumb" or heuristics were developed; the most important being the need for a 25 to 30 second stabilization time between any two segments of the approach profile. Similarly, the scaling functions for the glide-slope and localizer displays, and the flight-director gain schedules were chosen during preliminary flights by NASA Test Pilots.

Flight testing is an expensive and time-consuming effort. Consequently, an exhaustive evaluation of approach profile geometries was not a viable option. Thus, the approach profile definition during the NASA/FAA flight tests had to be based on limited data. Further improvements in the definition of the selected flight-profile geometries and parameters may be achievable through a more exhaustive flight test evaluation. Hence, the merits of an alternative approach to TERPS operational enhancement, based upon the use of real-time piloted simulations (including, where appropriate, pilot model-based off-line computer simulations), prior to flight test verification, need to be explored.

This report describes the findings on: "Technical Requirements for Benchmark Simulator-Based TERPS Evaluation," whose overall goal was to investigate the near-term (2 to 5 years) and long-term (10 to 15 years) feasibility and practicality of utilizing simulation technology for TERPS operational enhancement. The specific objectives were: (a) to identify and define which parts of TERPS may be evaluated with the present state of the art in simulator technology, and (b) to recommend a test plan for benchmark simulator-based TERPS evaluation of standard ILS and MLS approaches (i.e., 3° glide-slope ILS or 6° , 9° , 12° glide-slope MLS straight-in and constant-speed approach profiles) using NASA-ARC simulators.

SIMULATION-BASED APPROACH TO TERPS EVALUATION AND ENHANCEMENT

In order to determine the merits of using a simulation-based approach to TERPS evaluation and enhancement, it is necessary to understand the problems associated with simulating the various modules comprising the closed-loop simulation. A block diagram of the closed-loop simulation (either pilot-in-the-loop or pilot model-based) is shown in Figure 1. The overall simulation is relatively complex and consists of several interconnected modules for simulating the navigation, guidance, displays/controls and visual/motion systems.

The purpose of the on-board navigation system is to process the noisy position data provided by the external navigation aids (e.g., MLS azimuth/elevation, range; GPS range measurements, etc.) and on-board sensors (e.g., radar range estimates, FLIR bearing/elevation), and blend it with on-board dead reckoning system measurements of vehicle acceleration and/or velocity (e.g., strap-down INS, Doppler radar, air data/gyro compass) to obtain an estimate \hat{x} of the vehicle state x (i.e., range, range-rate, azimuth, and elevation with respect to a helipad referenced coordinate system).

The guidance system must provide the appropriate cockpit information necessary for the pilot to follow the reference flight path and ground speed profiles. This information can be in the form of vertical (i.e., glide-slope) and lateral (i.e., localizer) path following errors or in the form of pitch, roll, yaw and collective flight director commands. Standard cockpit instruments as well as advanced electronic displays may be used to provide the pilot with the necessary situation information and guidance commands.

The ability of the helicopter pilot to follow precisely a desired terminal approach profile (e.g., 3° , 6° , 9° , 12° straight-in or curved reference flight path plus a prescribed decelerating velocity profile) depends intimately on the quality of the navigation/guidance information provided by the cockpit instrumentation and on the vehicle (i.e., helicopter with SCAS) flying qualities. However, because of the closed-loop nature of the system, it is not possible to decouple or isolate the impact of one individual module (i.e., guidance, navigation, displays or SCAS) on total system performance without considering the influence of the other remaining elements. This interdependency is evident in the observed reciprocal relationships between display and control sophistication and between the quality of the external navigation aids and the complexity of the on-board navigation system. Therefore, it is important, that each of the modules in the closed-loop simulation of Figure 1 match as closely as possible the situation experienced in actual flight.

Simulation modules for the on-board navigation, guidance and display system are defined by specific algorithms and, hence, can be made almost identical to the formulations used in the actual aircraft. However, accurate

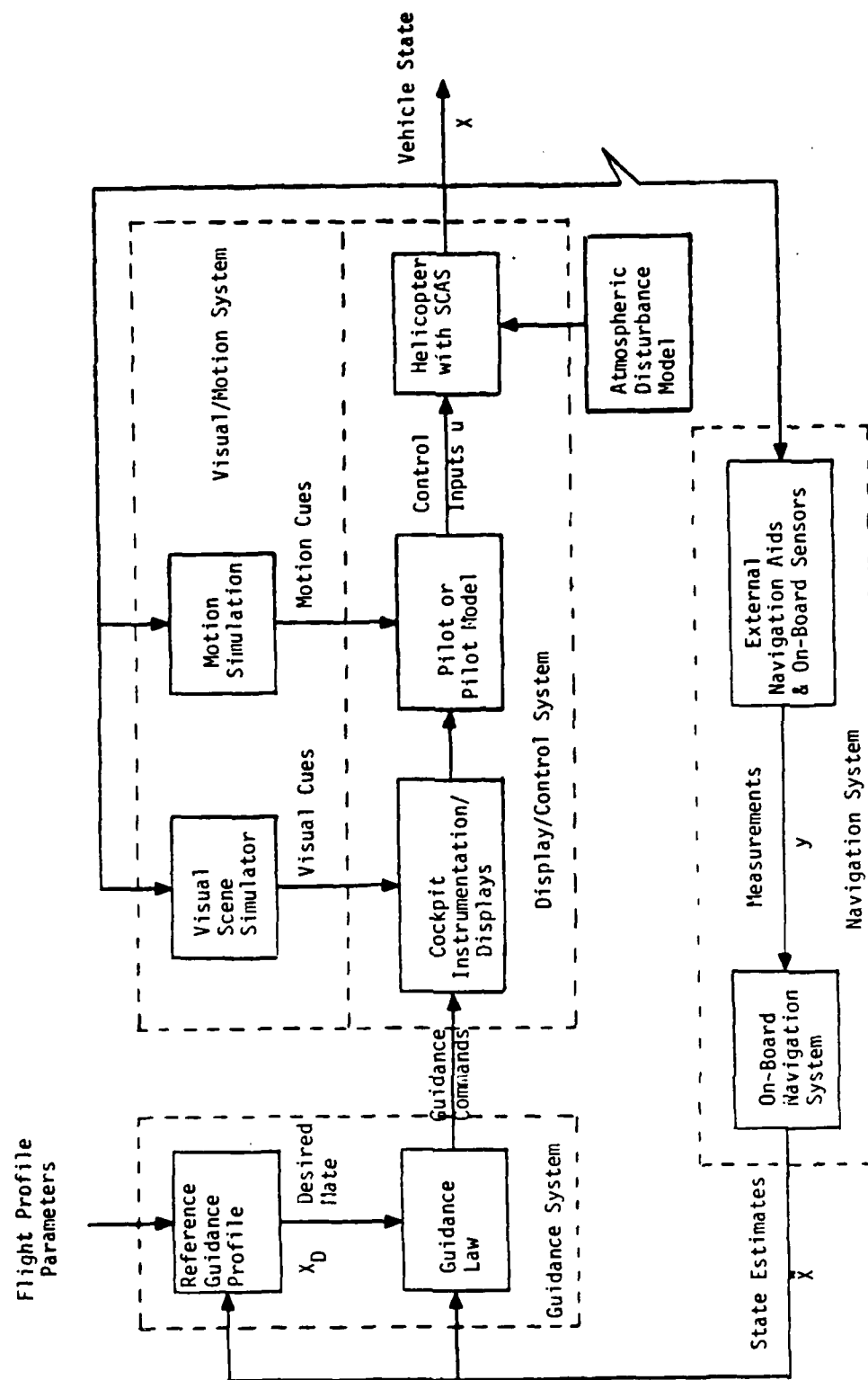


Figure 1. Elements of Closed-Loop Simulation for Evaluation/Enhancement of Terminal Instrument Procedures (TERPS)

simulation of the external navigation aids, on-board sensors, helicopter dynamics, atmospheric disturbances, vehicle motion and the visual scene is a non-trivial task. The problem lies in the development and validation of models for these individual elements, and their interaction with each other.

Extant models for the key modules corresponding to (a) external navigation aids, (b) atmospheric disturbances, (c) visual simulation (d) motion simulation, (e) helicopter dynamics and (f) the human pilot, were reviewed and are summarized in Appendices A through F, respectively.

It should be emphasized that the fidelity requirements on the various modules used in a real-time piloted simulation depend upon the specific terminal approach scenario to be investigated. Typically, the degree of fidelity required for each of the modules is highest for simulating precision, curved, descending and decelerating approaches to a helipad. However, as one regresses from this extremely stringent approach scenario towards precision, constant-speed, curved descending approaches, and, eventually, precision, straight-in landings, the required degree of realism in some modules can be relaxed. For example, navigation can be assumed to be perfect (i.e., assume zero navigation errors) while investigating the optimum curved approach profile parameters and other key factors as long as the final approach segment corresponds to a conventional landing approach. However, for decelerating approach profiles, navigation errors and guidance errors can be strongly coupled; under these circumstances the navigation system errors (i.e., both the external navigation signal errors, the on-board sensor errors and the on-board navigation filter model) cannot be ignored and must be simulated with high fidelity.

Any simulation, by definition, carries with it a risk or liability of producing erroneous results and conclusions. The problem lies in using inaccurate, incorrect or inappropriate mathematical models to represent real-world objects (e.g., helicopter dynamics and the human pilot) or phenomena (i.e., navigation signal propagation errors, visual scene generation, and motion simulation). Furthermore, even if perfect models were available, errors in the choice of the simulation facility and data-interpretation can escape being detected, and can lead to overly optimistic or even false simulation predictions.

However, it appears that simulation technology, as it exists today, may be adequate for evaluating enhanced TERPS for a number of non-standard situations. A discussion of which parts of TERPS may be evaluated with the present state-of-the-art in simulator technology is presented in the following section, along with a test-plan for TERPS evaluation of standard ILS and MLS approaches using NASA/ARC simulators.

TEST PLAN FOR SIMULATOR-BASED TERPS EVALUATION

REQUIREMENTS

Enhanced helicopter TERPS criteria need to be developed for the following non-standard situations.

1. Non-standard terminal approach profiles.
2. Non-standard external navigation aids and on-board filters.
3. Non-standard landing guidance algorithms.
4. Non-standard control/display augmentation systems.
5. Non-standard landing sites.

Existing simulators at NASA/ARC may be used for evaluating the TERPS for one or more of the above non-standard approach scenarios. NASA/ARC simulator facilities of interest for this effort are:

1. Vertical Motion Simulator (VMS)
2. Chair 6 Helicopter Simulator
3. S-19 UH-1H Simulator
4. Rotorcraft Digital Advanced Avionic System (RODAAS)

A new facility called the Advanced Rotary Wing Simulator (ARWS) is being considered for implementation within three years. It will be the rotary-wing equivalent of the existing fixed wing Manned Vehicle Systems Research Facility (MYSRF) at NASA/ARC. An upgrade or modification to the Ames VMS facility called the Rotorcraft Systems Integration Simulator (RSIS) is also underway and planned to be completed in another two or three years.

A review of these facilities shows a wide range of features, capabilities and sophistication. All four existing simulators at NASA/ARC are capable of supporting portions of the TERPS evaluation, and in particular a benchmark TERPS evaluation of standard ILS or MLS straight-in approaches. All four simulators have identical mathematical models for the MLS signals (Azimuth, elevation and range) and the atmospheric disturbances. The RODAAS and S-19 Simulators both have a UH-1H six-degrees-of-freedom mathematical model simulated in their respective host computers (i.e., PDP 11/23 for RODAAS and -9 for S-19).

The Chair 6 Simulator currently has access to three specific helicopter mathematical models--the SH-3, CH-47 and CH-53, on the -9 host computer. However, it also capable of simulating the 6-DOF UH-1H model⁶ used on the S-19 and RODAAS Simulators. In addition, the Chair 6 Simulator can also support the real-time simulation of a generic (as opposed to specific helicopter models) 9-DOF mathematical model for a helicopter that explicitly includes 3-DOF for the rotor tip path plane dynamics (i.e., 1 coning angle $a_0(t)$ and two flapping angles $a_1(t)$ and $b_1(t)$) as well as the 6-DOF for the rigid body dynamics.

The VMS can accommodate any of the above-mentioned helicopter models. Furthermore, the VMS, using the CDC 7600 as the host computer, can also simulate more complex "blade element" mathematical models for helicopters; although perhaps with some restrictions on the number of blades and the number of segments per blade that can be simulated in real-time (i.e., cycle time T small enough to simulate high frequency rotor frequencies without producing aliasing effects).

No visual scene generation capability is currently available on the RODAAS. The S-19 and Chair 6 Simulators have a single window visual scene display driven by the VFA 2 or 7 terrain boards; CGI displays are not available on these two simulators at the present time. The VMS has a full 5-window CGI display capable of simulating overland, overwater, or nap-of-the-earth (NOE) scenarios. A 6-DOF synergistic motion-drive system is available on the VMS; the other three simulators are all fixed-base.

Among the four simulation facilities, the VMS is the most versatile simulator and is recommended as the first choice for investigating TERPS operational enhancement. However, the VMS is much in demand and can only be acquired for two or four weeks duration by reserving six months or more in advance. If the VMS is not available, the recommended second choice is to use the fixed-base Chair 6 Simulator. The S-19 and RODAAS Simulators are both tailored for specific applications (S-19 as a test bed for UH-1H helicopter flight-test support and RODAAS for UH-1H non-terminal area avionics research) and are not designed as research facilities for terminal area investigations. Therefore, these two facilities are not recommended for TERPS evaluation and enhancement.

The S-19 UH-1H Simulator would have been ideally suited for benchmark simulator-based TERPS evaluation. Unfortunately, the S-19 facility is rather old and uses fixed point arithmetic in its on-board computers (Sperry 1819B 18-bit computers), thereby making it difficult to use for research investigations. Furthermore, this facility may be dismantled in the near future.

Both the VMS and the Chair 6 Simulators may be used with the current state-of-the-art in simulator technology to evaluate parts of the helicopter TERPS criteria. Among the five non-standard situations for which enhanced TERPS need to be developed, the investigation of the feasibility of flying non-standard terminal approach profiles is the most important and would serve as the pacing item for evaluating the other four situations. Starting with the standard 3° glide-slope (ILS or MLS) straight-in, constant airspeed, precision approach profile to a 50 ft AGL or higher decision height (50 ft decision height corresponds to a decision range of $\approx 1,000$ ft for VFR deceleration to a hover over the landing pad), the various non-standard precision approach profiles are listed below in order of increasing difficulty or complexity of simulation:

1. 6° , 9° , and 12° glide-slope straight in, constant airspeed, precision approach profiles to decision heights of 100, 150 and 200

ft AGL, respectively. (Decision heights correspond to a constant decision range of 1,000 ft for completing the deceleration to a hover under VFR conditions.)

2. 6⁰ and 9⁰ curved, constant airspeed, precision approach profiles to decision heights of 100 and 150 ft AGL profiles: i.e., U-turn or S-turn approaches, or complex curved horizontal and vertical flight trajectories composed by concatenating straight and/or circular flight path segments.
3. 6⁰, 9⁰, and 12⁰ straight-in, decelerating approaches to a decision height (prescribed values less than 100, 150 and 200 ft AGL, respectively) or to a hover (i.e., zero/zero conditions).
4. 6⁰ and 9⁰ curved, decelerating approaches to a decision height or to a hover.

Three types of tracking errors may be used to evaluate the terminal instrument approaches. They are:

1. Total System Error (TSE = actual position or speed - reference position or speed)
2. Navigation System Error (NSE = actual position or speed - estimated position or speed)
3. Flight Technical Error (FTE = estimated position or speed - reference position or speed)

Note that

$$TSE = NSE + FTE$$

where the reference position (or speed) refers to the commanded or desired position (or speed) and the estimated position (or speed) is the onboard navigation filter's best estimate of the vehicle position (or speed). Actual position (or speed) is known exactly in a computer simulation; in flight tests it must be computed (using appropriate filtering and smoothing algorithms) using measured tracking data from ground-based radar and/or laser tracking systems.

Note that the FTE is the tracking error displayed to the pilot on the cockpit instruments (e.g., glide-slope and localizer errors on the ADI/HSI) and reflects what the pilot sees as the error between his estimated position (or speed) and the desired flight-position (or speed) profile. In other words, the FTE is error tolerated or achievable by the pilot in attempting to follow or track a commanded reference profile (position or speed). The FTE can be assumed to be independent of the NSE as long as the navigation system (i.e., combination of external navaids and on-board navigation filter)

provides sufficiently accurate estimate of the vehicle position (or speed). This can usually be achieved by using an on-board aided inertial navigation system (system that blends vehicle acceleration measurements with external navaid signals) for vehicle position and speed estimation. Non-aided filters such as the alpha-beta (-) filter are not recommended because they are inaccurate (i.e., the estimates are either too noisy or lag in time behind the true values). Furthermore, it has been shown that filters can lead to closed-loop pilot-induced oscillations including loss of vehicle control. Therefore, use of at least a complementary filter (and preferably a Kalman filter) is recommended in order to avoid closed-loop coupling between the landing guidance commands and the navigation system errors.

Thus, as long as the navigation and guidance system can be assumed to be decoupled, the evaluation of constant speed, straight-in and curved steep-descending (e.g., 6°, 9° or 12° glide-slope) precision approach profiles to a decision height (i.e., profiles (1) and (2) described above) may be directly evaluated using existing state-of-the-art in simulator/computer technology. TERPS evaluation of these approaches may be conducted on the Ames VMS or Chair 6 Simulators, using either a specific helicopter model (e.g., UH-1H) or a generic 6 DOF or 9 DOF (6 rigid body DOF + 3 tip-path plane DOF) mathematical model for the helicopter. Flightpath guidance can be provided in the form of raw data or flight director commands. Some interpretation of the results from the simulator-based evaluations may be required in the presence of difficult wind-shear conditions. This is because the helicopter dynamic models are based on the assumption of instantaneous gust penetration. This may not hold in extreme shear situations. Similarly, the data for visual flight segments (i.e., either flare to a landing or go-around) following breakout at decision height could require substantial interpretation before it can be converted to the real-world scenario. This is because the quality of the simulated visual scene (i.e., the visual cues) provided by the terrain board or CGI system during low-altitude flight is questionable and may degrade pilot performance during the visual flight segment.

Simulator-based evaluation of decelerating straight-in or curved steep descending approaches using existing simulators, is not recommended because of substantial deficiencies in fidelity of the individual simulation modules (i.e., helicopter dynamics, gust penetration assumptions, visual/motion simulation, etc.) for vehicle speeds below that corresponding to the loss of translational lift (30-40 kt).

Independent verification and validation of the individual elements or modules comprising the closed-loop piloted simulation must be carried out before attempting a simulator-based TERPS evaluation of decelerating approach profiles.

The ultimate goal of this effort is to develop an optimum long-term (i.e., implementable within 10 to 15 years) facility development and validation plan for TERPS evaluation and operational enhancement over the next 20 years. This involves the development and validation of mathematical models

for representing, as accurately as needed, the various elements in the closed-loop piloted simulation; that is, the type of helicopter dynamics model (e.g., blade element or tip-path plane dynamics rotor model), the type of navigation signal model, the visual/motion system dynamics, the type of atmospheric disturbance model (e.g., analytical versus table look-up) and the dynamic interfaces between the various modules (e.g., interface between the gust model and the helicopter dynamics model, coordination of the visual and motion cueing systems, etc.).

However, the process of simulator development and validation is iterative; flight test data is needed to develop simulation models and simulation predictions must be validated against flight results. Therefore, a logical first step is to determine if results obtained from earlier NASA/FAA flight tests dealing with straight-in^{1,2} and curved steep-descending³⁻⁵ MLS approach procedures can be duplicated in a simulator. Results of such a comparison could be used to improve the fidelity of the individual simulation modules as well as the veracity of the overall closed-loop piloted simulation.

Recommendations for Standard Simulator-Based TERPS Evaluation

- o NASA/ARC Simulator: VMS or Chair-6
- o Vehicle Dynamics: 6-DOF quasi-static UH-1H model
- o Disturbance Model:
 - a) Dryden turbulence u_g , v_g , w_g and analytical wind shear model or,
 - b) recorded wind velocity field data (corresponding to the reference approach profiles) obtained from actual NASA/FAA flight test data.
- o MLS Navigation Signal Model:
 - a) bias plus colored random noise error model or,
 - b) error data (corresponding to the reference approach profiles) extracted from NASA/FAA flight test data.
- o Reference Approach Profiles: 3⁰, 6⁰, 9⁰ and 12⁰ straight-in, constant speed approach profiles as defined in the NASA/FAA flight-test programs.
- o Guidance Commands:
 - a) raw data or "angle only" information; or
 - b) pitch, roll, and collective flight director commands as designed in the NASA/FAA flight-test program.
- o Displays/Controls:
 - a) Standard UH-1H cockpit instruments; glide-slope, localizer and flight-director signals on ADI/HSI.

b) Basic UH-1H helicopter with stablizer bar but without any electronic SCAS.

- o On-Board Navigation Filter: Complementary filters for range, azimuth, and elevation.

The validity of the simulator-based approach can be determined by comparing the simulator-based results (i.e., TSE, NSE and FTE time histories and statistics) with those obtained during actual flight-tests. Any significant discrepancies between the two sets of data can be used to identify and develop more accurate models for the simulation modules and make improvements in the fidelity of the overall simulation.

CONCLUDING REMARKS

The technical requirements for simulation-based TERPS evaluation and operational enhancement have been reviewed. The requirements relate to the fidelity of modules used on the piloted and offline computer simulations. Results of this study indicate that models for the helicopter dynamics, navigation signal and the atmospheric disturbances are the most important elements in the overall simulation. Visual scene simulation is not needed for the IFR flight segments but is crucial for the visual task following breakout at decision height. Motion simulation is also not essential for the constant speed segments of the terminal approach profile. However, it can significantly affect the pilot's performance, workload and opinion rating during curved, steep-descending and decelerating approaches.

Another key factor in improving the veracity of the overall simulation is the manner in which the various component modules are integrated with each other. This is especially important in the interface of the gust disturbances module with the helicopter dynamics. The standard frozen field assumption of instantaneous immersion of the vehicle into the gust field is not valid at low airspeeds. Gradual gust penetration is more appropriate where each rotor blade encounters the gust field at a slightly different point in space and time. However, in order to simulate gradual gust penetration by the rotor blades, a blade element or a tip-path plane model for the rotor dynamics is needed as part of simulated helicopter model.

A review of the literature for the mathematical models of various modules and a critical evaluation of the capability of NASA/ARC simulators suggest that benchmark piloted simulator-based TERPS evaluation of straight-in or curved, steep descending approaches on the Ames simulators appears feasible. Data provided by these benchmark experiments may be used to validate the simulation by comparing it with actual NASA/FAA flight-tests data obtained under similar conditions. Information garnered from such an effort can be invaluable in the iterative simulation validation process.

APPENDIX A NAVIGATION SYSTEMS

The following appendix describes different navigation systems which are pertinent to helicopter flight. These include:

- a. Instrument Landing System (ILS);
- b. Microwave Landing System (MLS);
- c. VOR/DME, TACAN and VORTAC;
- d. Loran-C;
- e. Omega/VLF; and
- f. GPS

The general operating and error characteristics of each system are first described. This is followed by mathematical error model descriptions which are suitable or currently used for helicopter cockpit simulator studies. When available, published flight test measured navigation system errors are also presented.

Instrument Landing System (ILS)

General Description

The instrument landing system (ILS) consists of a glide-slope beam, a localizer beam, and up to three marker beacons.⁷ The glide slope provides vertical steering signals for landing in one direction (the front course) on the runway. The localizer provides lateral steering signals for front-course and back-course approaches to the runway. The first marker beacon (the outer marker OM) is a vertical beam that marks the distance on the glide slope 4 to 7 mi from the runway threshold. The second beacon (the middle marker MM) is placed where the glide slope is 200 ft above the runway (nominally 3500 ft from the threshold). An optional third beacon (the inner marker IM) is placed where the glide slope is 100 ft above the runway (nominally 1000 ft from the threshold). The third beacon is only present for runways certified for Category II and III operations.

Figure 2 depicts the ILS system. It shows the glide slope plane, the marker beacon locations, the locations of the localizer and glide slope antennas, and typical landing lights.

The glide-slope antenna establishes a radiation pattern in space with a signal proportional to the vertical displacement from the glide path. The signal drives the up-down cross-pointer needle in the aircraft. The glide path angle is usually 2.5 to 3 degree. The projected glide path intercepts the runway approximately 1000 ft past the threshold.

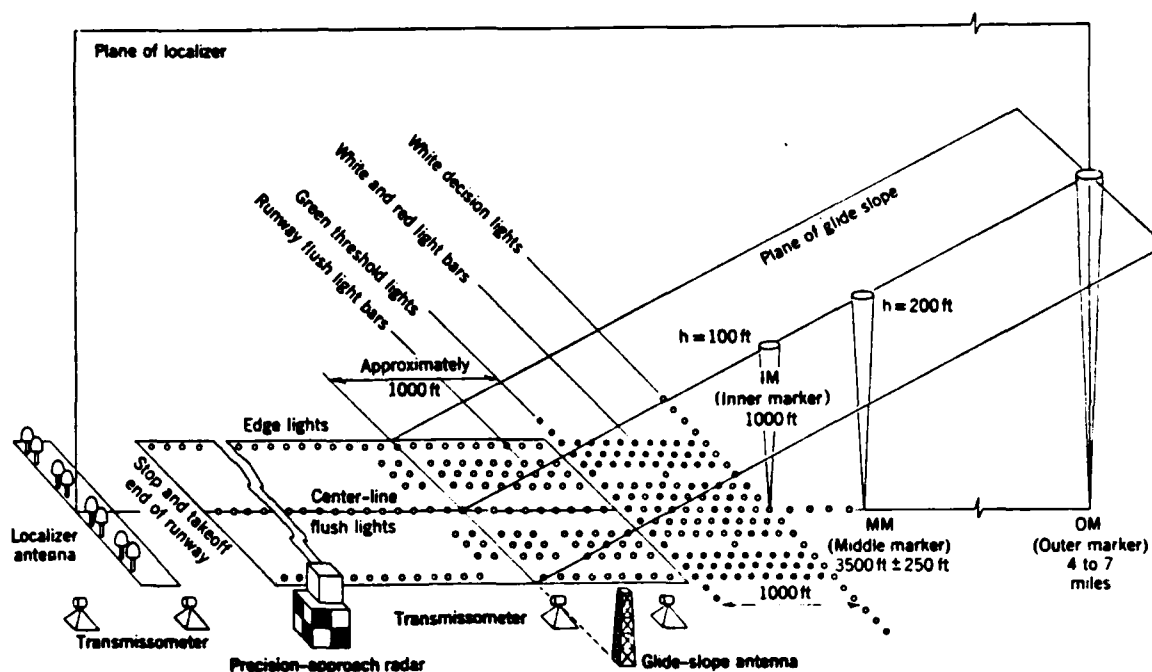


Figure 2. Category II Runway Configurations for U. S. Civil Airports [7]

The localizer establishes a pattern in space whose signal is proportional to the lateral displacement from the vertical plane through the runway center-line. The signal drives the left-right cross-pointer needle in the aircraft.

The usual null-reference glide-slope array consists of two antennas on a mast, one 14 ft above ground and one 28 ft high (for a 3 degree glide slope). The mast is located approximately 1000 ft past the threshold and 500 ft to the side of the runway centerline. Both antennas make use of the ground plane as a reflector to increase the effective antenna aperture. As shown in Figure 3, the contours of constant signal strength are hyperboloids of revolution whose axis of symmetry is perpendicular to the ground. The half-angle of the asymptotic cone is 87 degree for a 3 degree glide slope. A vertical plane through the runway center line intersects the glide-path hyperboloid in a hyperbola whose asymptote is the 3 degree glide path but which flares out near the ground, never touching the runway. The primary contour is 2 to 10 ft above the asymptotic glide slope at the threshold of a 250 ft wide runway, 1 to 5 ft above at the inner marker, and 15 to 30 ft above the runway at its point of closest approach. As a result, the glide slope cannot be used as a touchdown-guidance aid.

Because the glide-slope transmissions are of the continuous-wave type, reflections to the aircraft from surface irregularities, hills, vegetation, and other aircraft will cause bends in the glide path. The received signal is the vector sum of all energy arriving at the aircraft's antenna, including that from reflections as shown in Figure 4. The change from wet to dry terrain within 2000 ft of the antenna causes a 1 ft vertical error at an

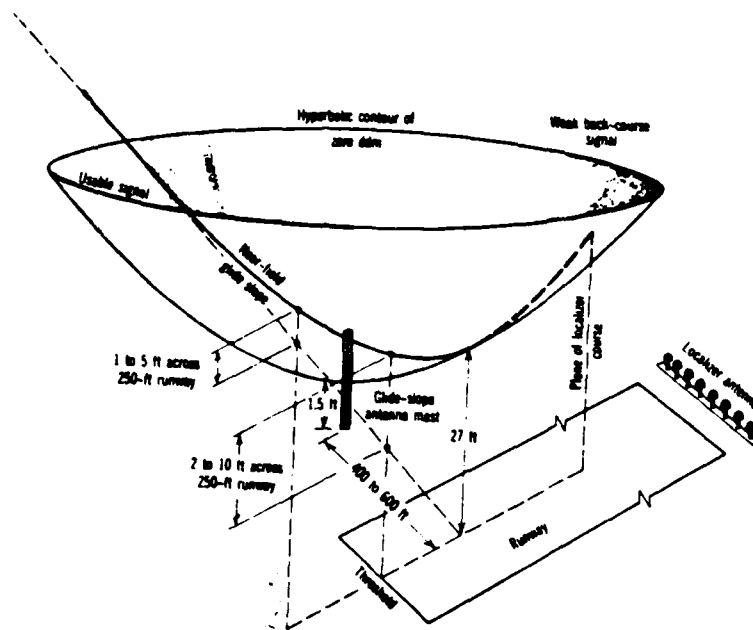


Figure 3. Glide Slope Pattern Near the Runway [7]

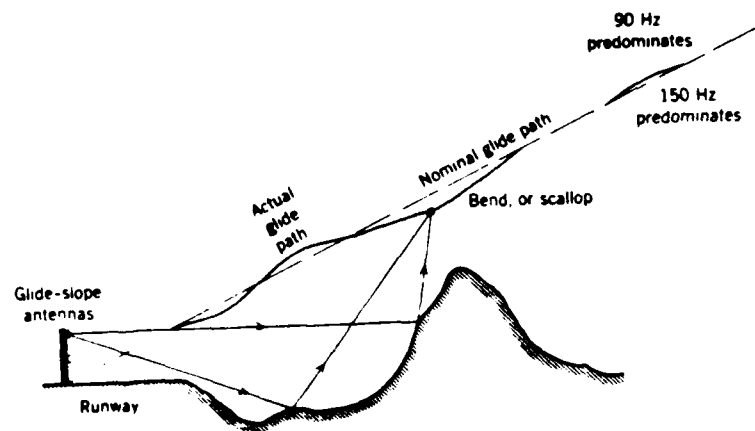


Figure 4. Formation of Bends in the Glide Slope [7]

altitude of 200 ft. A 4 ft snowcover causes a maximum 0.4 degree change in the glide slope angle. Ground irregularities on property that may not belong to the airport authority may cause beam bends.

The localizer signal is of the continuous-wave type, and reflections from terrain, buildings, aircraft and ground vehicles will reflect spurious energy to the landing aircraft, resulting in a bend or scallop in the course. An error of up to 0.3 degree or 60 ft laterally can be caused by an aircraft taking off, and this error can persist for as long as 10 sec.

Localizer data can normally be acquired at a range of 25 nmi within ± 10 degree of the course line.⁸ Within 17 nmi, the coverage extends to ± 35 degree. However, only "fly left" or "fly right" indications are available outside a linear region approximately ± 2.1 degree from the centerline. Localizer data, in practice, may be receivable at elevation angles up to 25 degree above the horizon, depending on the type antenna employed. The lower elevation limit depends both on antenna and terrain, but it provides adequate terrain clearance and is at least low enough for conventional ILS approaches. Thus, the coverage is certainly lower than required for helicopters.

Glide slope data is normally receivable at a maximum range of 10 nmi. for an approach within ± 8 degree of the runway centerline and at elevation angles between 1.35 and 5.25 degree. Only "fly down" or "fly up" information is available outside a linear error signal region approximately ± 0.9 degree above and below the fixed glide path.

The basic data from conventional and advanced ILS provide both course line and descent angle guidance from the on-board receiver, which derives error signals proportional to angular displacement from the runway centerline and from a nominal glide path. The "on course" and "fly to" indications are displayed, and the error signals are available for coupling to an autopilot.

The locations of airports in the United States with ILS equipment are shown in Figure 5.⁹

ILS Error Models

Requirements for ILS installations are specified by the International Civil Aviation Organization (ICAO) for Categories I, II, and III. Two types of errors are addressed: alignment accuracy of the mean beams, and anomalies such as bends superimposed on the mean beams. Tolerances for these errors vary for each of the landing categories.

For the Space Shuttle, a Cat. III system⁸ is used, and error models were developed for this class of ILS. The errors for simulation of shuttle landings are assumed to be biases for the mean beam and random noise for bend representation. The ILS error model for this system is presented in Table 1. This includes both the signal generated plus that of the receiver.

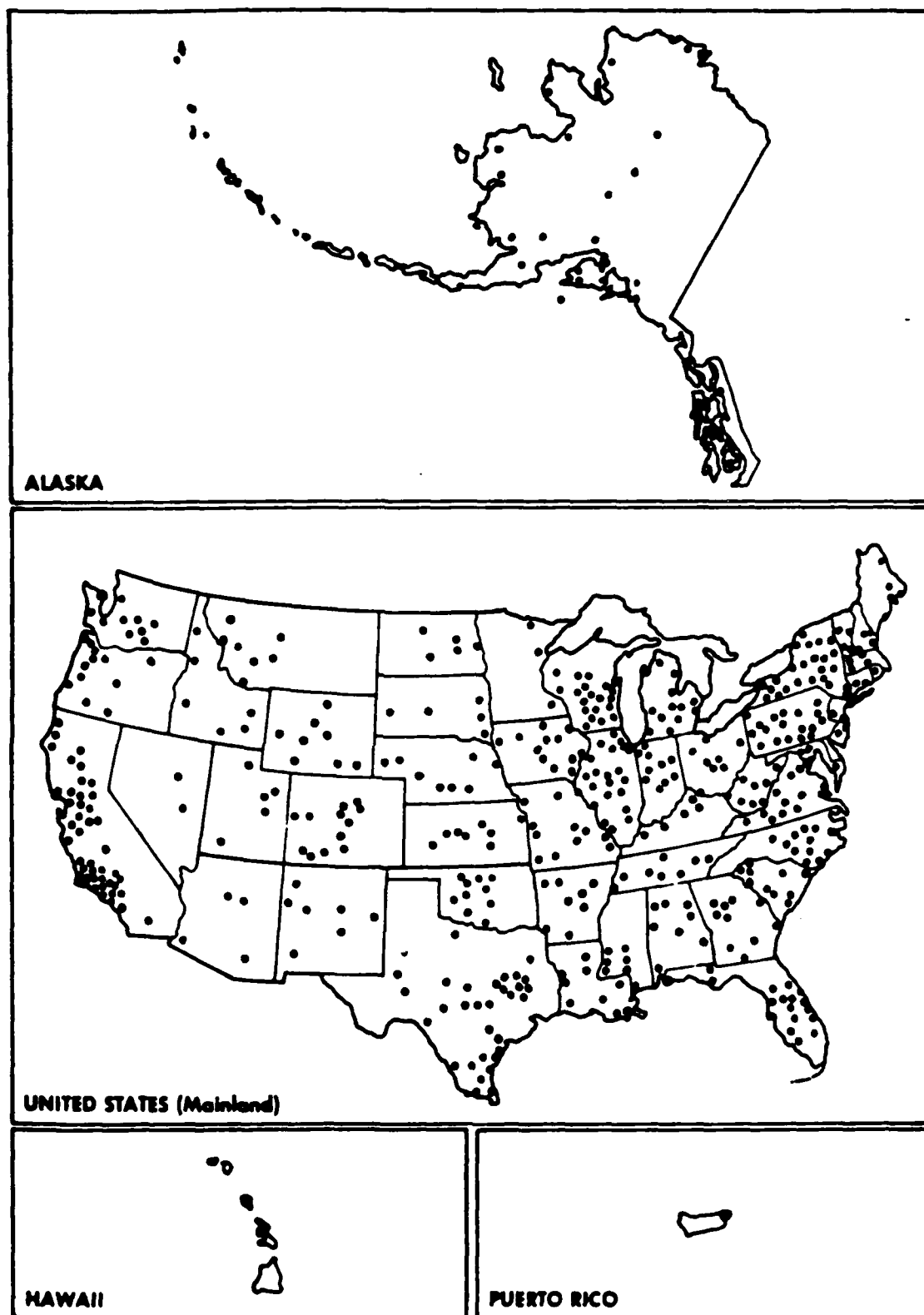


Figure 5. Locations of ILS Equipment Throughout the U. S. [9]

Table 1. ILS Error Models [8]

	Coverage		Meas. Errors (1σ), 3° Glide Slope	
Glide slope ¹	Range:	10-nm	Bias	Random
	Azimuth:	+8°		+15 percent
	Elevation:	0.45θ to 1.75θ		Range
	Altitude:	h > 50 ft	0.7 mrad {t}	0.8 mrad
	Linear regions: within		0.3 mrad {r}	0.8 + 0.4 Δ
	+0.9° (θ = 3°)		0.8 mrad {rss}	1.2 mrad
				Δ = (R _{nm} - 0.6)/3.4
	Coverage		Meas. Errors (1σ)	
Localizer ²	Range:	25 nm; AZ < 10°	Bias	Random
	Range:	17 nm; AZ < 35°		+10 percent
	Elevation:	0.05° to 20°		Range
	Linear region:	+2.1°	0.3 mrad {t}	0.5 mrad
			0.1 mrad {r}	0.5 + 2.6 Δ
			0.3 mrad {rss}	3.1 mrad
				Δ = (R _{nm} - 0.6)/3.4

1. Derived values from assumed 3° glideslope. For 19° glideslope, multiply bias and random by ratio (19°/3°).
2. Derived values from assumed 10 000-ft runway plus 1000 ft to LOC antenna.

NOTES: Bias: Misalignment of mean beam in vicinity of threshold.

Random: Variation of the actual from mean in specific regions.

$(t) = \text{error in transmission, } (r) = \text{error in reception, } (rss) = \text{root sum square.}$

In Reference 1, data were recorded from 10 different ILS beams to develop models of repeatable ILS errors as function of position from the runway. These models are intended for realistic ILS signal simulation. The noise structure of ILS courses in space, whether localizer or glide slope, are repeatable when measured precisely. The structure contains noise which is a result of the multipath effects of objects surrounding the airport such as buildings, terrain, power lines and towers. An aircraft moving along a given path in space will receive the same noise structure information. These data representing the repeatable errors were recorded into tables with 1000 elements, with each element representing a 25 ft interval. Figure 6 illustrates the typical localizer error structure, and Figure 7 shows typical glide slope errors. The error tables can be used to generate position dependent ILS errors for digital simulation instead of using the typical bias and random noise models that are typically used.

Table 2 summarizes the current error model parameters used for ILS simulation on NASA Ames helicopter simulators. These consist of colored noise terms that are range dependent. The original source of these models are from the VSTOLAND simulator. The Reference 10 data are more accurate but more elaborate to implement. The current model is probably adequate, but the error parameters should be varied in magnitude to reflect whether the ILS system is for Category I, II, or III facility.

Microwave Landing System (MLS)

General Description

The MLS is a navigation aid providing precision landing guidance and an expanded coverage not provided by the ILS. The basic MLS ground system consists of an azimuth antenna and an elevation antenna. The azimuth antenna is normally located on the runway centerline beyond the stop end, and the elevation antenna is located on either side of the runway in the vicinity of the glidepath intercept point. The azimuth beam sweeps to and from, up to +60 degree in some configurations about the runway centerline. The elevation beam sweeps up and down similarly to provide coverage between 0 degree and 20 degree. Some configurations also contain a DME antenna to give precision range information which is located near the azimuth antenna. A basic configuration is depicted in Figure 8.

The airborne equipment consists of a receiving antenna, an angle receiver for the elevation and azimuth signal detection, a DME receiver for the range signal, and a control head in the cockpit for selecting various MLS sites and desired glide slopes and azimuth radials. Also provided are signals representing deviations from the selected glide slope and azimuth radial. These deviations are converted to analog signals in the angle receiver and scaled to provide signals similar to those obtained from an ILS receiver.

The MLS has a time multiplex format in which the antenna scans are not separated at equal time intervals. This time shift is referred to as "jitter." The signals are also subject to spurious spikes.¹¹

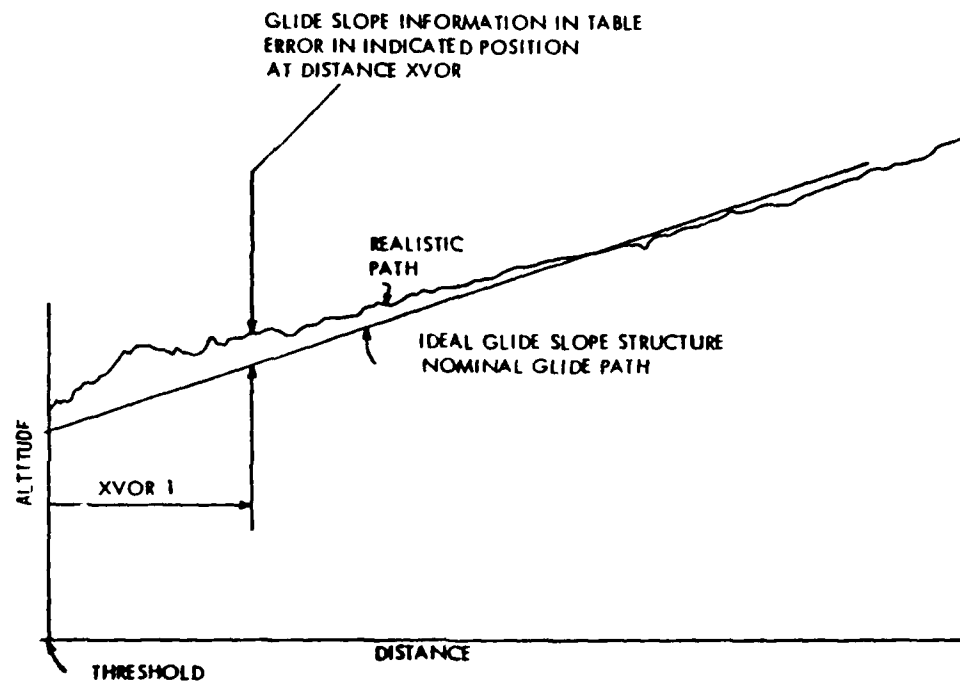


Figure 6. Glide Slope Table Errors [10]

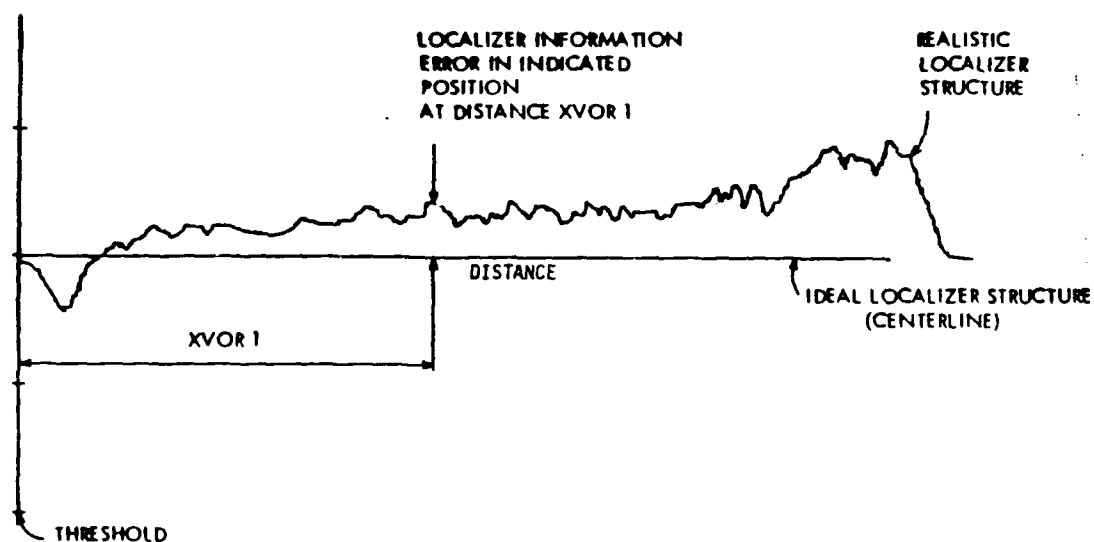


Figure 7. Localizer Table Errors [10]

Table 2. Discrete Ames helicopter Simulation Equations for the ILS

Error Equations:

Localizer:

$$B_{1L}(n+1) = K_1 B_{1L}(n) + \sigma_{bL} \sqrt{1-K_1^2} \eta_1$$

$$B_{2L}(n+1) = K_1 B_{2L}(n) + \sigma_{bL} \sqrt{1-K_1^2} B_{1L}(n+1)$$

$$R_L = \sigma_r \eta_2$$

$$Az_e = Az + B_{2L}(n+1) + R_L$$

Glide Slope:

$$B_{1G}(n+1) = K_1 B_{1G}(n) + \sigma_{bG} \sqrt{1-K_1^2} \eta_3$$

$$B_{2G}(n+1) = K_1 B_{2G}(n) + \sigma_{bG} \sqrt{1-K_1^2} B_{1G}(n+1)$$

$$R_G = \sigma_{rG} \eta_4$$

$$El_e = El + B_{2G}(n+1) + R_G$$

Noise Characteristics:

η_1, η_4 = white, zero-mean Gaussian noise with $\sigma = 1$.

Range dependence:

	$r_{loc} < 3500$	$3500 < r_{loc} < 24000$	$24000 < r_{loc} < 60000$	$r_{loc} > 60000$
σ_{bL}	0.3°	0.3°	0.3°	No error
σ_{rL}	0.5°	$0.5^\circ + \Delta_r 2.6^\circ$	3.1°	
σ_{bG}	0.8°	0.8°	0.8°	
σ_{rG}	0.8°	$0.8^\circ + \Delta_r 0.4^\circ$	1.2°	

where $\Delta_r = (r_{loc} - 35000)/23860$.

Noise shaping gain $K_1 = e^{-2\Delta t/3}$; Δt = time step.

Signal valid region

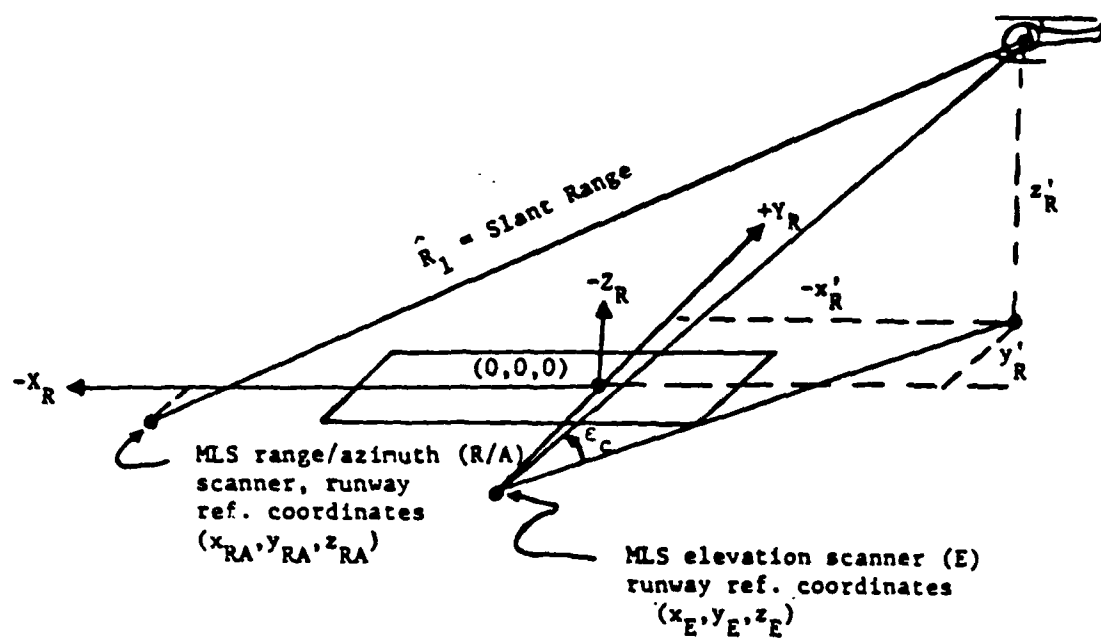
Localizer: $R_L = 150000$ ft

$Az = 35^\circ$

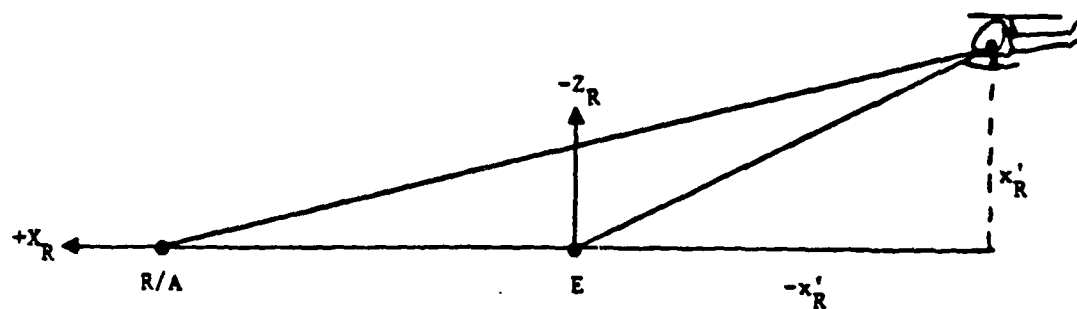
Glide Slope: $R_G = 150000$ ft

$Az = 35^\circ$

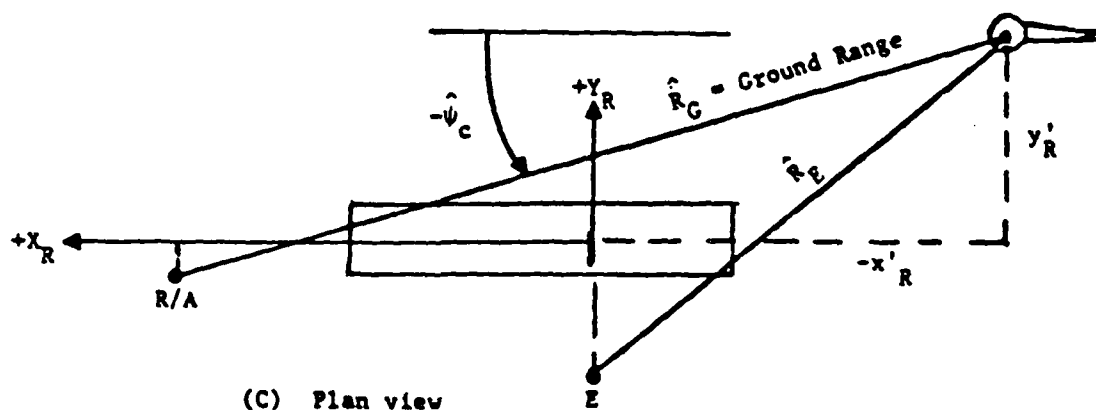
$El_{max} = 20^\circ$



(A) Three-dimensional view



(B) Elevation view



(C) Plan view

Figure 8. Geometry of MLS Navigation

There are three basic transmitters for the MLS signals. The azimuth and elevation transmitters are Time Reference Scanning Beams. The DME transponder is a time-of-arrival system. Frequently these patterns are modeled as straight lines and flat planes. This is not the true nature of the MLS signals in space. Instead they are quadric surfaces. The azimuth pattern is a circular cone with a horizontal axis of rotation. The elevation pattern is a circular cone with a vertical axis of rotation. The DME has a spherical pattern.

There are very few portions of the MLS signal where the non-linear nature has significant differences from flat plane assumptions. Two areas that are impacted are the glide path inside the Decision Height for the single elevation antenna and the ground track of the aircraft at the upper, outer corners of the MLS coverage volume.

Figure 9 shows the conical shape of the azimuth signal. The nappes are formed by the phased-array antenna. The horizontal axis of the cone is perpendicular to the boresight of the antenna. The surface behind the antenna and above the coverage limit is not transmitted by the MLS.

Figure 10 illustrates the conical pattern of the elevation antenna. The axis of the cone is the zenith of the antenna. The cone's surface behind the antenna is not transmitted by the MLS. As an aircraft approaches the runway on a constant elevation angle, it follows the surface of the cone, similar to the ILS. (See Figure 3). Because the antenna is not on the runway, the aircraft will not actually descend to the vertex of the cone.

When the sweeping azimuth beam centers on the boresight of the azimuth antenna, the beam is a flat plane. On either side of the boresight the pattern is the cone surface. The cone shape is more pronounced as the beam moves away from the boresight to the edge of the MLS coverage. Table 3 shows the differences in ground track positions between the conical MLS and a planar system for various values of azimuth, elevation and range. Here, it is assumed that the three transmitters are colocated. At short approach distances, the differences between the flat plane assumption and the actual MLS conical position are negligible. At the edge of the MLS coverage the angle between the ground tracks of the conical and the planar systems is sufficient to present different positions on the ATC surveillance radar scope.¹²

Figure 11 indicates the difference in ground azimuth angles when comparing the conical model with the planar model. The differences are inconsequential except at the high azimuth and elevation angles.

The location of the elevation antenna beside the runway near the touch-down point combined with an aircraft which flies at a constant elevation angle and in the vertical plane of the extended runway centerline creates a glide path hyperbola. The intersection of the plane and the cone result in a hyperbola where the origin is at the phase center of the elevation antenna. The asymptotes are the generatrix of the cone projected on the runway centerline plane.

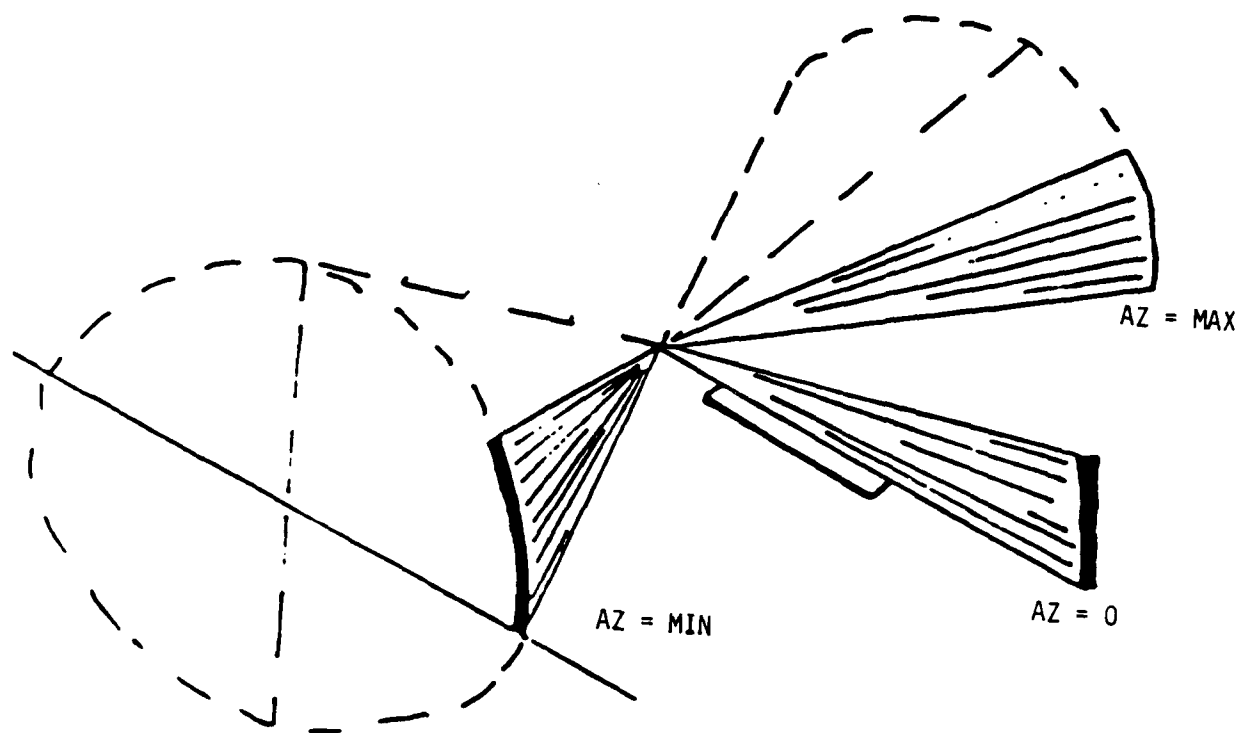


Figure 9. Conical Pattern of MLS Azimuth Signal [12]

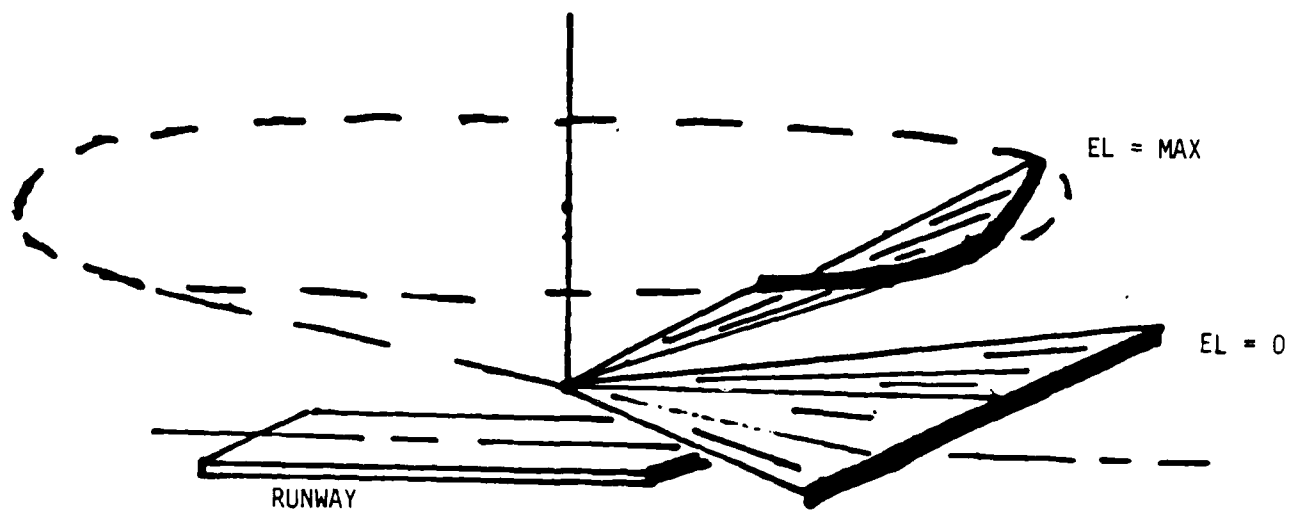


Figure 10. Conical Pattern of MLS Elevation Signal [12]

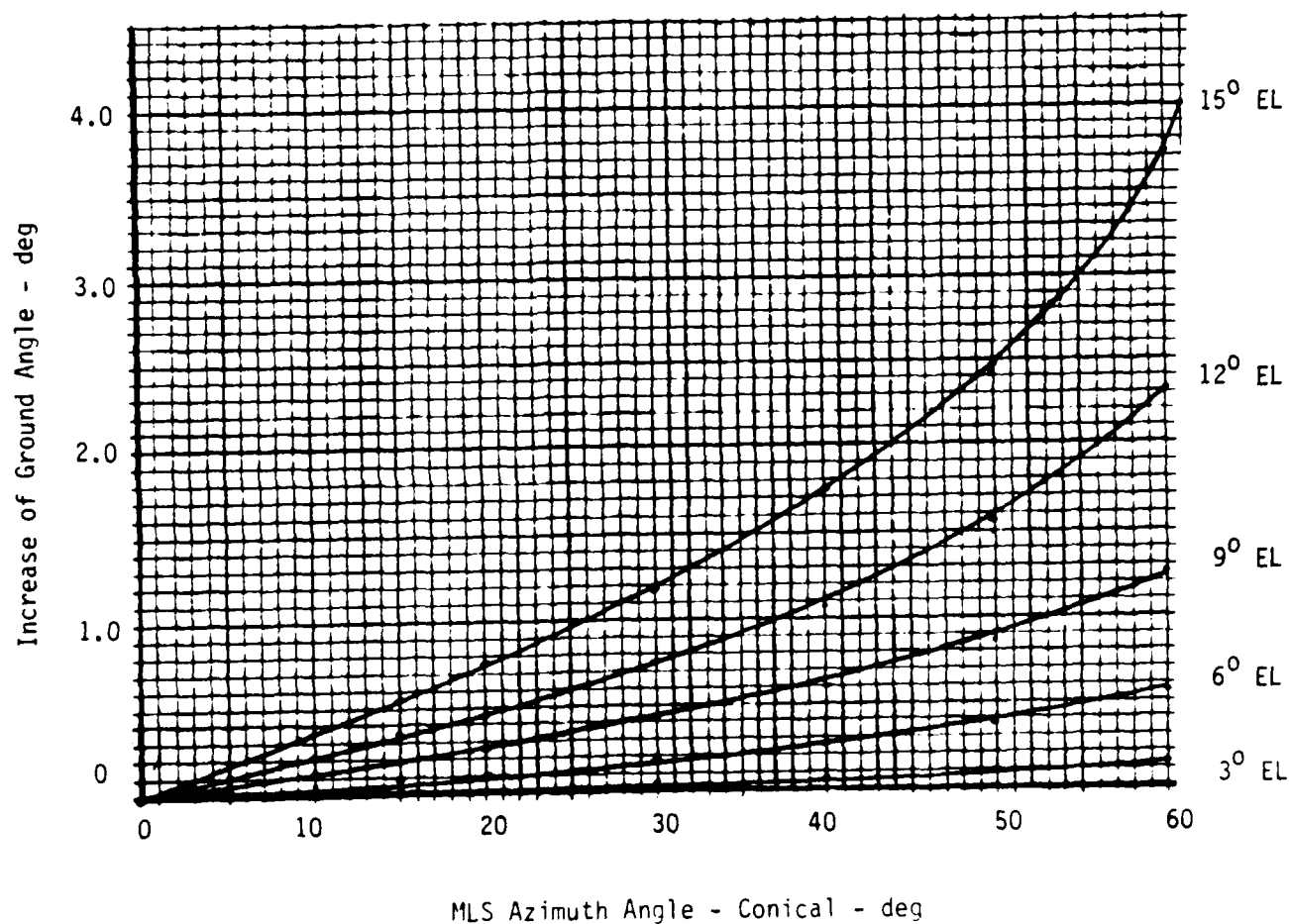


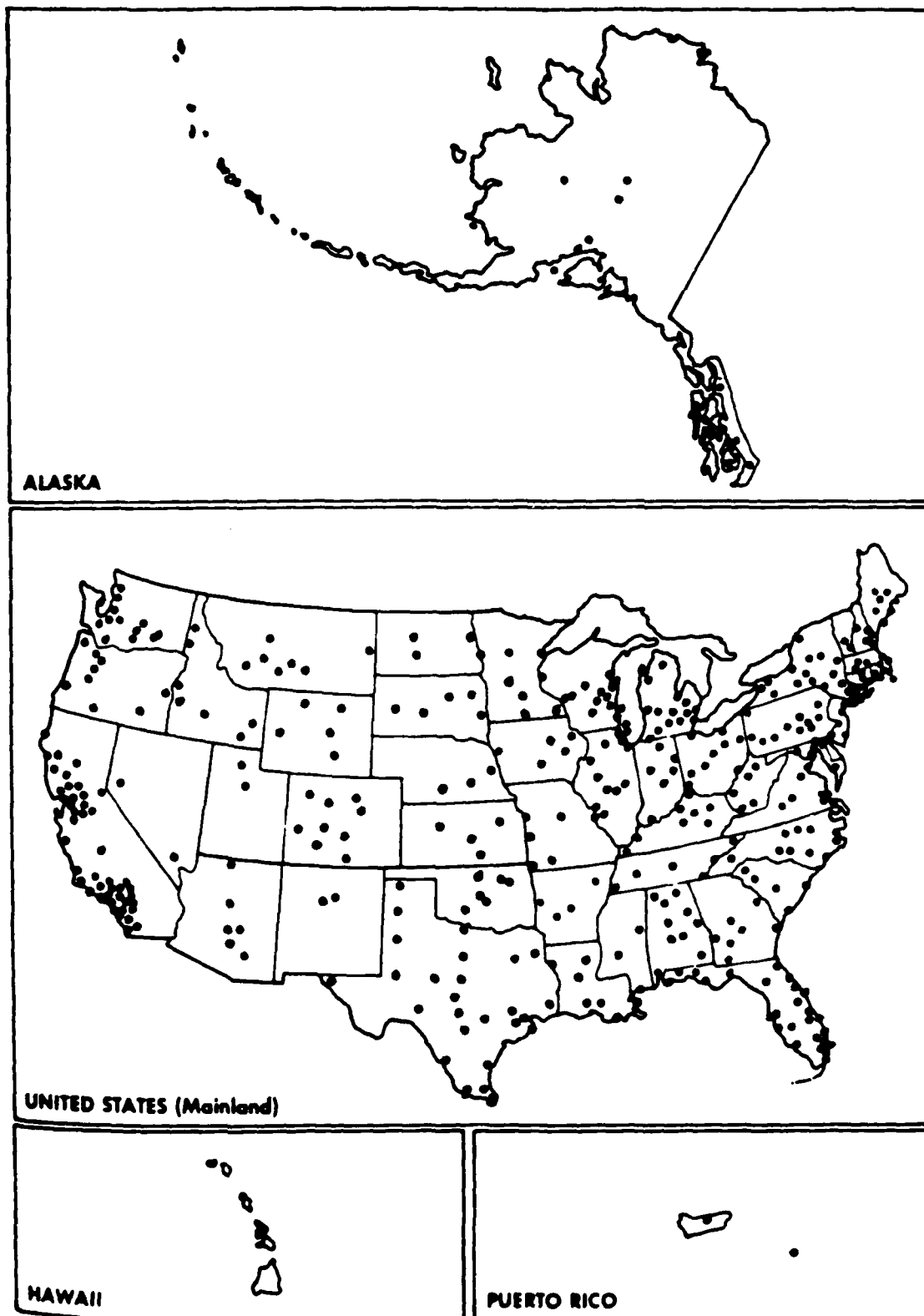
Figure 11. Difference in Ground Azimuth Angle Due to Surface Approximations as Planes Rather Than Conic Surfaces [12]

Table 3. Ground Track Difference Between Conic and Plane Surfaces for Various Aircraft Locations

DME NM	AZ DEG	EL DEG	X Feet	Y Feet	Dist Feet
1	10	3	-.3	.4	1.5
	20	6	-4.7	11.4	12.1
	40	9	-40.8	48.1	63.0
10	10	3	-2.6	14.5	14.7
	20	6	-41.6	113.8	121.2
	40	9	-407.8	480.8	630.5
20	10	3	-5.1	28.9	29.4
	20	6	-83.1	227.7	242.5
	40	9	-815.6	916.7	1,261.0
at 20,000 Feet Ceiling					
16.0	40	12	-1,168.0	1,365.5	1,798.9
12.8	40	15	-1,473.4	1,703.4	2,252.2

The difference between the asymptote and the actual glide path is negligible in the approach phase of the MLS maneuver. The difference becomes noticeable after the Decision Height and becomes significant as the aircraft is over the runway. Table 4 shows the differences between the asymptote and hyperbolic paths for various approach elevation angles with a specific elevation antenna site. One conclusion for this geometric situation is that at the Decision Height the pilot could transition to another elevation reference such as available from a second elevation antenna. On a manual approach, the pilot should hold the established rate of descent until flare.

Figure 12 depicts the anticipated locations of MLS coverage for the 1990 time period.⁹



**1990 SYSTEM
MICROWAVE LANDING SYSTEMS**

Figure 12. Projected MLS Locations for the 1990 Time Period [9]

Table 4. Difference Between Hyperbolic Path and Asymptotic Approximation
For Elevation Antenna With Various Approach Angles

Elevation location: Offset = -250 Feet; Set Back = -258 Feet;
Phase Center Height = 7 Feet; Nmi = 6076.1 Feet.

El Angle	Distance from Threshold	Glide Path Height		Difference
		Asymptote	Hyperbola	
3	Abeam Antenna	7	20.1	13.1
	0	20.5	25.8	5.3
	1,000 Feet	72.9	74.2	1.3
	1 Mile	339.0	339.2	0.3
	2 Mile	657.4	657.5	0.1
	5 Mile	1612.7	1612.7	0.1
6	Abeam Antenna	7	33.3	26.3
	0	34.1	44.8	10.6
	1,000 Feet	139.2	141.8	2.6
	1 Mile	672.7	673.3	0.5
	2 Mile	1311.4	1311.6	0.3
	5 Mile	3227.2	33227.3	0.1
9	Abeam Antenna	7	46.6	39.6
	0	47.9	63.9	16.0
	1,000 Feet	206.2	210.1	3.9
	1 Mile	1010.2	1011.0	0.8
	2 Mile	1972.6	1973.0	0.4
	5 Mile	4859.7	4859.8	0.2

MLS Error Models

In Reference 11, a noise model is posed for the MLS receivers based on test results presented in Reference 13. The general discrete equation for random noise is

$$r_{n+1} = G_i r_n + \sqrt{1-G_i^2} \sigma_i r_i \quad (1)$$

where r_i is a random Gaussian number with variance 1 and zero mean, σ_i is the standard deviation of the noise, and G_i is a constant given by

$$G_i = e^{-\Delta t / \tau_i} \quad (2)$$

Here, τ_i is a time constant, and Δt is the simulation update interval. The inverse time constant $1/\tau_i$ is taken to be 3, 4, and 3, respectively, for the azimuth, elevation, and range measurements. Values for σ_i are .01 to .02

degree for azimuth and elevation and 7.5 to 10 ft for the range measurement. These error terms are used in NASA's Advanced Cab Simulator for MLS errors.

In Reference 14, the MLS range error from flight data taken at NASA's Crow's Landing facility was found to have a Gaussian distribution with a mean error of 0.1 ft and a standard deviation of 5.9 ft. However, this included the effect of on-board filtering of the raw range data.

In Reference 2, various navigation performance data were analyzed for 140 helicopter approaches at Crow's Landing along 3, 6, and 9 degree glide slopes to decision heights of 50, 100, and 150 ft. From these data, it was found that MLS range error had a approximate standard deviation of 10 ft. Elevation error had a 0.025 degree standard deviation with zero mean. Azimuth error had a similar standard deviation and also a bias of 0.1 to 0.2 degree.

In Reference 5, further data results of curved helicopter approaches to the Crow's Landing MLS were used to compute and plot several statistical performance measures. Elevation angle was within ± 0.05 degree (2σ) of zero until about two miles-to-go. After this point, it deteriorated because of the geometric elevation problems discussed earlier. The azimuth error was within ± 0.15 degree (2σ) of zero. Range error was ± 40 ft (2σ) with an offset bias of about -90 ft. These results were for 37 straight-in, 12 degree glide slope approaches.

Table 5 summarizes the current error model and its parameters used for MLS simulation on NASA Ames helicopter simulators. Biases are set to zero and no spikes or data dropouts are simulated. Also, the geometric effects discussed earlier are not included. The error equations for range, azimuth, and elevation all have a form similar to Eq. (1).

VOR/DME

General Description

The VHF omnidirectional range (VOR) has been the standard enroute navigation system for measuring aircraft bearing (designated as "theta") to a specific ground site (e.g., the transmitting VOR ground station) since 1949. The VOR principle of operation is simple; the ground station radiates a cardioid pattern that rotates at 30 Hz, generating a 30 Hz sine wave at the output of the airborne receiver. The ground station also radiates an omnidirectional signal which is modulated with a fixed 30 Hz reference tone. The phase between the two 30 Hz tones varies directly with the bearing of the aircraft.

Table 5. Discrete Ames Helicopter Simulation Equations for the MLS

Error Equations (3 equations of generic form):

$$B_{1i}(n+1) = K_1 B_{1i}(n) + \sigma_i \sqrt{1 - K_1^2} \eta_i$$

i = DME range random error (mdr)

Azimuth random error (mar)

Elevation random error (mer)

$$\text{Range } R_e = R + B_{1\text{mdr}}$$

$$\text{Azimuth } A_{ze} = A_z + B_{1\text{mar}}$$

$$\text{Elevation } E_{1e} = E1 + B_{1\text{mer}}$$

Noise Characteristics:

η_i = white, zero-mean Gaussian noise with $\sigma = 1$.

Standard Deviations:

$$\sigma_{\text{mdr}} = 20 \text{ ft}; \sigma_{\text{mar}} = 0.03^\circ; \sigma_{\text{mer}} = 0.02^\circ$$

Noise shaping gain: $K_1 = e^{-\Delta t/2}$; Δt = time step.

Signal valid region:

Range 180,000 ft;

Azimuth: $-40^\circ < A_z < 40^\circ$ when $0^\circ < E1 < 20^\circ$

Elevation: $1.1^\circ < E1 < 15^\circ$ when $-40^\circ < A_z < 40^\circ$

The measurement accuracy of the VOR is relatively consistent and is limited by only two major factors:

1. Site error due to reflecting objects near the transmitting station; and
2. Error in reading 30 Hz phase differences in the airborne equipment.

To remove site error, it is customary to locate the station on smooth terrain and to remove all trees and other major obstructions to a distance of 1500 ft. Where this has not been possible, errors of up to 15 degree have been experienced. One solution is to install the improved Doppler VOR.

The Doppler VOR applies the principles of wide antenna aperture to the reduction of site error. This involves using a 44 ft diameter circle of 52 Alford loops, together with a single Alford loop in the center. This allows up to a ten-fold reduction in site error. At one example site, maximum deviations measured during a 20 nmi orbital flight were reduced from 2.8 degree with a standard VOR to 0.4 degree with a Doppler VOR.

To remove airborne error requires use of the precision VOR receiver which uses multilobe principles. The combination of Doppler and precision VOR can provide a total bearing measurement error on the order of 0.25 degree.

Distance measuring equipment (DME) is an internationally standardized pulse-ranging system for aircraft, operating in the 960 to 1215 MHz band. It measures slant range (designated "rho") from the aircraft to the ground station. When the ground station is colocated with a VOR station, the resulting combination forms the standard ICAO rho-theta short-range navigation system.

Tacan (Tactical air navigation system) is a military omnibearing and distance measurement system using the same pulses and frequencies for the distance measurement function as the standard DME system. Vortac is the colocation of VOR and Tacan to provide rho-theta navigation to both civil and military aircraft. Thus, each type of aircraft may fit into the same air traffic control environment regardless of which type of airborne equipment it carries.

DME is based on the aircraft interrogator transmitting pulses on one of 126 frequencies, spaced 1 MHz apart, in the 1025 to 1150 MHz band. The ground beacon (or transponder) receives these pulses and, after a 50 μ sec fixed delay, retransmits them back to the aircraft on a frequency 63 MHz below or above the airborne transmitting frequency. The airborne interrogator automatically compares the elapsed time between transmission and reception, subtracts out the fixed delay, and converts the result to distance to the station.⁷

The ICAO requires an overall DME system accuracy of 0.5 nmi or 3 percent, whichever is greater. Actual system accuracy can be much better than this. The ground delay between transmission and reception must be held as constant as possible. Typical enroute beacons exhibit a total variation of ± 0.5 sec, corresponding to a distance error of ± 0.04 nmi. Beacons associated with MLS systems can be designed to be more accurate due to the smaller spread of interrogation signal levels. On board equipment inaccuracy will add some noise, but the error in slant range is primarily a bias specific to each station.⁷

Ground stations are classified according to their intended use. The stations are available for use within their service volume. Outside the service volume, reliable service may not be available. For standard use, the airspace boundaries are called standard service volumes (SSV). They are defined in Table 6 for the three station classes. These boundaries are also depicted in Figures 13, 14, and 15.

Table 6. Standard Service Volumes for VOR/DME coverage.

Designator	Altitude and Range boundaries
Terminal (T)	From 1000 ft AGL up to and including 12000 ft AGL at radial distances out to 25 nmi.
Low (L) Altitude	From 1000 ft AGL up to and including 18000 ft AGL at radial distances out to 40 nmi.
High (H) Altitude	From 1000 ft AGL up to and including 14500 ft AGL at radial distances out to 40 nmi. From 14500 ft up to and including 60000 ft at radial distances out to 100 nmi. From 18000 ft AGL up to and including 45000 ft at radial distances out to 130 nmi.

Within 25 nmi, the bottom of the T service is defined by the curve in Figure 16. Within 40 nmi, the bottoms of the L and H service volumes are defined by the curve in Figure 17. The distance parameter to be compared against the defined boundaries is

$$q = [R_e + h(\text{station}) + h(\text{aircraft})] \sin (R_g / 2 * R_e) \quad (3)$$

Here, R_e is the radius of the earth and R_g is the ground range between the ground station and the aircraft.¹⁵

Within the operational service volume of each station, bearing signal information permitting satisfactory performance of airborne components is normally provided from the radio horizon up to an elevation angle of approximately 60 degree for a VOR component and approximately 40 degree for the Tacan component. At higher elevation angles, the bearing signal information may not

(Refer to Figure 17 for altitudes
below 1000 feet (305 m))

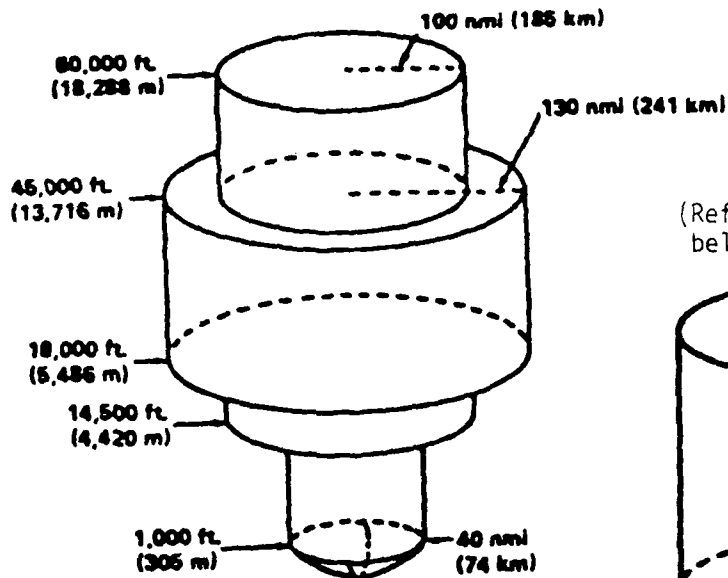
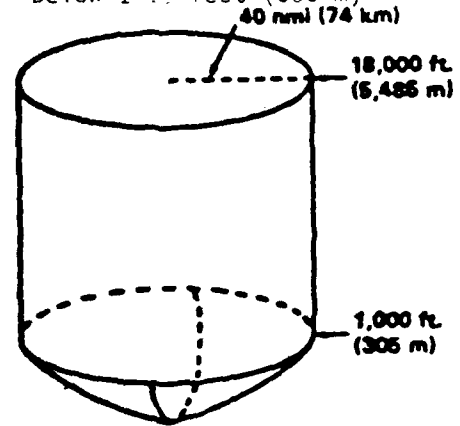


Figure 13. Standard High Altitude
Service Volume [15]

(Refer to Figure 17 for altitudes
below 1000 feet (305 m))



NOTE: All elevations shown are with respect
to the station's site elevation (AGL).
Metric Measurements are given for
convenience and are approximations.
These figures do not reference the area
defined as the Vertical Angle Coverage
Limitations (paragraph 23.d.)

Figure 14. Standard Low
Altitude Service Volume [15]

(Refer to Figure 16 for altitudes
below 1000 feet (305 m))

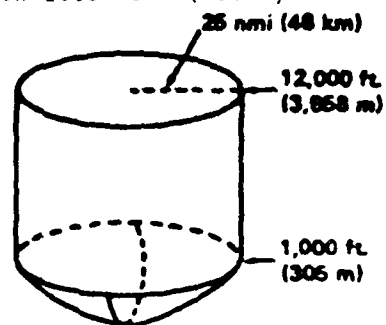


Figure 15. Standard Terminal
Service Volume [15]

be usable. Distance information provided by DME will permit satisfactory performance of airborne components from the radio horizon up to an elevation angle of 60 degree.

The current VOR/DME locations in the United States are shown in Figure 18.⁹

VOR/DME Error Models

In Reference 15, the VOR bearing signal is modeled as equal to true bearing plus local magnetic deviation from North plus the error term composed of components due to the receiver, transmitter, and course roughness. The receiver component consists of Gaussian distributed random bias with zero mean and standard deviation of 0.2 degree. The transmitter error is also modeled as Gaussian distributed bias with zero mean and standard deviation of 0.15 degree. The course roughness component is treated as colored noise with correlation time inversely proportional to aircraft ground speed, or

$$E\{N_c(t)N_c(t+\tau)\} = \sigma_c^2 e^{-V_g \tau / 250} \quad (4)$$

Here, the standard deviation σ_c is 0.2 degree, and V_g is ground speed, in kt.

Also, in Reference 15, the DME signal is modeled as slant range plus white and colored noise error terms. The white noise error terms have a Gaussian distribution with zero mean and standard deviation which is the greater of 0.5 nmi or 3% of the slant range. The colored noise term has a standard deviation of 0.1 nmi and a correlation time constant of 4000 sec. This represents a slowly varying bias like error.

Table 7 summarizes the current error model and its parameters for the VOR/DME simulation on NASA Ames helicopter simulators. Both the Crow's Landing TACAN and the Stockton Vortac are simulated. The error equations are similar to Eq. (1) and both high frequency random noise ($\tau = 1$) and low frequency ($\tau = 500$) bias like terms are used.

LORAN-C

General Characteristics

Loran-C is a hyperbolic system of radionavigation available throughout much of the Northern Hemisphere. Ships and aircraft can use Loran-C in all weather conditions to obtain high accuracy position information. The inherent accuracy capabilities of the system make it suitable for general purpose or for precision radionavigation, and for a wide variety of radiolocation purposes. The range capabilities of the system make it particularly desirable in remote areas where suitable transmitting sites are limited and where coverage of vast areas is required.¹⁶

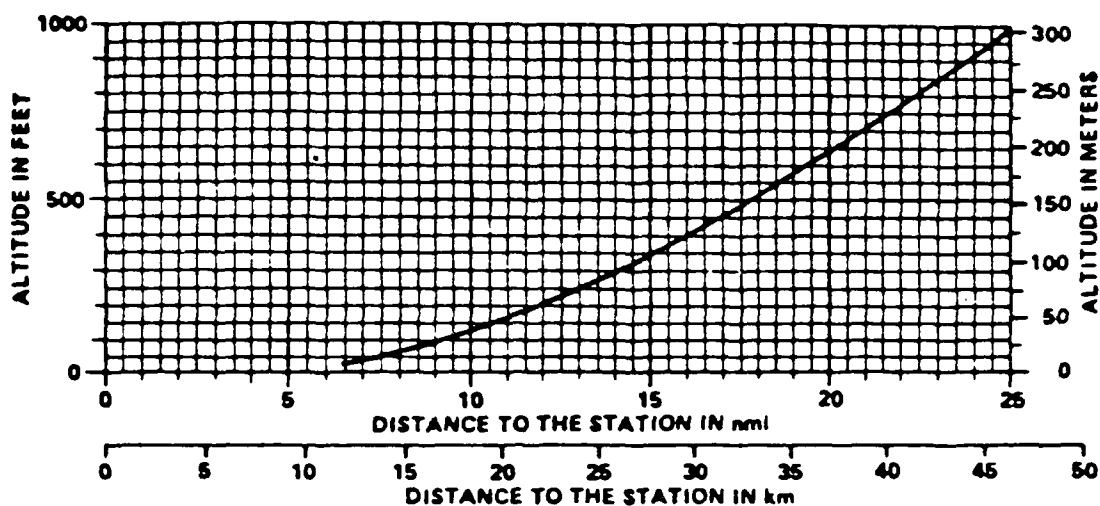


Figure 16. Definition of the Lower Edge of the Standard T (Terminal) Service Volume [15]

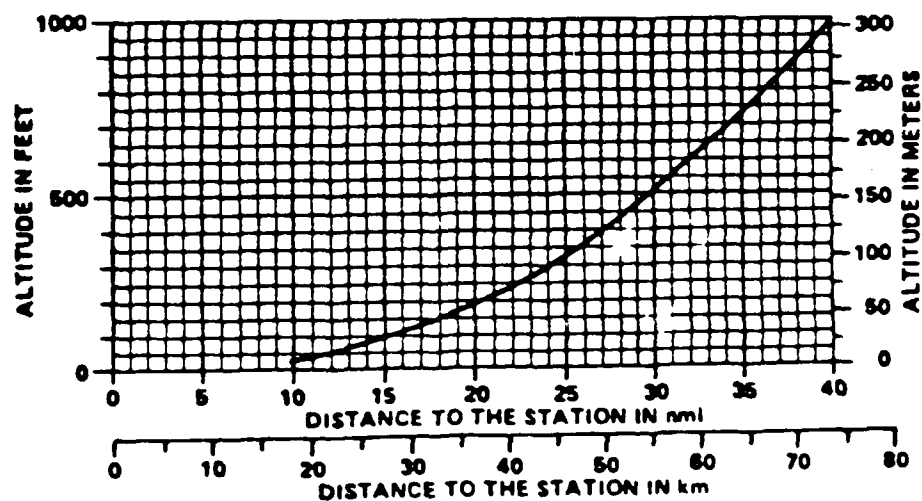


Figure 17. Definition of the Lower Edge of the Standard H (High) and L (Low) Service Volumes [15]

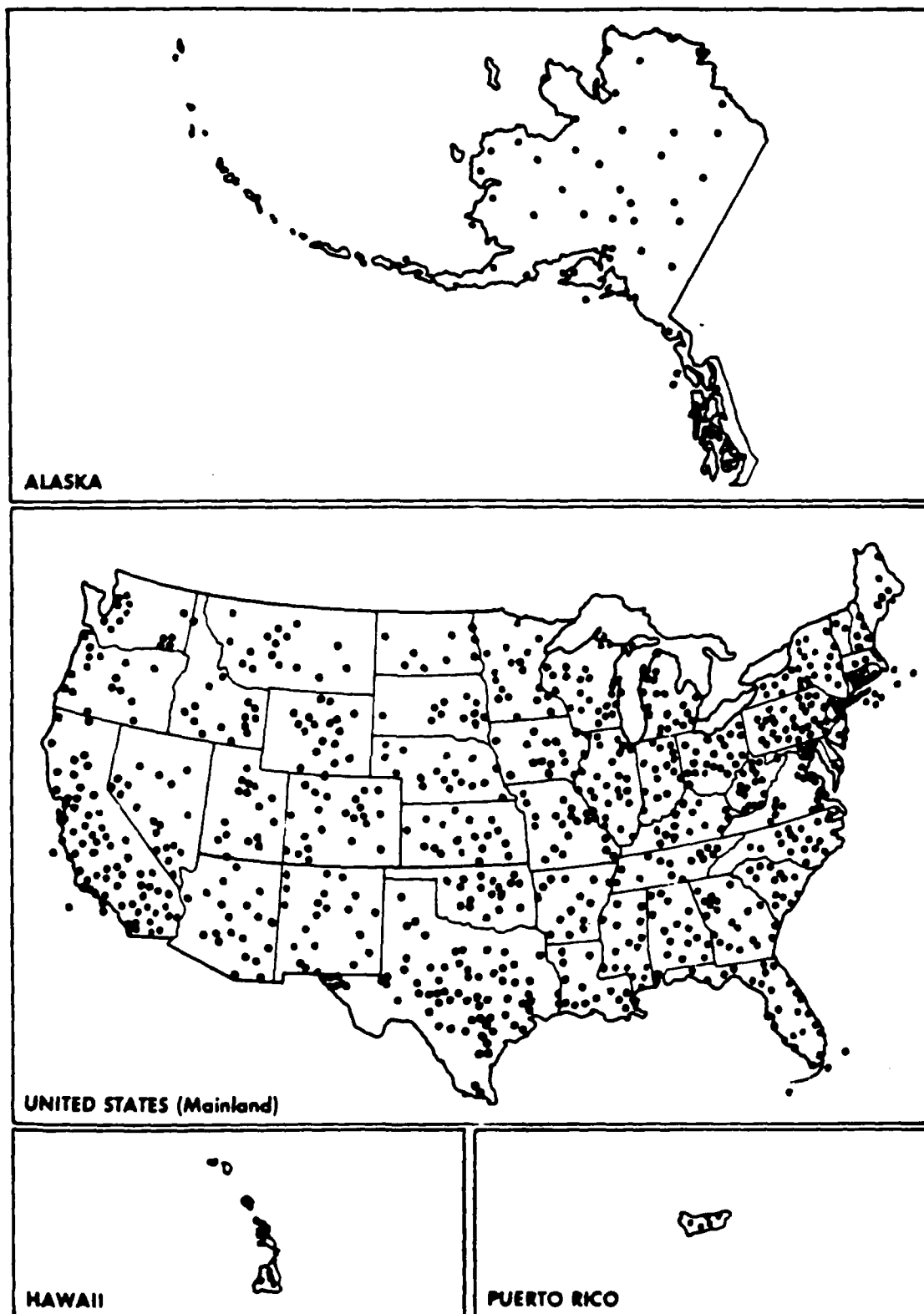


Figure 18. Current Locations of VOR and DME station in the U. S. [9]

Table 7. Discrete Ames Helicopter Simulation
Equations for Tacan and Vortac

Error Equations (8 equations of generic form):

$$B_{1i}(n+1) = K_1 B_{1L}(n) + \sigma_i \sqrt{1-K_1^2} \eta_i$$

i = Vortac VOR random (vvr) and bias (vvb)

Vortac DME random (vdr) and bias (vdb)

Tacan VOR random (tvr) and bias (tvb)

Tacan DME random (tdr) and bias (tdb)

Range (DME)

$$R_e = R + B_{1vdr} + B_{1vdb} \text{ or } = R + B_{1tdr} + B_{1tdb}$$

Bearing (VOR)

$$B_e = B + B_{1vvr} + B_{1vvb} \text{ or } = B + B_{1tvr} + B_{1tvb}$$

Noise Characteristics:

η_i = white, zero-mean Gaussian noise with $\sigma = 1$.

Standard Deviations

Vortac:

$$\sigma_{vvr} = 0.3^\circ; \sigma_{vvb} = 0.35^\circ; \sigma_{vdr} = 12 \text{ ft}; \sigma_{vdb} = 850 \text{ ft}$$

Tacan:

$$\sigma_{tvr} = 0.59^\circ; \sigma_{tvb} = 0.762^\circ; \sigma_{tdr} = 12 \text{ ft}; \sigma_{tdb} = 850 \text{ ft}$$

Noise shaping gain: $K_1 = e^{-\Delta t/\tau}$; Δt = time step.

Time constant: random $\tau_{ri} = 1 \text{ sec}$; bias $\tau_{bi} = 500 \text{ sec}$

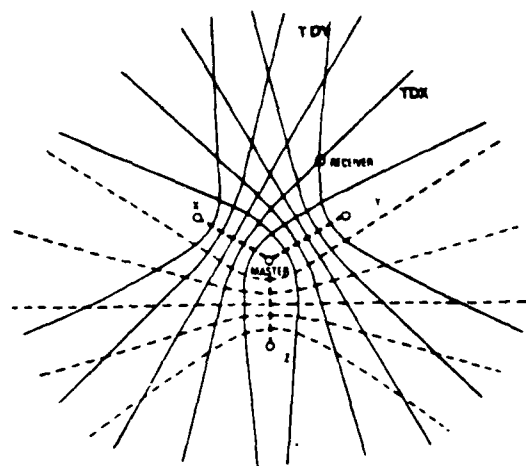
A group of Loran-C stations transmitting synchronized pulse signals at a common repetition rate is called a chain. One station is designated the "master" and the others are designated "secondaries." In the original and conventional mode, a Loran-C user receiver measures the time difference (TD) between the master station and a secondary station X signals; this defines a hyperbolic line of position TDX, as shown in Figure 19a. Measurement between the master signal and another secondary Y defines a second line TDY, and the receiver location is the intersection. A third secondary Z provides coverage for other receiver locations where one of the other secondaries does not provide either good signals, closely spaced hyperbolas, or good crossing angles. There may be up to five secondaries synchronized to one master, where geography is less favorable.¹⁶

Loran-C signals are radio-frequency pulses, as shown in Figure 19b. At 100 kHz, the carrier cycles are 10 sec long--conventional to high receiver phase-measurement accuracy is 0.01 to 0.001 cycles representing timing accuracy of 100 to 10 nsec. For conventional Loran-C operation, the ground-wave signal is utilized for highest accuracy, and measurements are made at the end of the third cycle to prevent contamination by the sky wave which travels a longer path. To select the desired cycle crossing, the receiver also makes measurements of the arrival time of the pulse envelope. All Loran-C stations transmit at the same radio frequency, and the pulse rise and fall are controlled to confine 99 percent of the transmitter energy to the 90-110 kHz allocated band. The unused trailing edge is deliberately made less steep to minimize sideband energy.

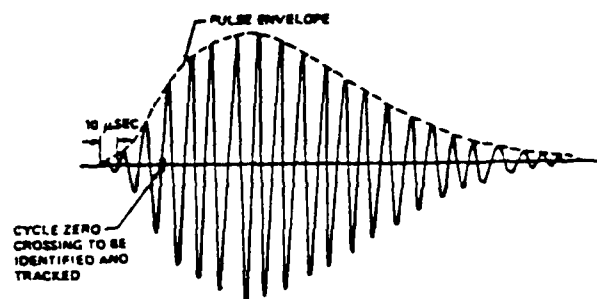
To eliminate mutual interference between the stations of a chain, signals are transmitted on a time-shared basis, with timing chosen to provide guard regions against signal overlap anywhere in the system. To achieve higher average power, a group of eight pulses is sent from each secondary station, with 1000 sec between pulses.

The duration of the pulse pattern is known as the Group Repetition Interval (GRI) defined in Figure 19c. Different GRI are utilized to distinguish chains and minimize mutual interference between chains. The GRI are between 40000 and 99000 μ sec in multiples of 10 μ sec; the GRI designator is the number of microseconds divided by 10. Some stations are double pulsed and operate as a member of two chains on two GRIs.

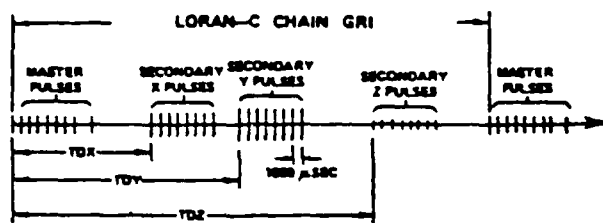
Geometry plays an important factor in Loran-C accuracy. Figure 19a shows that as the receiver departs from the area between the stations the lines diverge. Also the crossing angles of the lines of position get smaller. This results in reduced positional accuracy for a given time-measurement accuracy at longer ranges, commonly called Geometrical Dilution of Position (GDOP). The GDOP for Figure 19a is shown in Figure 19d. The parameter on the curves is the Circular Error Probability (CEP)--radius of the circle containing 50 percent of the positional errors for a standard deviation (67 percent error) of 0.1 sec in each of the two time differences. The contours and CEP are dependent just upon the geometrical configuration and are independent of distance scale.



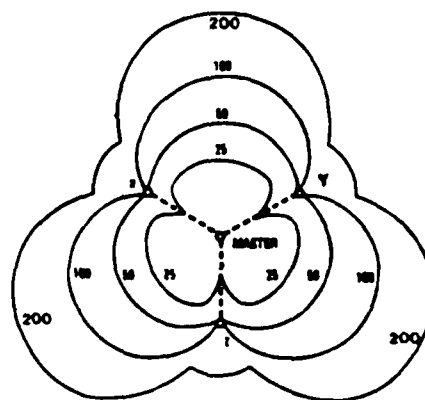
a. Loran-C station chain with hyperbolic lines of position



b. Loran-C pulse detail



c. Loran-C pulse pattern



d. Fix accuracy—CEP contours in meters for 0.1-μs standard deviation line of position error

Figure 19. Loran-C Signal Characteristics [17]

Figure 20 show the coverage provided by the Southeast U.S. Loran-C chain. The dashed lines show the limits of coverage where the accuracy is within 0.25 nmi on a 95% basis. Figure 21 shows similar U.S. and Canadian Loran-C coverage.

Since the inception of Loran-C, it has been recognized that precision depends upon a detailed understanding and calculation of the velocity of 100 kHz radio propagation over the earth's surface. The effective phase velocity was found to be a function of the characteristics of the over-earth path and also of weather conditions. To obtain highest accuracy in Loran-C, it has been necessary to consider the following factors:

1. Primary factor - correction for propagation through the atmosphere as opposed to propagation through space.
2. Secondary factor (SF) - the amount by which the Loran-C signal is additionally delayed by propagation over an all sea-water path.
3. Additional secondary factor (ASF) - the amount by which the Loran-C signal is additionally delayed by propagation over terrain of various conductivities and profiles.

The method presently used by the government responsible for Loran-C charts is to use best estimates of land conductivity to calculate ASF, and to adjust these conductivities on the basis of time-difference calibration measurements to achieve a best fit.¹⁷

A Loran-C receiving set receives radio waves transmitted by Loran-C transmitting stations and processes these signals to provide the user with a measurement of the time of arrival of the signals at the receiver site. This involves many signal processing steps, starting with the reception of the signals by the receiver antenna and ending with the output from the receiver of the desired time or position information. Reference 18 presents a functional description of a typical Loran-C receiver, with the goal of providing insight into the processing which is accomplished within the receiver.

The Loran-C system is now fully operational and covers not only U.S. coastal areas and other waterways, but also about two-thirds of the land area of the coterminous 48 states. As a consequence, it is anticipated that Loran-C will be used increasingly to provide position location information on land. To extend the coverage for this purpose to the entire coterminous states will require additional stations. The number of stations may have to be further increased to provide adequate signals over the entire U. S. if Loran-C is an acceptable common system replacement for aviation. National and international agreements would be required to adopt Loran-C as the short-distance navigational system standard.¹⁶

LORAN-C

SOUTHEAST U.S. CHAIN

GRI 7880

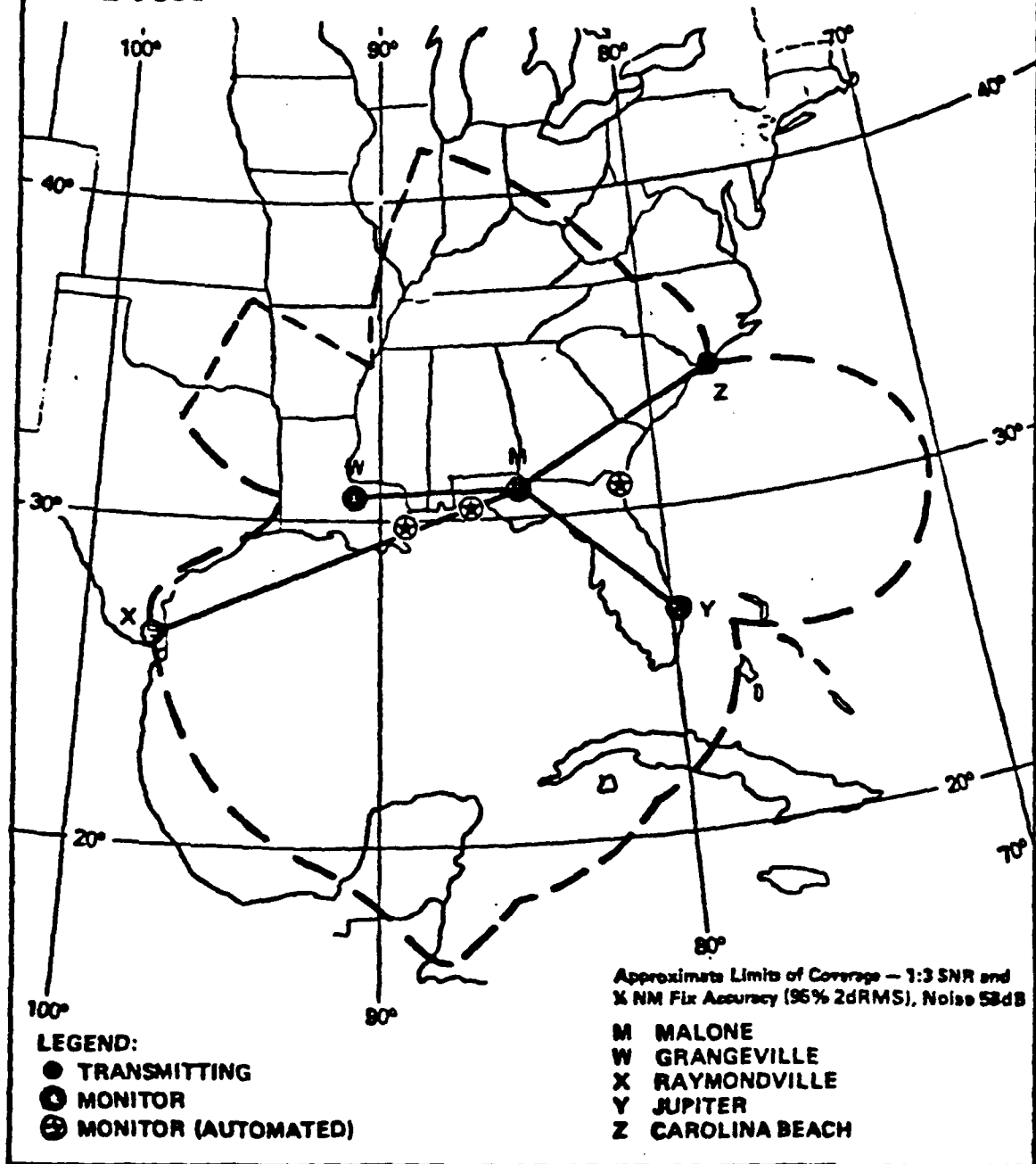


Figure 20. Loran-C Southeast U. S. Chain Coverage [22]

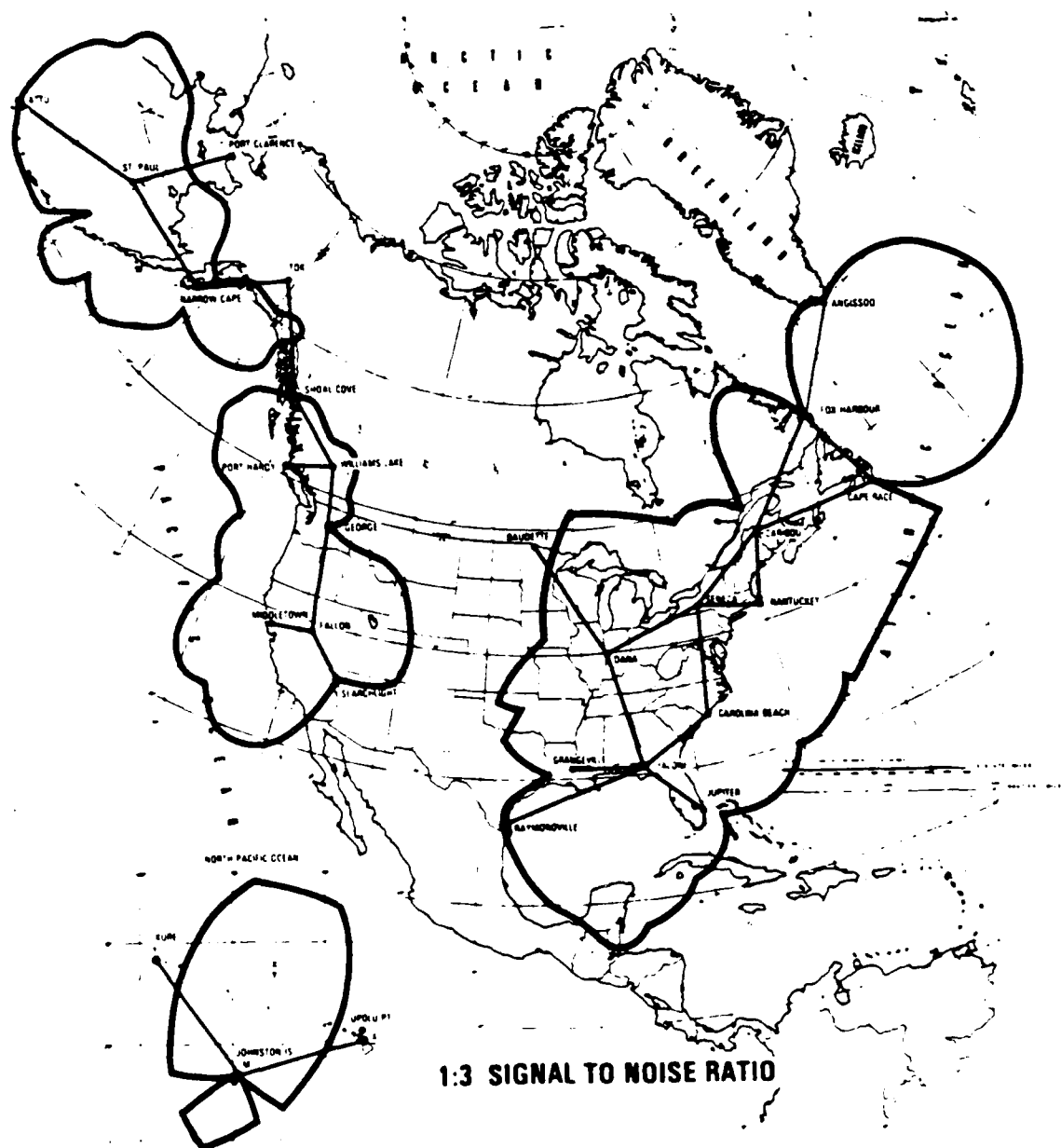


Figure 21. U. S. Loran-C Coverage [25]

The FAA Loran-C program addresses the issue of Loran-C signal availability and reliability; the performance of the Loran-C system for enroute, terminal, and non-precision approach operations; and the feasibility of developing low-cost avionics, particularly for general aviation. This is part of a joint effort between the FAA and the U.S. Coast Guard which includes establishing a Loran-C data base, developing low-cost avionics equipment, developing geographical grid corrections, and determining the impact of using Loran-C navigation in the air traffic control system and flight inspection procedures.¹⁶

Flight Test Accuracy Analysis

Several flight tests have been made to determine the accuracy of the Loran-C signal in terms of its ability to meet the requirements for area navigation as specified by the FAA Advisory Circular AC90-45A. This document defines flight test errors according to those terms diagrammed in Figure 22. Flight Technical Error (FTE) refers to the accuracy with which the pilot controls the aircraft as measured by his success in nulling deflections of the Course Deviation Indicator (CDI). The Total System Cross Track (TSCT) Error is the root-sum-square of FTE and Cross Track Error (CTE). Both CTE and Along Track Error (ATE) are position errors resulting from error contribution of both the airborne and ground equipment.

A series of flight tests were made starting in 1979 in the state of Vermont using a Beech E50 aircraft. The intent was to obtain a Supplemental Type Certificate (STC) for the use of a Loran-C navigation system in the National Airspace System.¹⁸ During the test period, 76 approach segments, 101 terminal segments, and 66 enroute segments were flown within range of a precision reference system. The results of these tests in terms of the FTE, CTE, ATE, and TSCT are presented in Table 8 in comparison with the requirements of AC90-45A. Measured performance was shown to exceed the minimum requirements specified for area navigation in AC90-45A for all phases of flight. Based on these results, the STC was issued to the State of Vermont. Also, no degradation in navigation accuracy or functional performance was observed when the Loran-C navigation system was compared to the VOR/DME system in the aircraft.

Reference 20 reports results of 1979 flight tests made within the West Coast Loran-C chain. In particular, approach tests were made in the vicinity of South Lake Tahoe, California, Klamath Falls, Oregon, Grand Junction, Colorado, and Reno, Nevada. A total of 24 non-precision approaches were made to the corresponding airports. Some inherent problems with Loran-C were evident during the test including bias shifts, GDOP effects, and signal propagation errors. These errors caused the along track and cross track inaccuracies to exceed the AC90-45A approach requirements.

The West Coast test results are summarized in Table 9. Table 9a presents the mean and two standard deviation along track and cross track errors. Table 9b compares the results with the AC90-45A approach criteria. Table 9c

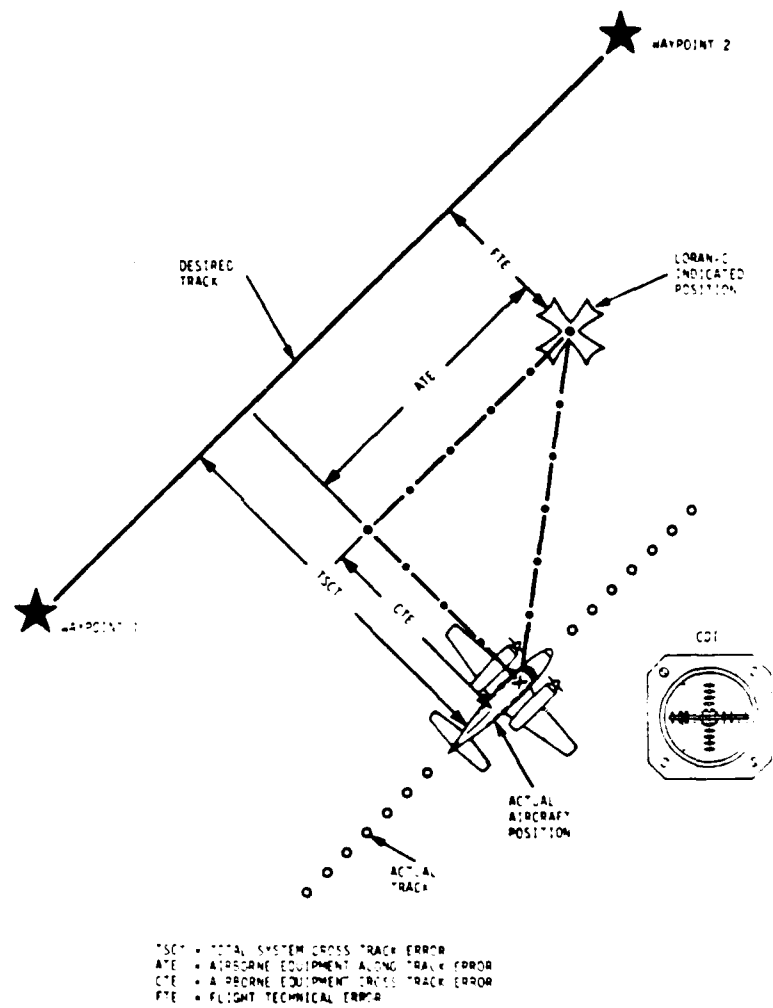


Figure 22. Loran-C Flight Test Error Definitions [19]

Table 8. Loran-C Flight Test Errors for Vermont Flight Tests [19]

d. — Aggregated error data for all approach segments

Approach	Total System Error				FTE—Flight Technical Error		CTE—Equipment Error	
	TSAT—Along Track		TSCT—Cross Track		RQD	Meas	RQD	Meas
	RQD	Meas	RQD	Calc ¹				
31 Flights	0.3 nm	0.16 nm	0.6 nm	0.32 nm	0.5 nm	0.28 nm	0.33 nm	0.15 nm
76 Seg-ments		11,198		17,949		17,949		11,229
Number of Measure-ments								

¹ TSCT = $\sqrt{(FTE)^2 + (CTE)^2}$.

b. — Aggregated error data for all terminal segments

Approach	Total System Error				FTE—Flight Technical Error		CTE—Equipment Error	
	TSAT—Along Track		TSCT—Cross Track		RQD	Meas	RQD	Meas
	RQD	Meas	RQD	Calc ¹				
25 Flights	1.1 nm	0.15 nm	1.5 nm	0.60 nm	1.0 nm	0.58 nm	1.12 nm	0.16 nm
101 Seg-ments		12,408		22,539		22,539		12,419
Number of Measure-ments								

¹ TSCT = $\sqrt{(FTE)^2 + (CTE)^2}$.

c. — Aggregated error data for all en route segments

En route	Total System Error				FTE—Flight Technical Error		CTE—Equipment Error	
	TSAT—Along Track		TSCT—Cross Track		RQD	Meas	RQD	Meas
	RQD	Meas	RQD	Calc ¹				
29 Flights	1.5 nm	0.12 nm	2.5 nm	0.73 nm	2.0 nm	0.71 nm	1.5 nm	0.15 nm
66 Seg-ments		23,127		45,449		45,449		23,116
Number of Measure-ments								

¹ TSCT = $\sqrt{(FTE)^2 + (CTE)^2}$.

Table 9. Results of West Coast Loran-C Flight Test [20]

a. Navigation Sensor Error Performance

	CROSS TRACK		ALONG TRACK	
	Mean	2 σ	Mean	2 σ
AC90-45A REQS	---	.30	---	.30
Klamath Falls (FMG)*	.07	.24	.04	.13
Lake Tahoe (FMS)	-.33	.11	.39	.27
Lake Tahoe (FMG)	.17	.15	-.48	.22
Grand Junction (FGS)	-.21	.40	.00	.15
Reno (FMS)	-.11	.09	.76	.33
Stead (FMG)	.20	.45	.22	.26
Stead (FMS)	-.85	.19	-.18	.37
Test Aggregate	-.10	.49	.14	.71

*F - Fallon, Nev.
M - Middletown, Cal.

G - George, Wash.
S - Searchlight, Nev.

b. Comparison of Results with AC90-45A

	AC 90-45A Approach Criteria (2 σ)		Loran-C Test Results (2 σ)	
	Cross Track	Along Track	Cross Track	Along Track
Airspace(TSCT)	0.6	0.3	0.50	0.71
FTE	0.5	---	0.37	---
Loran-C	0.3	0.3	0.49	0.71

c. Comparison with Biases Removed

	AC 90-45A Approach Criteria (2 σ)		Bias-Corrected Test Results (2 σ)	
	Cross Track	Along Track	Cross Track	Along Track
Airspace (TSCT)	0.6	0.3	0.31	0.22
FTE	0.5	---	0.35	---
Loran-C	0.3	0.3	0.21	0.23

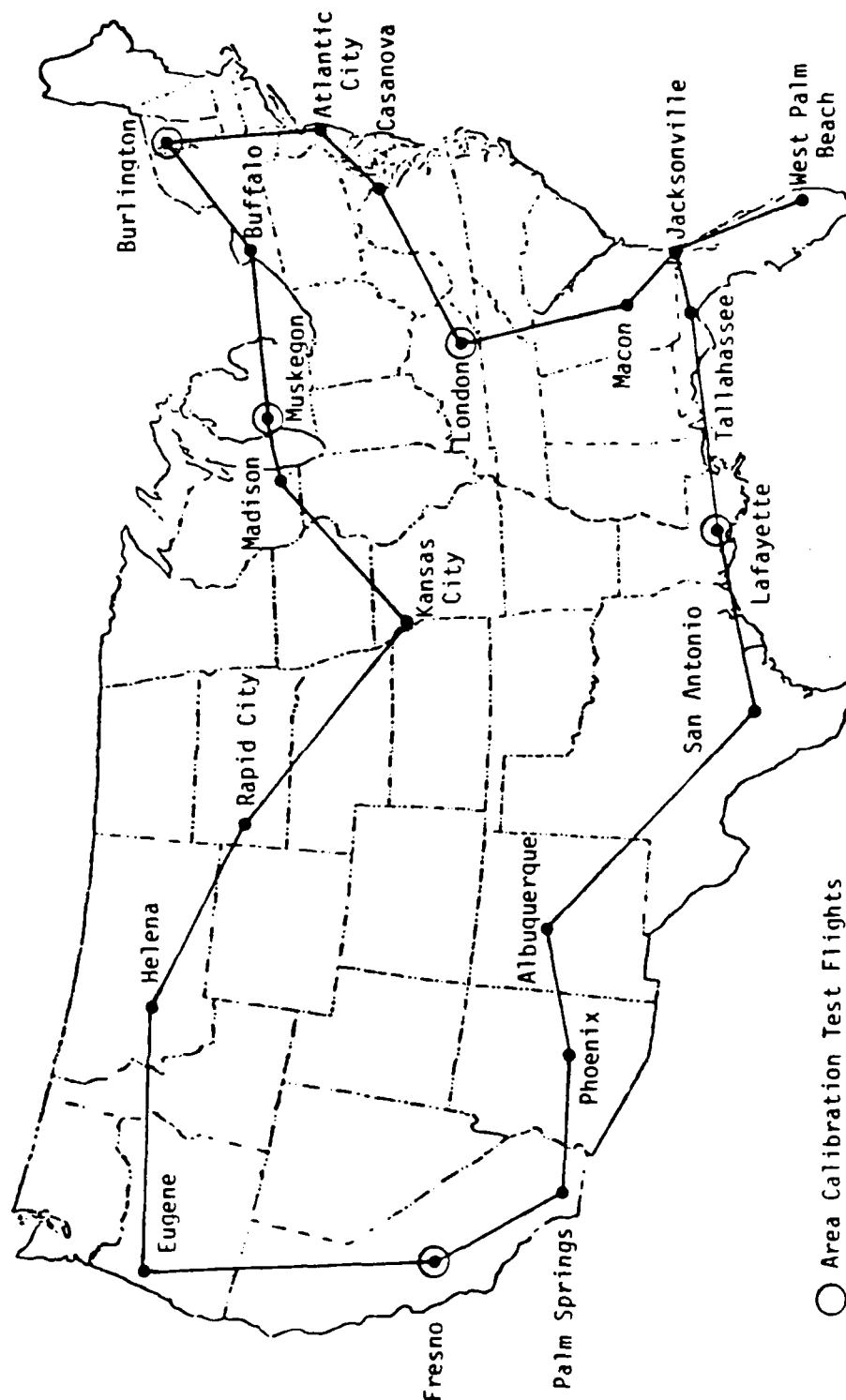
compares the results if the biases are systematically removed. In the latter case, the error results are acceptable. This indicates the need to remove location dependent biases as part of the Loran-C avionics function.

Reference 21 reports results of 1982 flight tests made in Alaska using the North Pacific Loran C chain. Here, the navigation error results were mixed. Around Nome, Bethel, Aniak, and King Salmon, the system met or exceeded the enroute accuracy requirements of AC90-45A. However, the system performed poorly near Anchorage and Fairbanks. Much calibration work needs to be done to use Loran-C in these vicinities for non-precision approaches.

Reference 22 reports results of a 1983 flight test around the United States following the route shown in Figure 23. The route segments were chosen so that all stations in each of the four U.S. Loran-C chains were used during the test. In addition, five calibration paths were flown to evaluate area calibration procedures in a localized area. The calibration flight pattern is shown in Figure 24. Cities where calibration tests were made are shown in Figure 23.

The flight test and subsequent analysis of the recorded data produced the following results:

1. Loran-C signals were received on all segments of the test, even those in the "midcontinental gap" area. However, the Loran-C geometry is very poor in some of these areas, particularly in the southwestern United States, which produced large navigation errors.
2. Navigation errors measured during the enroute phase of the test, in areas of both good and poor geometry, were worse than the enroute requirements of FAA AC90-45A for the non-VOR/DME systems. In areas of good geometry only, navigation errors were better than the requirements of AC90-45A.
3. The largest source of navigation error was due to propagation modeling error. These errors tend to look like bias errors in a given operational area.
4. Cycle errors, caused by misidentification of the third cycle zero crossing of the Loran-C signal, were observed on three separate occasions during the test.
5. Outages at the Loran-C transmitters, both of a momentary nature and of longer duration, were correlated with outages of the airborne receiver. A few short duration receiver outages were correlated with rain and thunderstorm activity.



○ Area Calibration Test Flights

Figure 23. Loran-C Flight Test Route [22]

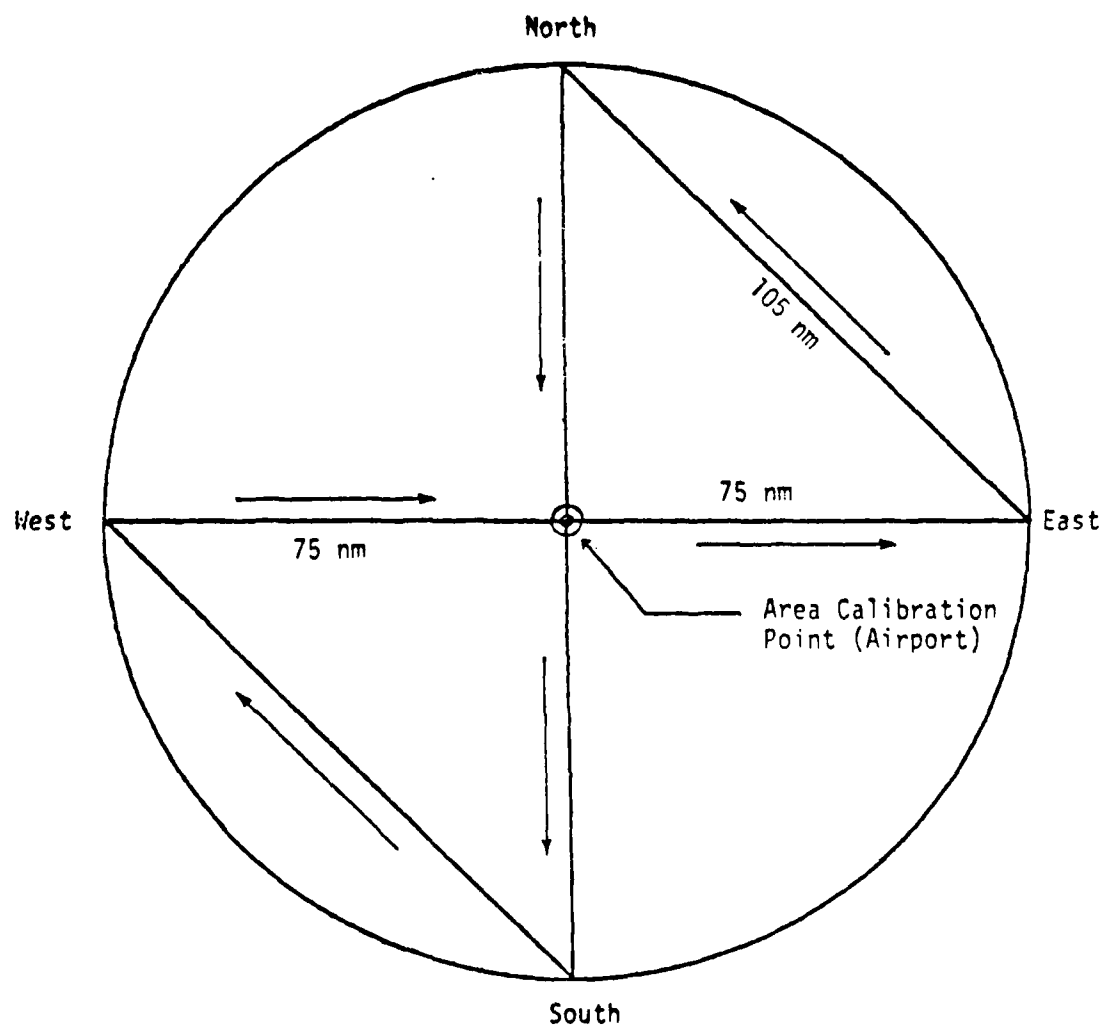


Figure 24. Area Calibration Pattern (75 nm Radius of Validity) [22]

At five locations, the calibration procedure permitted the operator to insert a correction factor into the receiver to remove system bias errors at the calibration point. The following results were obtained during these tests:

1. The calibration procedure reduced navigation errors throughout the 75 nmi radius calibration point. After calibration, errors were reduced to a level where both enroute and terminal area requirements of AC90-45A were met at all test locations. In addition, the accuracy very nearly met the requirements for non-precision approach throughout the calibration area.
2. In some calibration tests the correction factor, which was inserted on the ground at a known location, did not totally remove all time difference error at the calibration point as determined from the airborne measurements. These differences may be due to errors in the reference point location or local disturbances in the Loran-C grid near the calibration point. The differences, measuring over 1 sec in some instances, could produce operationally significant navigation errors if Loran-C were to be used for instrument approach procedures.²³

Typical Loran-C crosstrack and along track errors are shown in Figure 25. As can be seen, the along track errors tend to be slowly varying biases. The crosstrack errors have a mean bias plus oscillatory terms with cycle times of 5-10 minutes. These and similar plots can be used to derive error models for Loran-C simulations when used for study on non-precision approaches. At this time, NASA Ames does not have a Loran-C simulation to be used for helicopter simulator studies; this seems straightforward to develop, though.

The Loran-C system has much promise as an area navigator for helicopter applications, especially to remote areas. Its advantages and disadvantages are summarized in Table 10.

Omega

General Characteristics

Omega is a very-low-frequency (VLF) navigation system operating in the internationally allocated navigation band between 10 and 14 kHz. Eight stations presently provide global coverage. The system is already supporting over 16000 users who are split between the marine and aeronautical communities with the majority now being aeronautical. Receivers range from relatively simple instruments using only one of the frequencies provided by Omega to complex instruments able to receive all frequencies from all eight Omega stations and process this information to readout directly in latitude and longitude. Commercial acceptance has been particularly rapid in the airborne community within the last several years.²⁴

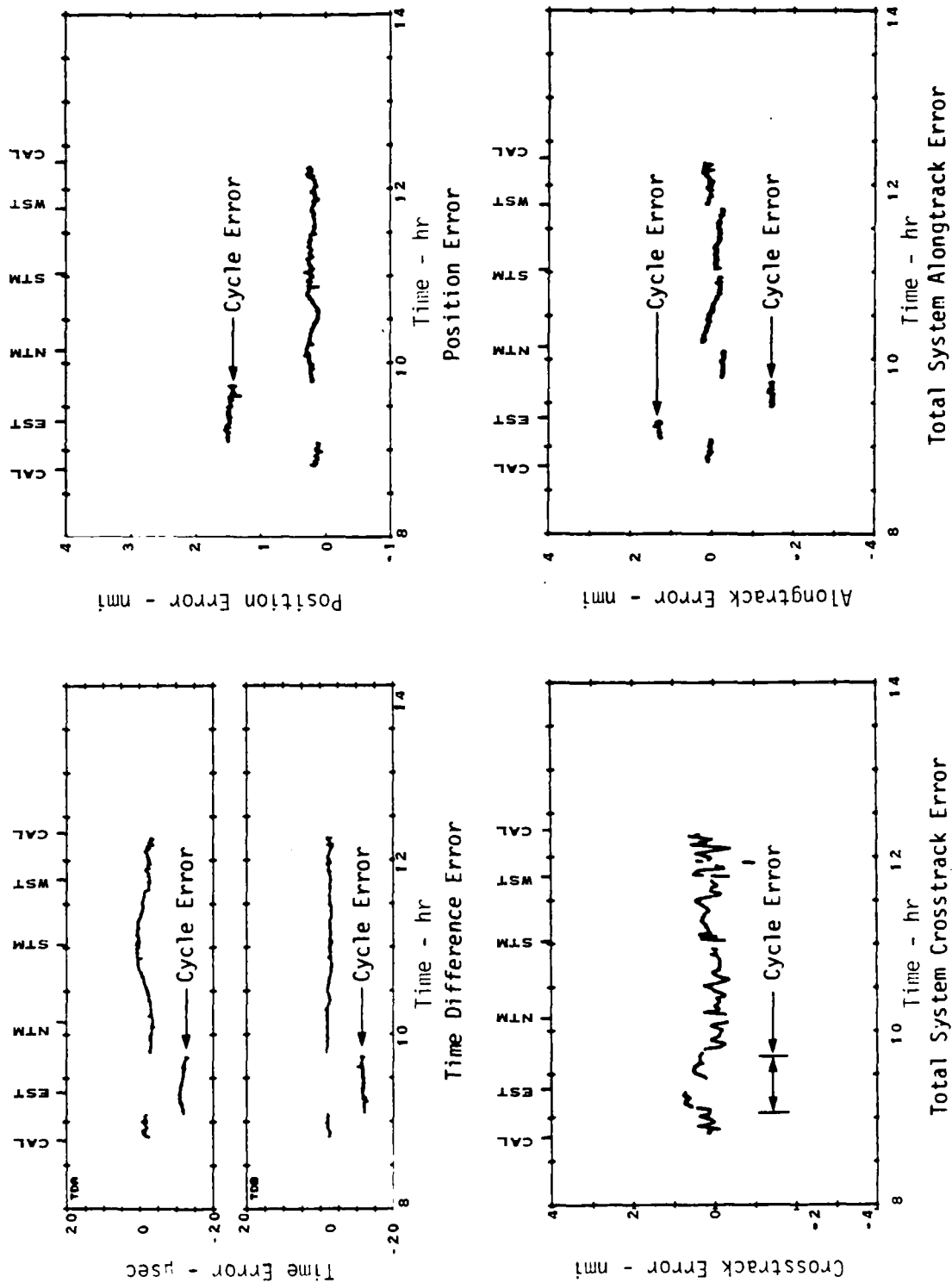


Figure 25. Calibration System Errors, London, KY (July 6, 1983)[22]

Table 10. Loran-C Advantage Summary²³

Advantages	Disadvantages
Low Cost	No coverage in U. S. Central and Rocky Mountain states and in many other parts of the world.
No line-of-sight problem	Accuracy poor near two station baseline.
Good accuracy for Area Navigation	Anomalies in propagation.
Available in most areas	Errors in waypoint or station selection could be catastrophic.
Easy to use	

Omega utilizes continuous wave (CW) phase comparison of skywaves from pairs of stations. The stations transmit time shared signals on four frequencies: 10.2 kHz, 11.33 kHz, 13.6 kHz, and 11.05 kHz. In addition to these common frequencies, each station transmits a unique frequency to aid station identification and to enhance receiver performance.²⁵

In the 10.2 kHz Omega system, isophase lines or lanes are formed about every 8 nmi. A user of the Omega system must know his position within the accuracy of his lane width or he will have an ambiguous position. Ambiguous lines of position (LOPs) occur as there are no means to identify particular points of constant phase difference which recur throughout the coverage area. A two-frequency receiver, using also the 13.6 kHz LOPs, can provide lanes 24 nmi apart by using the beat between the 10.2 and 13.6 kHz signals. Multiple-frequency receivers extend the lane width, for the purpose of resolving lane ambiguity. Lane widths of approximately 288 nmi along the base line can be generated with a four-frequency receiver.

Because of the lane ambiguity, a receiver must be preset to a known location at the start of a trip. The accuracy of that position must be known to sufficient accuracy to be within the lane that the receiver is capable of generating. Once set to a known location, the Omega receiver counts the number of lanes it crosses in the course of a voyage. This lane count is subject to errors which may be introduced by an interruption of power to the receiver, changes in propagation conditions near local sunset and sunrise and other factors. To use the single frequency Omega receiver effectively for navigation, it is essential that a dead reckoning position plot be carefully maintained and the Omega positions compared to it periodically so that any lane ambiguities can be detected and corrected.

The inherent accuracy of the Omega system is limited by the accuracy of the propagation corrections that must be applied to the individual receiver

readings. The corrections may be obtained in the form of predictions from tables or automatically in computerized receivers. The system was designed to provide a predictable accuracy of 2 to 4 nmi (2 drms). That accuracy depends on location, station pairs used, time of day, and validity of the propagation corrections.

Propagation correction tables are based on theory and modified to fit monitor data taken over long periods for localized areas. An extensive monitoring program is in use to verify the propagation model used to predict the corrections and the system accuracy in the area of the network stations. A number of permanent monitors will be maintained to update the model on a long-term basis. The system currently provides coverage over most of the earth. The specific accuracy attained depends on the type of equipment used as well as the time of day and the location of the user. In most cases, the accuracies attained are consistent with the 2-4 nmi system design goal.

A differential Omega system has been developed and there are approximately 15 stations in operation primarily in Europe. The differential Omega stations operate on the principal of a local area monitor system comparing the received Omega signal with the predicted signal for the location and then transmitting a correction factor based on the observed difference. The correction factor is usually transmitted over an existing radiobeacon system and can provide an accuracy ranging from 0.3 nmi at 50 nmi to 1 nmi at 500 nmi. The range of transmission of the correction factor varies with the range of the beacon. Reception of the differential Omega signal requires the use of a differential Omega receiver.

There are also a number of U. S. Navy VLF communication stations operating in the 14-30 kHz range that can be used with Omega receivers for navigation. The VLF transmitters emit a phase stable, high power signal. By using a multiple fixed tuned receiver, a common intermediate frequency for phase measurement, and a computer, navigation position can be obtained. The VLF station method is also subject to the lane ambiguity problems discussed above.

The equipment required for Omega/VLF is a receiver/processor, control display unit, and either an E or H field antenna and coupler.

Flight Test Accuracy Results

Reference 26 reports the results of an extensive flight test of an Omega/VLF system to determine its inherent accuracy with respect to AC90-45A requirements for non-VOR systems. The route followed during the test is shown in Figure 26. Aircraft position was established during post flight data processing from the multiple DME distance measurements provided by a scanning DME receiver. Navigation accuracy was determined by comparing the Omega/VLF position and navigation parameters with corresponding parameters derived from the DME position reference system.

The flight and subsequent analysis of the recorded data produced the following results:

1. The overall errors of the Omega/VLF system slightly exceed current enroute requirements for non-VOR/DME area navigation systems as specified in AC90-45A. The quantitative results are shown in Table 11. Accuracy was poor on the night flight segment between Bismarck and Minneapolis due to marginal availability and poor fix geometry of the received signals. The major source of Omega/VLF system error appeared to be the error in deriving aircraft position from the Omega and VLF phase measurements and signal propagation models.
2. Navigation system availability was very good on most flight segments. Two system outages occurred, and they were believed to be caused by loss of synchronization. The Omega/VLF system was not able to resume valid navigation in either instance. The cause of the loss of synchronization could not be determined.

Typical cross track and along track position errors for the Omega/VLF system are shown in Figures 27-28. As can be seen, the cross track errors are oscillatory about zero with amplitude of about 1 nmi and a period of about 10 minutes. The along track error is a slowly varying bias with white noise of about 0.2 nmi superimposed. These error characteristics are similar to those of the Loran-C system shown in Figure 25.

Table 11. Omega/VLF Accuracy (nautical miles) [26]

Error Quantity	Mean (\bar{x})	Standard Deviation (σ)	$\bar{x} - 2\sigma$	$\bar{x} + 2\sigma$	AC 90-45A Requirements
Total System Crosstrack	0.17	1.25	-2.33	2.67	2.50
Total System Alongtrack	-0.63	0.89	-2.41	1.15	1.50

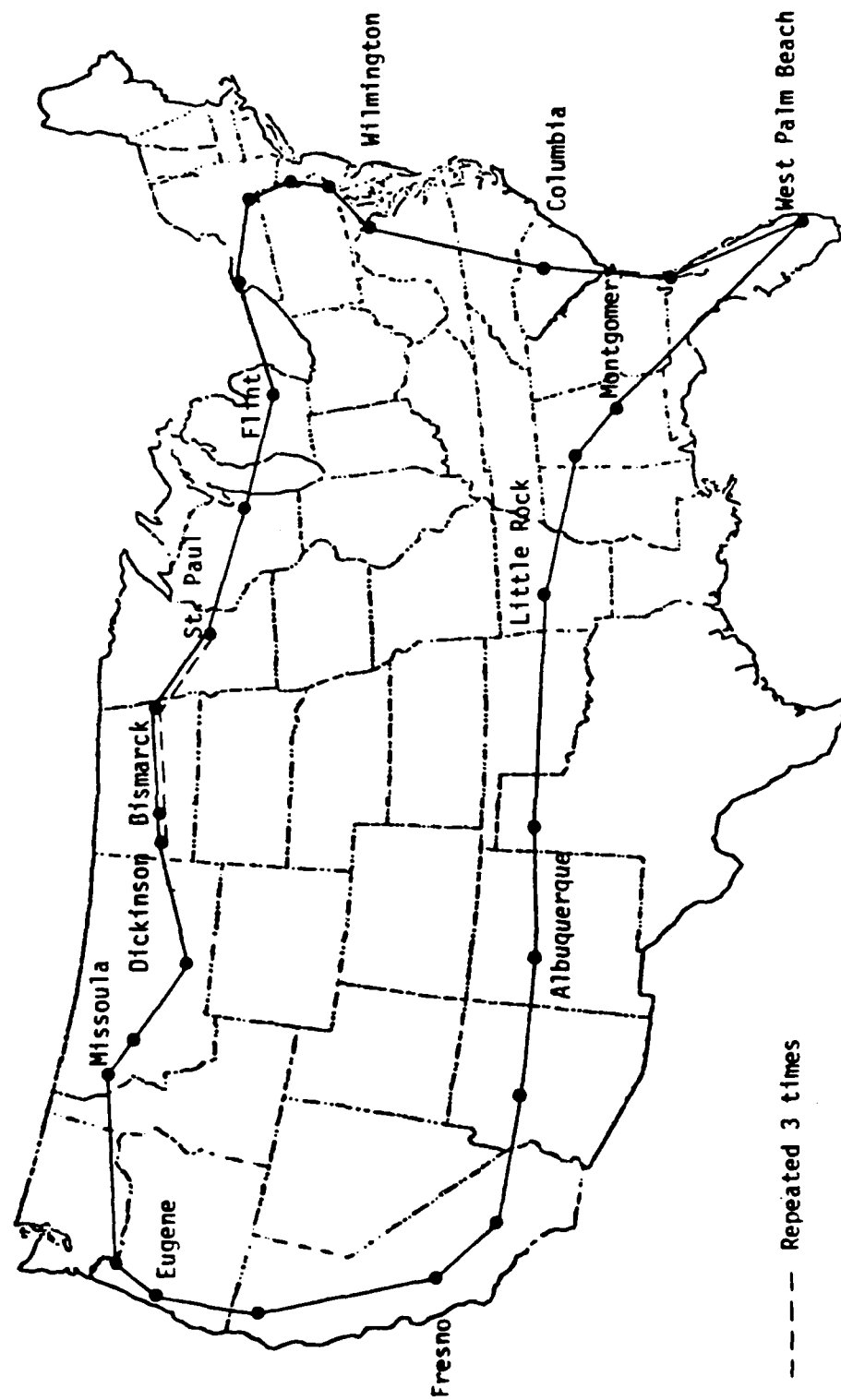


Figure 26. Omega/VLF Flight Test Route [26]

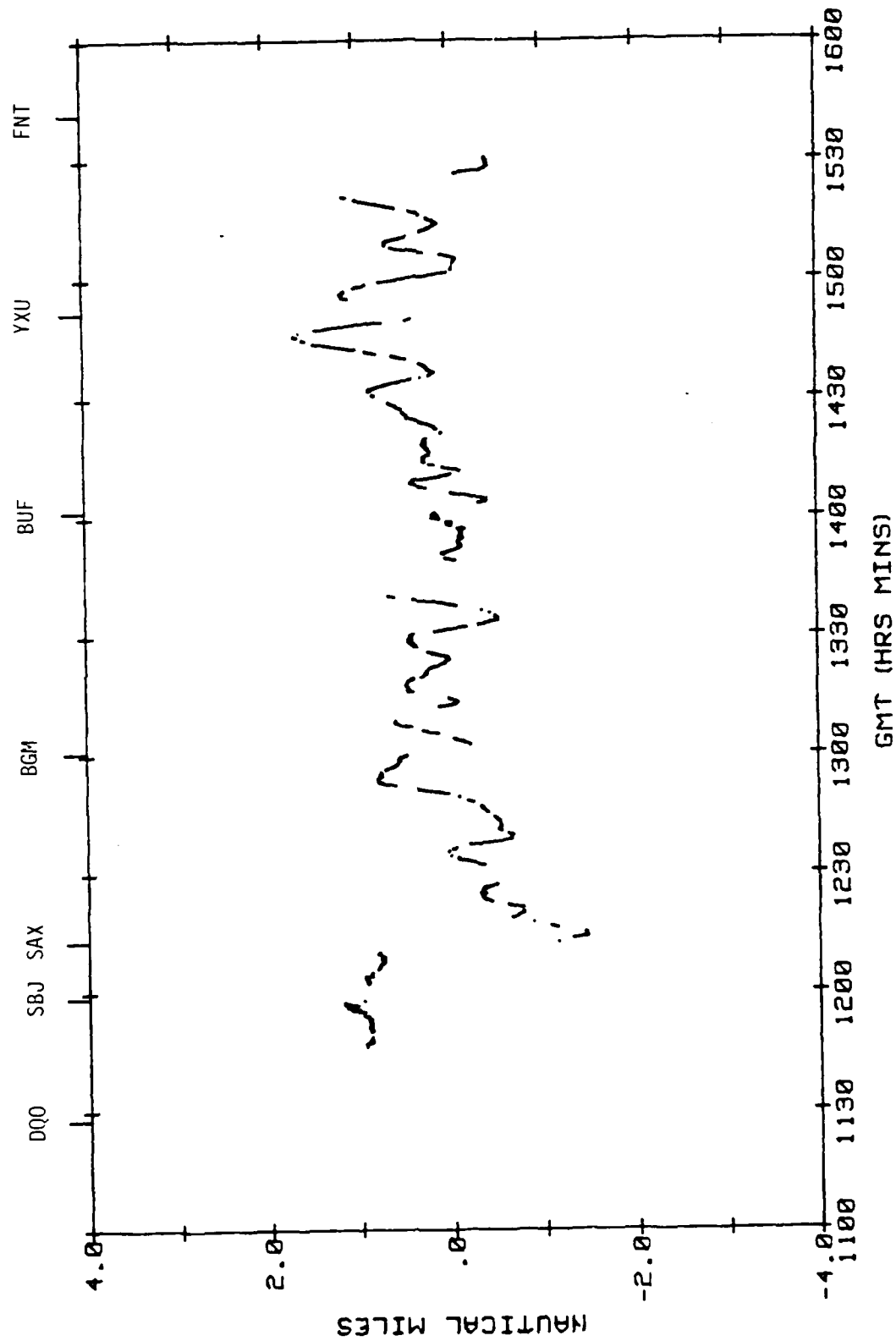


Figure 27. Total System Crosstrack Error for Segment 3,
Wilmington, DE, to Flint, MI (May 10, 1983) [26]

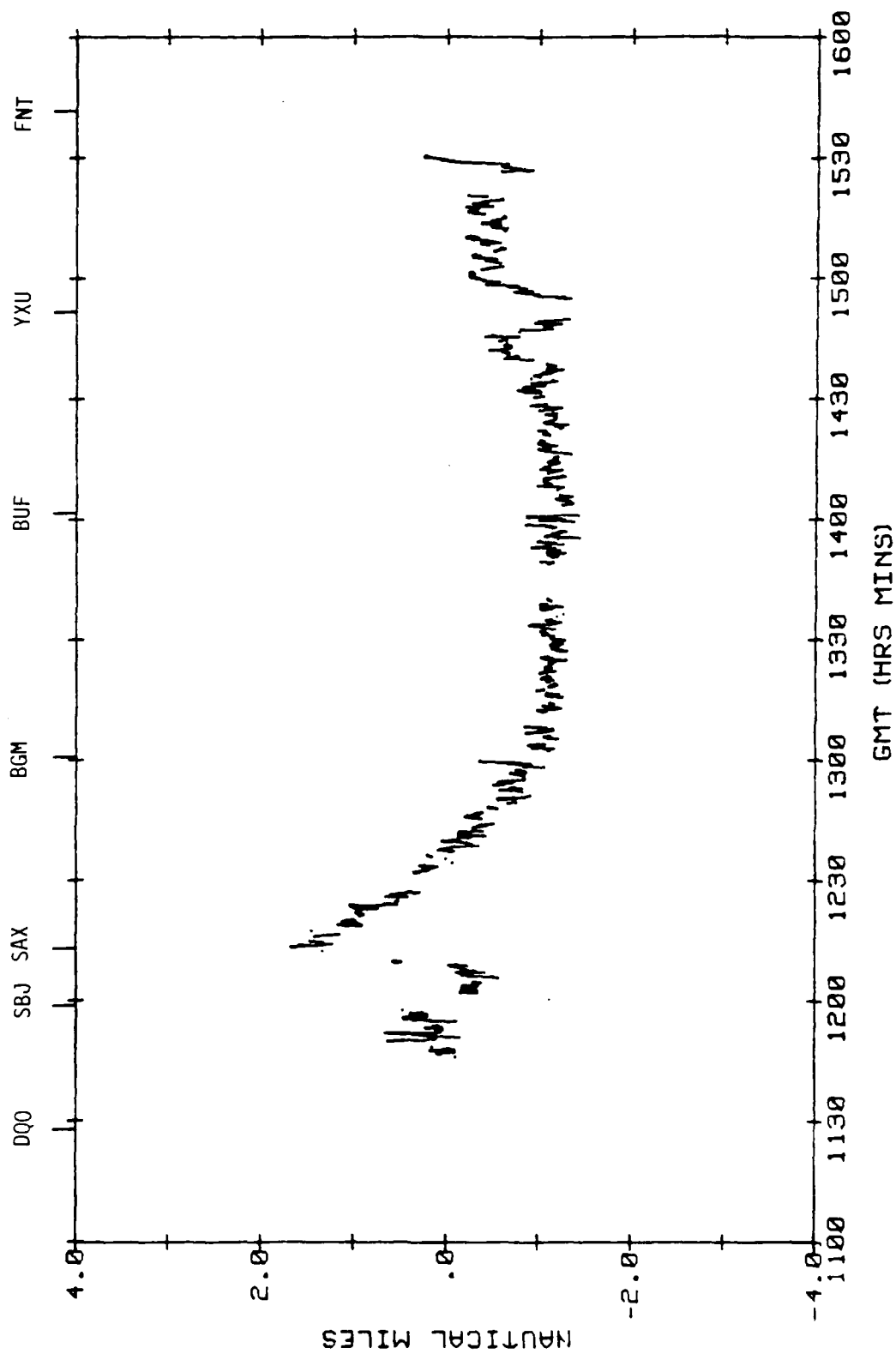


Figure 28. Total System Alongtrack Error for Segment 3, Wilmington, DE, to Flint, MI (May 10, 1983) [26]

There is no known simulation of the Omega system used by NASA for cockpit simulation studies. However, it appears that regular Omega is not accurate enough to be used for approach and non-precision landing studies for helicopters. Not enough is known about differential Omega, and as a future system, GPS navigation will probably replace Omega from further consideration.

GPS

General Characteristics

The Navstar Global Positioning System (GPS) is a satellite-based radio navigation system that will provide extremely accurate position, velocity, and time on a worldwide, continuous basis. It is planned that GPS will be fully operational by 1989, and test capability is available now. GPS will be unaffected by weather and will provide a worldwide common grid reference system.^{25,27,28} The system consists of a space segment, a control segment and a user segment.

When fully deployed, the space segment will consist of 18 satellites in six 12 hour orbits with 3 satellites in each orbit. Each satellite will continuously broadcast a message containing precise information relative to its own position (ephemeris) and clock accuracy and less precise information relative to the entire constellation position (almanac).

The control segment consists of monitor stations and a master control station. The monitor stations transmit satellite tracking data to the master control station, which determines the satellites' orbital parameters and communicates them to the satellites for retransmission to the users.

The user segment consists of the equipment necessary to derive position, velocity and time from the information received from the satellites.

The monitor stations track the signals from all satellites as they make their passes, and relay the information to the Master Control Station which computes a best fit predicted ephemeris and clock model for the next orbit. At the control center, corrections are applied to the range data transmitted from the monitor stations to remove deterministic biases. These include ionospheric delay, tropospheric refraction, general and special relativistic effects, antenna phase center offsets, earth rotation and timetag corrections.

The data are smoothed over a 15-minute interval by editing and fitting the data using a least squares fit. This set of smoothed measurements is then processed by a Kalman estimator in the control center. The output state vector includes orbital element perturbations, solar pressure estimates, satellite clock bias, drift and drift rate, monitor station clock errors, tropospheric residuals, and polar wander residuals. In the final state of this process, clock states are propagated forward and the reference ephemeris is corrected. These become the ephemeris and clock predictions of the

navigation messages for each satellite, which are uplinked to the satellites for continuous broadcast.

The navigation signal is continuously broadcast on a 20 MHz spread spectrum signal centered at the L1 frequency of 1575.42 MHz, and the secondary L2 frequency of 1227.60 MHz. L1 and L2 are the carrier signals for GPS whose frequency doppler shifts can be measured for velocity determination. For position determination, the carriers have high rate bi-phase shift keyed codes superimposed on them, modulating the phase.

There are actually two codes on the carrier: Standard Positioning Service (SPS, also known as Course/Acquisition (C/A)) code with a chip rate of 1.023 MHz, and Precision Positioning Service (PPS, or Precise (P)) code with a chip rate of 10.23 MHz. The SPS code is short, repeating every millisecond. Each satellite broadcasts a different SPS code chosen from a family of 1023 specified codes which allows for minimum interference between SPS signals from the satellites and thus positive satellite identification by the user. The PPS code is a long sequence, repeating every 280 days, and each satellite is assigned a week-long portion of this sequence. In addition, a low rate (50 Hz) navigation message is modulated on the signal which contains the satellite ephemerides, clock modeling parameters, satellite status, ionospheric propagation delay parameters, complete satellite constellation almanac, and a special message block.

The PPS code will be highly protected and denied from common use via encryption, due to its military value. Hence, most civil users will be limited to use of the SPS code, which is intentionally degraded further to assure its lack of value to enemy military operations. This degradation, called "selective availability," is currently designed to provide position accuracy of 100 m (2 drms) horizontally and 156 m (2 drms) vertically²⁵ with the SPS code.

User receivers continuously track any four signals from the six to eight satellites in view at any time to solve the hyperbolic positioning problem for three position coordinates and an unknown user clock bias. User receivers use less precise quartz crystal oscillators which accumulate phase and frequency offsets relative to the more stable cesium satellite clocks. The user must solve for this clock bias using the fourth measurement. In addition, the Doppler shift of the carrier can be measured and used for velocity determination.

The position location is obtained using four "pseudorange" measurements to four satellites. Pseudorange is illustrated in Figure 29. These measurements have errors due to the unknown user clock bias, residual phase and frequency errors from the tracking loops, and other sources of ranging errors including mismodeled signal propagation delays, ephemeris errors, multipath errors, and the intentional signal degradation imposed on the SPS signal.

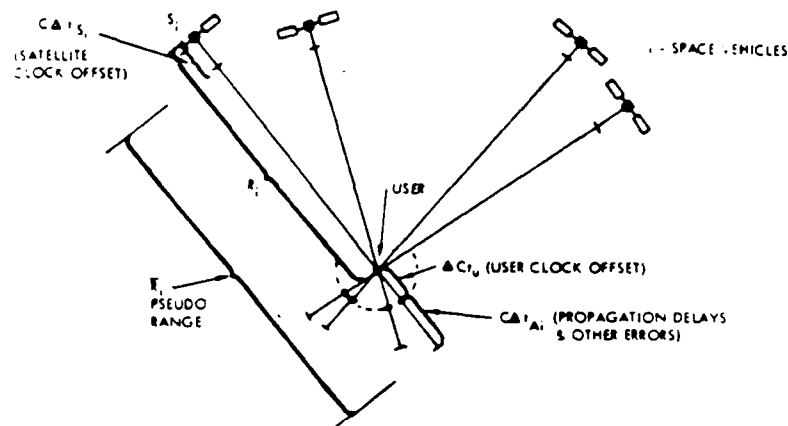


Figure 29. Illustration of Pseudorange Measurements [28]

The concept of finding a user position based on the removal of the fixed range bias from each range estimate is illustrated in a two-dimensional situation with three satellites in Figure 30. The figure illustrates that the pseudorange radii from the three satellites do not meet at a point but enclose the shaded triangular area. However, a range value of fixed magnitude can always be found that when removed from the pseudoranges will cause the radii to meet at a point which is the user position.²⁸

For maximum three-dimensional accuracy, the receiver needs to track well spaced satellites on the horizon and overhead. However, because the satellites are continuously rising and setting from the user's vantage point, geometry is often less than optimum for resolution of the vertical and horizontal position components. Error contributions from non-optimum geometry of the four tracked satellites is also referred to as GDOP, the factor that degrades ranging accuracy.

Differential GPS is a concept that eliminates some of the common, bias-type errors experienced by convention GPS. Differential GPS derives its potential from the fact that the measurement errors are highly correlated between different users. By employing a ground-based GPS receiver with known position location, correlated errors can be identified and eliminated. In addition, depending on the relative rates, intentional degradation of the GPS signal may be eliminated by differential GPS as well. These errors identified by the stationary system are then broadcast so that they can be removed by nearby users.

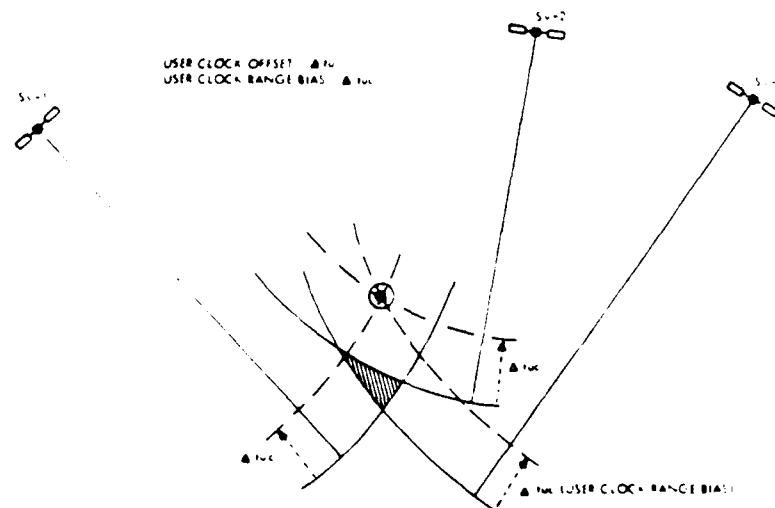


Figure 30. Determination of User Position and Time Offset [28]

Simulation and Flight Test Results

Reference 33 reports the results of 35 visual approaches made to five East Coast airports to see if a GPS single-channel receiver (referred to as a Z-set) was adequate to provide navigation for non-precision approaches. Either three satellites plus barometric altitude or four satellites were used to navigate, and the GPS error was computed. The error analysis of these tests showed rms errors on non-precision approaches to be 30.5 m or less in along-track and cross-track, which yielded a 95% probability circle with radius of 74.7 m. The GDOP for these tests was typically less than 8.5, and the bias error were less than 15 m. The receiver successfully maintained satellite lock during turns when the RF propagation link between the GPS antenna and a satellite was briefly masked. In addition, the Z-set appeared to navigate accurately in the presence of high RFI/noise emissions. It was concluded that the Z-set would meet FAA accuracy requirements for non-precision approaches (100 m, 2 drms accuracy in the horizontal plane) under appropriate satellite conditions.

Reference 34 describes the design and flight test results of an experimental low cost GPS receiver in a general aviation aircraft. The receiver was flight tested at a large urban airport, at several small general aviation airports, and over mountainous terrain. The horizontal system accuracy during typical aircraft flight profiles was measured to be 333 ft

(95% confidence). This level of accuracy meets the FAA accuracy requirements of AC90-45A for level and turning flight, and it is consistent with the proposed 100 m accuracy requirement of the Federal Radionavigation Plan.

Reference 32 describes a flight test of a Z-set where the objective was to demonstrate the possible improvement using the differential concept. This was a particularly meaningful test in that it contained a great deal of flight data which could be used for modeling the GPS errors. Figure 31 depicts the error characteristics of the four pseudo-range measurements from four different satellites. Figure 32 shows what GPS corrections look like in three dimensions after processing ground derived measurements. Figure 33 compares the horizontal position errors with conventional GPS and differential GPS. Figure 34 makes this comparison in the vertical direction. Figure 35 presents the total navigation error comparison for both conventional and differential GPS. Here, we see that with differential GPS, the total error remains less than 20 m, while the conventional GPS error grows up to 60 m. Note in Figure 35, that the GPS error has an oscillatory characteristic with amplitude of about 5 m and a period of about 15 sec. This oscillation appears on top of a time-varying bias type error. These curves can be used for developing simulation error models.

Reference 29 presents a comprehensive report of a fast time computer simulation developed to analyze various scenarios of GPS-referenced civil helicopter navigation. The simulation provides the ability to study the flight profile, the receiver Kalman filter, and the signal propagation environment. Elements of this simulation include:

1. Satellite constellation and almanac;
2. User route plan and flight dynamics;
3. Receiver Kalman filter parameters and differential implementation;
4. System ephemeris and clock error characteristics; and
5. Signal propagation environment characteristics.

Error sources include:

1. Satellite ephemeris error;
2. Satellite clock error;
3. Selective availability;
4. Ionospheric propagation delay;
5. Tropospheric propagation delay;
6. Multipath;
7. Receiver noise; and
8. User clock error.

Depending on the accuracy of the error models, this simulation could also serve as a source of error models for cockpit simulator studies using the GPS.

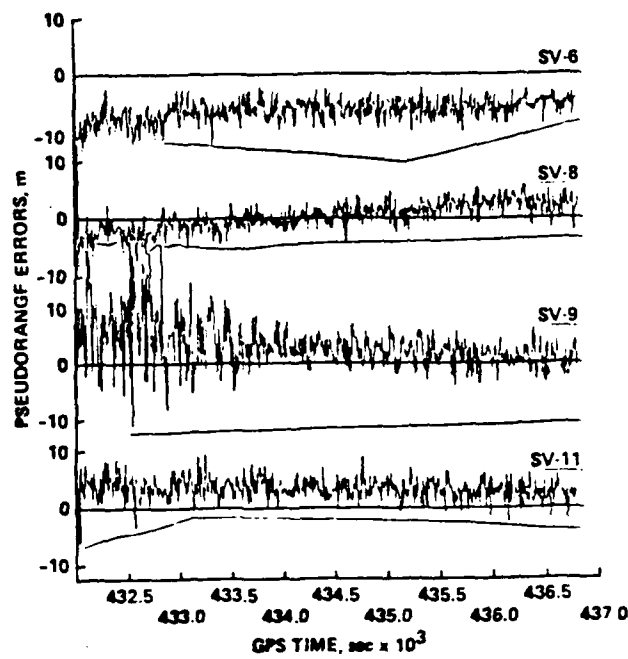


Figure 31. Reference Receiver Pseudorange Measurements During Test [32]

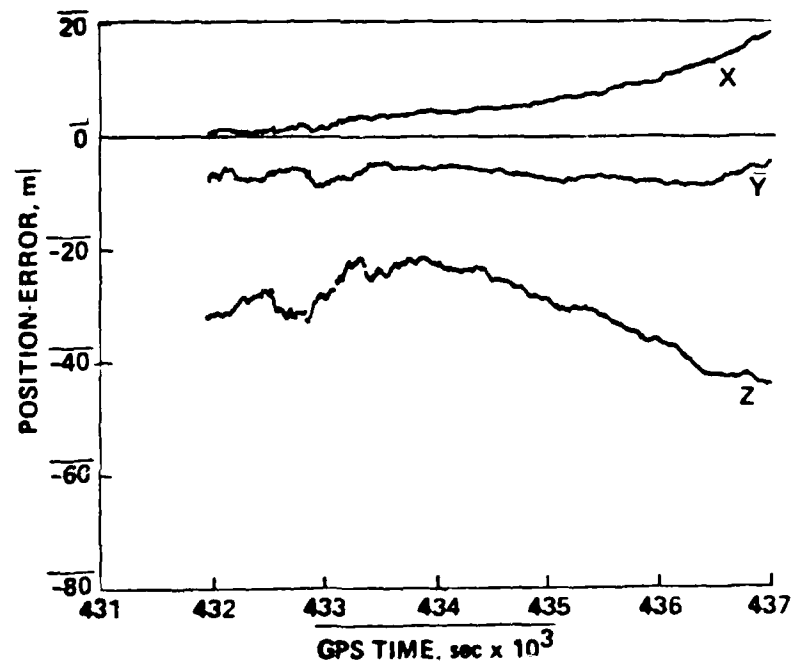


Figure 32. Differential GPS Corrections [32]

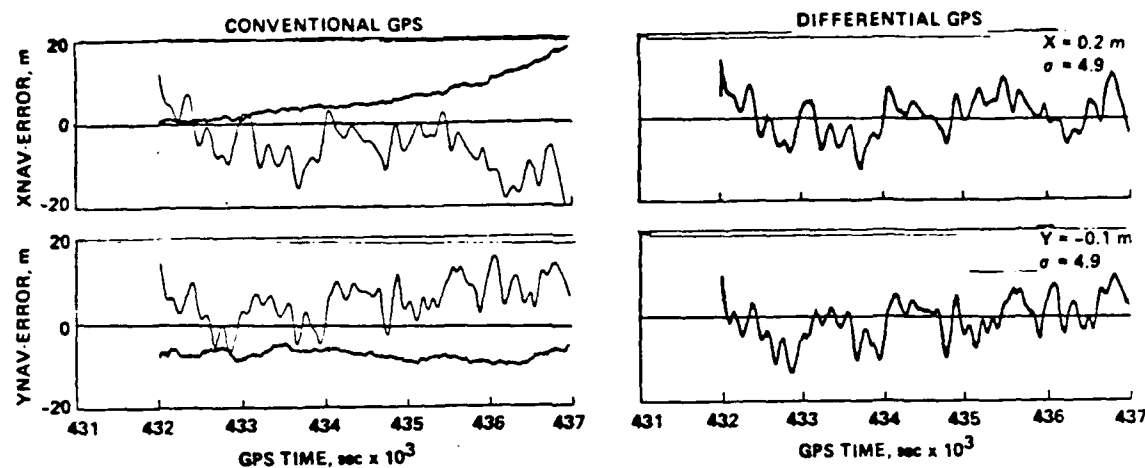


Figure 33. GPS Lateral Navigation Errors [32]

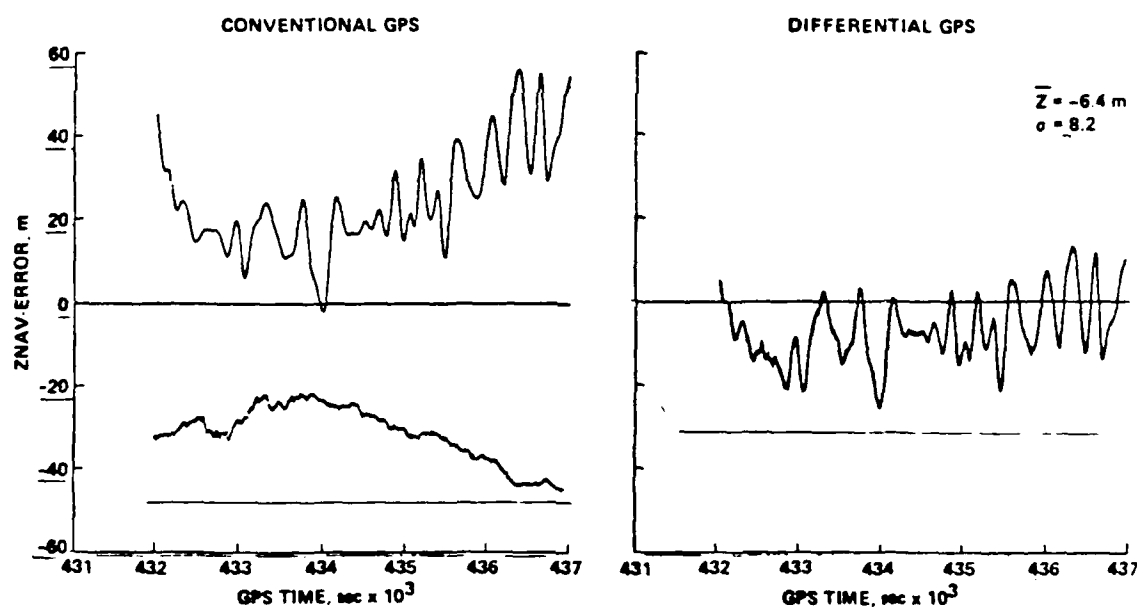


Figure 34. GPS Vertical Navigation Errors [32]

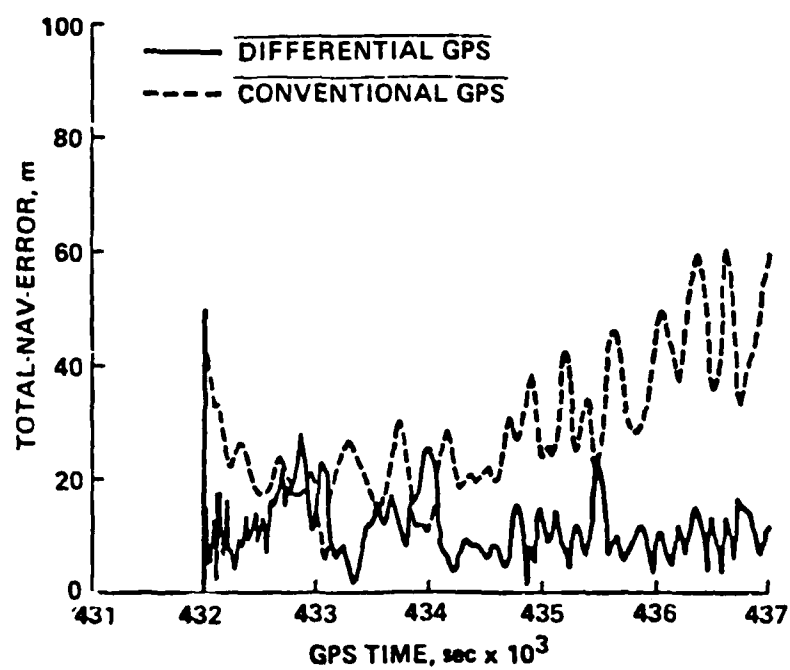


Figure 35. Total Navigation Error Comparison [32]

APPENDIX B

MODELS FOR ENVIRONMENTAL DISTURBANCES

It is well known that environmental disturbances in the form of steady winds, wind-shear, gust and random turbulence can have a major negative impact on task performance, pilot workload and, hence, pilot opinion ratings. Therefore, realistic simulation modules for the environmental disturbances must be developed (if not available already) and used in any meaningful simulator-based approach to TERPS operational enhancement. Towards this end, extant models for environmental disturbances need to be reviewed for fidelity of implementation with respect to the known real-world atmospheric turbulence characteristics.

Both objective as well as subjective fidelity of implementation must be evaluated. Objective model fidelity measures the degree to which a specific model for atmospheric disturbances mimics the temporal, spectral and statistical characteristics of the naturally occurring environmental disturbances acting upon the aircraft. In contrast, subjective fidelity refers to the qualitative sense of realism, with regard to the vehicle response to the simulated disturbances, that is experienced by the pilot in the flight simulator cockpit.

However, it must be emphasized that achieving objective model fidelity does not guarantee subjective fidelity and, therefore, pilot acceptance, and vice-versa. This is because subjective fidelity as measured by the pilot's subjective opinion rating, reflects not only the degree of realism of the atmospheric disturbance model itself, but also on the fidelity of other key modules (in particular, the helicopter model and the vehicle motion-cue simulation) in the overall closed-loop simulation. Under ideal conditions, the best approach would be to: (1) develop and validate models for each individual module in the overall closed-loop simulation using objective measures of model fidelity, and (2) verify the subjective fidelity of the complete closed-loop simulation using standard pilot opinion rating methods.

Unfortunately, this ideal approach is based upon the presumption that adequate data, simulation technology, time and money are available for conducting such an effort. In most cases, the stumbling block seems to be the lack of sufficient and accurate real-world data to serve as the basis for validating the objective fidelity of a given module. Furthermore, even if exact models or representations of the atmospheric disturbances were available, their "real-time" implementation (i.e., with frame or cycle times small enough to prevent aliasing) for piloted simulation investigations may not be feasible with the existing state-of-the-art in computer technology. This problem is especially exacerbated by the fact that a complex model for one module (e.g., turbulence) in a large closed-loop simulation usually mandates that the other modules (e.g., helicopter dynamics, motion-cueing drive systems) match its scope and level of implementation. As a result, a com-

promise is needed between physical realism and engineering requirements in selecting a model formulation for real-time simulation.

Before proceeding with the discussion of the engineering requirements on the wind models and their specific implementation algorithms, it is first appropriate to review the known physical properties of naturally-occurring atmospheric disturbances.

Characteristics of Naturally-Occurring Atmospheric Disturbances

It must be noted that the disturbances encountered by an aircraft depend upon the prevailing weather conditions and upon the altitude and speed with which the aircraft is flying. However, for convenience, atmospheric disturbances can be characterized into four types as mentioned earlier: (1) steady winds, (2) wind-shears, (3) discrete gusts, and (4) random turbulences. At any given time, the actual disturbance experienced by an aircraft can be described as a combination of one or more of these different types of disturbance categories. The mathematical model used to generate simulated atmospheric disturbances should attempt to represent the known statistical properties of actual disturbances. The following paragraphs describe what is known about the temporal, spectral, and probability distribution characteristics of real atmospheric disturbances. Much of the information described herein is based upon wind measurements gathered using instrumented towers and, to a lesser extent, from processing flight test data.

Temporal Characteristics.

Recorded time histories of atmospheric turbulence over long durations sometimes show some interesting features known as "patchiness" and "intermittency." Patchiness is a term used to describe the low frequency variation or modulation of the disturbance velocity amplitude over time that results in the occurrence of patches of large gust disturbances to the aircraft. The pilot must respond to these disturbances by applying the appropriate controls in order to avoid large flight path excursions from the desired path (i.e., altitude and course). Similarly, intermittency refers to the occurrence of condensed periods of activity where the rate of change (or gradient) of the measured turbulence velocity displays larger than normal values. Note that intermittency should not be confused with patchiness. Patchiness is a relatively low frequency amplitude modulation phenomenon reflecting the alternating periods of high and low turbulence field activity that is so familiar in other naturally occurring disturbances (e.g., lulls and swells in ocean waves). In contrast, intermittency is caused by a frequency or phase modulation of the disturbance function, whereby rapid changes in the rate of change (i.e., derivative) of turbulence velocity can occur independent of the amplitude of the turbulence velocity itself.

Power Spectral Density

Time histories of recorded atmospheric disturbance provide the raw data necessary for understanding their statistical properties in the time and frequency domains. All such analyses are based upon the use of the "frozen-field" concept. This assumption, also known as Taylor's hypothesis, states that the spatial pattern of wind turbulence velocities remains frozen in space (that is, moves through space at the mean wind speed) over a sufficiently large region of the atmosphere.

For purposes of analysis and physical interpretation, the random component of atmospheric disturbances called turbulence is considered to be a continuous stochastic process with certain definable statistical properties. According to this assumption, the frozen random turbulence field traveling through space with some mean wind speed can be envisioned as being composed of the sum of an infinitely large number of sinusoids (i.e., Fourier series representation) with their individual spatial frequencies (i.e., cycles per meter) and corresponding amplitudes. The Power Spectral Density function (or simply the spectrum) is based on a continuous version of this concept and describes in a concise functional form the distribution in spatial frequency of the power ((meters per second²) /cycle/meter) contained in the measured turbulence velocity signal.

In order to extract turbulence velocity spectral data from flight tests, it is assumed that the aircraft in penetrating the gust velocity field is perturbed by three independent, stationary stochastic processes, acting at the vehicle center of gravity. These three orthogonal turbulence velocity components are (1) the longitudinal disturbance u_g , (2) lateral disturbance v_g , and (3) the vertical disturbance w_g , all in the aircraft body axes. This single-point lumped representation is valid as long as the dimensions of the aircraft are much smaller than the smallest wavelength present in the turbulence spectra. Measured power spectral densities for u_g , v_g , and w_g show a remarkable degree of consistency and agreement with theory. The measured spectra can be concisely described by fitting the data with analytical functions of frequency with as few parameters as possible (i.e., parsimonious parameterization).

Two model formulations for describing the measured spectra are commonly used; they are the von Karman model and the Dryden model. The weight of the evidence indicates that the von Karman form, using a non-rational frequency representation, provides a more accurate fit to the experimental data over the entire frequency range. The Dryden form is constrained to a simpler rational representation, but is not as accurate in fitting the data at higher frequencies.

Table 12 gives two analytical spectral models. These models are of the form presented in the proposed revision of MIL-H-8501A by ARVIN/CALSPAN.³⁵ Notice that these two models each specify a family of power spectral densities for each gust component which depend upon only two parameters, the turbulence

Table 12. Poer Spectral Density Models
(From Proposed Revisions to MIL-H-8501A Reference 35)

Spectrum	von Karman		Dryden	
$\phi_u(\Omega)$	$\sigma_u^2 \frac{2L_u}{\pi} \frac{1}{[1+(1.339L_u\Omega)^2]^{5/6}}$		$\sigma_u^2 \frac{2L_u}{\pi} \frac{1}{[1+(L_u\Omega)^2]}$	
$\phi_v(\Omega)$	$\sigma_v^2 \frac{2L_v}{\pi} \frac{1+(8/3)(2.678L_v\Omega)^2}{[1+(2.678L_v\Omega)^2]^{11/6}}$		$\sigma_v^2 \frac{2L_v}{\pi} \frac{[1+12(L_v\Omega)^2]}{[1+4(L_v\Omega)^2]^2}$	
$\phi_w(\Omega)$	$\sigma_w^2 \frac{2L_w}{\pi} \frac{1+(8/3)(2.678L_w\Omega)^2}{[1+(2.678L_w\Omega)^2]^{11/6}}$		$\sigma_w^2 \frac{2L_w}{\pi} \frac{[1+12(L_w\Omega)^2]}{[1+4(L_w\Omega)^2]^2}$	
Scale Lengths	$h \geq 2500$ ft	$h < 2500$ ft	$h \geq 1750$ ft	$h < 1750$ ft
	$L_u = 2L_v = 2L_w$ = 2500 ft	$L_u = 2L_v = 184 h^{1/3}$ ft $2L_w = h$ ft	$L_u = 2L_v = 2L_w$ = 1750 ft	$L_u = 2L_v = 145h^{1/3}$ ft $2L_w = h$ ft
Standard Deviations σ_u & σ_v	Operational $\sigma_u = \sigma_v = 6$ ft/s	Operational $\sigma_u = \sigma_v = 6$ ft/s	Operational $\sigma_u = \sigma_v = 6$ ft/s	Operational $\sigma_u = \sigma_v = 6$ ft/s
	Most Severe $\sigma_u = \sigma_v = 20$ ft/s	Most Severe $\sigma_u = \sigma_v = 10$ ft/s	Most Severe $\sigma_u = \sigma_v = 20$ ft/s	Most Severe $\sigma_u = \sigma_v = 10$ ft/s
σ_w	$\frac{\sigma_u^2}{L_u^{2/3}} = \frac{\sigma_v^2}{(2L_v)^{2/3}} = \frac{\sigma_w^2}{(2L_w)^{2/3}}$	$\sigma_w = \frac{h^{2/9}}{3\sqrt{184}} \sigma_u$	$\frac{\sigma_u^2}{L_u} = \frac{\sigma_v^2}{2L_v} = \frac{\sigma_w^2}{2L_w}$	$\sigma_w = \frac{h^{1/3}}{\sqrt{145}} \sigma_u$

velocity standard deviation () and the gust scale length (L). The scale lengths L_u , L_v and L_w , as well as the turbulence velocity standard deviations σ_u , σ_v , and σ_w are deterministic functions of altitude as shown in Table 12.

The spectral densities given in Table 12 are functions of the spatial frequency variable (Ω) in cycles/ft. Conversion of these spectra from the spatial to the temporal frequency domain is accomplished by invoking the frozen field concept which implies that the temporal frequency ω (rad/s) is related to the spatial frequency Ω (cycles/ft) by the airspeed V (ft/s) according to the relationship $\omega = \Omega V$. Spectral densities given in the spatial frequency domain can therefore be transformed to the temporal domain via the transformation

$$\phi(\omega) = \frac{1}{V} \phi(\Omega) \Big|_{\Omega = \omega/V}$$

As mentioned above, the analytical spectral models and their parameter values given in Table 12 are taken from reference 35, which describes ARVIN/CALSPAN'S recommendations for updating MIL-H-8501A in terms of mission-oriented flying qualities requirements for military rotorcraft. It must be recognized that MIL-H-8501A provides no guidance or recommendations for wind models to be used for rotorcraft simulations. Consequently, this revision to MIL-H-8501A is based upon material presented in other similar documents for airplane flying qualities under Category III C flight operations (i.e., in particular, for terminal flight phases performed below 2000 feet altitude and requiring accurate flight path control). As a result, the exact definitions of the von Karman and Dryden spectra (i.e., analytical formulations, equations relating scale length and the standard deviations, and their functional dependence on altitude) given in Table 12 do not match those given in the previous flying qualities documents.³⁶⁻³⁹ However, it appears that these definitions proposed by CALSPAN are correct and consistent with each other.

It must be strongly emphasized that the existing models for turbulence spectra, especially for altitudes below 2,000 feet AGL are based on sparse experimental data, and as such, do not represent the final words on the subject of low altitude wind spectra. At best, these spectral models are to be used as guidelines for simulation purposes and should be modified as appropriate before implementation in any specific investigation.

Probability Distribution Characteristics

The probability distribution characteristics of atmospheric disturbances describe the relative frequency or probability of occurrence of the range of disturbance amplitudes. For continuous stochastic processes, these properties can be quantified in terms of their cumulative probability distributions and the probability density functions, or more simply by their N^{th} normalized central moments (i.e., mean, variance, skewness, kurtosis, etc.). As discussed earlier, some sample time histories of turbulence velocities show interesting features called patchiness and intermittency. An analysis of the probability distribution characteristics of the measured turbulence velocity and its derivative shows a distinctly non-Gaussian behavior as measured by their probability density functions and more succinctly by their measured fourth and sixth normalized central moments M_4 and M_6 , respectively. A Gaussian random process has values for M_4 (Kurtosis) and M_6 of 3.0 and 15.0, respectively. Measured values for these two parameters^{40, 41} are larger for both the turbulence velocity as well as the increments (i.e., derivative) of turbulence velocity. These data have been used by researchers to develop a non-Gaussian model for turbulence that not only has the desired measured von Karman or Dryden spectral density, but also is capable of reproducing the observed temporal characteristics of patchiness and intermittency described earlier.

However, the issue of wind simulation realism and the need to simulate the features of patchiness and intermittency may be exaggerated for the terminal approach segment (i.e., Category III C) simulation which covers approximately two minutes (12,000 ft at 100 ft/s) of real time; a period over which patchiness and intermittency may not occur frequently. In such cases, an alternative approach would be to impose deterministic or discrete gust segments in summation with a Gaussian turbulence time history to mimic the occurrence of patchy and/or intermittent disturbance features on some individual terminal approach segments.

Atmospheric Disturbance Models

The above paragraphs summarize the essential temporal, spectral and probability distribution features of naturally-occurring atmospheric disturbances. Any mathematical or computer disturbance model must be capable of generating sample time histories that can reproduce some or all of these observed characteristics as needed. The standard approach towards accomplishing this objective is to assume that all naturally-occurring atmospheric disturbances are formed by appropriately summing four types of elemental disturbance components: (1) mean winds, (2) wind shear, (3) discrete gusts, and (4) turbulence.

The following paragraphs describe the model structures currently used or proposed for the four wind components.

Mean Winds and Wind Shear Models

The mean or steady winds experienced by an aircraft along a reference flight path can vary considerably in both magnitude and direction. Data collected from various sources (including sophisticated Doppler radar) indicate that the wind velocity field can be represented by its three Cartesian components (W_x , W_y , W_z) in a ground-referenced coordinate system (x , y , z). Furthermore, this three-dimensional wind field data can also be stored over reasonable periods of time, thereby providing a four-dimensional (3 spatial coordinates plus the time dimension) wind field data base. Such a data base has been under development as part of the Joint Airport Weather Studies (JAWS) project⁴² by the National Center for Atmospheric Research (NCAR) in Boulder, Colorado.

Unfortunately, although this data base is essential for archival purposes, its enormous size and "table look-up" format precludes using it for real-time piloted simulation experiments, because of the large memory and computational burden imposed by the data storage/retrieval requirements. However, most aircraft simulation investigations are limited in scope to flying a selected but finite number of flight paths. Thus, for example, the simulated flight profiles for helicopter terminal instrument procedures shall also be limited to a fixed portion or volume of the airspace surrounding the helipad or runway (e.g., $\pm 45^\circ$ Az, $0-15^\circ$ elevation and 6 nmi range for

helicopter MLS approaches). Subsets of the JAWS wind fields data can be tailored for specific flight trajectories by storing data along three curved vertical planes; a central along-track plane through the flight path and two more planes (one on each side of the central plane) at a distance of ± 500 ft from the central plane. Linear interpolation between these three planar data sets may be used to compute the wind velocity at intermediate spatial coordinates.

It is recommended that, wherever feasible, such subsets of the JAWS data base be used in real-time piloted simulations. Sophisticated simulators such as the Vertical Motion Simulator (VMS) and the Man Vehicle Systems Research Facility (MVS RF) at NASA/Ames are capable of handling the computational burden imposed by such "Table Look-up" models. However, these simulators are not necessarily warranted for all aspects of TERPS operational enhancement. For less sophisticated simulators (e.g., chair 6 helicopter simulator at NASA/Ames) simple analytical wind shear models as described below are needed to fit the real-time computational requirements of the piloted simulation.

Two types of wind shear models have been proposed in the flying qualities literature. Both MIL-F-8785C³⁶ for military airplanes and CALSPAN's proposed revision to MIL-H-8501A³⁵ for military rotorcraft define wind shear models that describe the variation of the horizontal mean wind profile as a function of altitude above ground level (AGL), by the following equations:

MIL-F-8785C:

$$\begin{aligned} u_w &= u_{20} \frac{\ln(h/z_0)}{\ln(20/z_0)} & : 20 \text{ ft} \leq h \leq 600 \text{ ft} \\ u_w &= u_{20} & : h \leq 20 \text{ ft} \\ u_w &= u_{20} \frac{\ln(600/z_0)}{\ln(20/z_0)} & : h \geq 600 \text{ ft} \end{aligned}$$

where u_w = horizontal wind speed (ft/s)
 u_{20} = horizontal wind speed at 20 ft AGL (ft/s)
 z_0 = surface roughness height
 = 0.15 ft. for category C flight phase
 h = altitude AGL (ft)

Calspan's Revision to MIL-H-8501A:

$$V_w = V_0 + Gh \quad : 0 \leq h \leq 300 \text{ ft}$$

where V_w = horizontal wind speed (ft/s)
 V_0 = horizontal wind speed at 20 ft AGL (ft/s)
 h = altitude AGL (ft)
 G = 0.14 ft/s per ft: for operational environment
= 0.34 ft/s per ft: for severe environment

u_{20} in MIL-F-8785C and V_0 in Calspan's revision to MIL-H-8501A define the wind speed at 20 ft AGL; its value can be chosen to represent a prescribed probability of exceedance using data contained in Figure 36 (plot showing probability of exceeding mean wind speed at 20 ft AGL) of Reference 37. For flying qualities experiments, the mean wind speed at 20 ft AGL (i.e., u_{20} or V_0) is chosen to be 25 ft/s, 50 ft/s or 75 ft/s corresponding to "light," "moderate" or "severe" environmental conditions. The wind gradient values given for the MIL-H-8501A model are based upon wind shear estimates extracted from measured data. Wind direction, in both models, can be specified as a constant or a function of altitude.

An alternate formulation in the proposed new Military Standard and Handbook for Flying Qualities of Air Vehicles³⁸, defines wind shear as a constant time rate of change of wind speed and direction as follows:

$$\text{For } t \leq t_0: u_g = V_0 \cos\psi_0, v_g = V_0 \sin\psi_0$$

$$t \geq t_f: u_g = V_0 \cos\psi_f, v_g = V_0 \sin\psi_f$$

and for the duration of the shear

$$t_0 < t < t_f: u_g = V_0 \cos\psi_0 + \frac{t - t_0}{t_f - t_0} (V_f \cos\psi_f - V_0 \cos\psi_0)$$

and

$$\text{and } v_g = V_0 \sin\psi_0 + \frac{t - t_0}{t_f - t_0} (V_f \sin\psi_f - V_0 \sin\psi_0)$$

where

V_0 = Initial wind velocity;
 ψ_0 = Initial wind angle;
 V_f = Final wind velocity;
 ψ_f = Final wind angle;
 t_0 = Time shear is initiated;
 t_f = Time shear is terminated; and
 $t_f - t_0$ = shear duration (e.g., 10 seconds)

Maximum wind shear magnitude gradient is

$$\frac{V_f - V_o}{t_f - t_o} < 3.4 \text{ ft/s}^2,$$

and maximum wind shear orientation gradient is

$$\frac{\psi_f - \psi_o}{t_f - t_o} < 9 \text{ deg/s.}$$

The shear must terminate at 50 ft AGL for landing simulation.

The wind shear simulation module at NASA/Ames, called BWIND, uses a model formulation similar to that proposed in MIL-H-8501A above, but where the wind shear is active for altitudes between 20 ft and 200 ft, AGL.

None of the above analytical wind shear models is satisfactory for helicopter approach and landing simulations needed for TERPS operational enhancement. The first type of model where wind speed is a function of altitude has an acceptable analytical formulation but is limited to altitudes less than 300-600 ft AGL. The second model structure is not acceptable because the wind speed variation is defined as a function of time. In such a model, the wind shear magnitude and orientation gradient must be tuned to the vehicle speed during landing. In a piloted helicopter simulation, the pilot may choose to fly at a speed that is different and varying with altitude from that assumed in the wind shear time gradients, thus leading to meaningless simulation results. Furthermore, a time rate of change wind shear model would be totally incorrect for the helicopter deceleration to a hover task scenario.

What is needed, therefore, is an analytical model for wind shear as a function of altitude AGL that is tailored to fit a representative finite set of low altitude (i.e., ≤ 3000 ft AGL) wind velocity profiles in the JAWS data base. Such a model would provide realistic wind shear disturbances to the aircraft while maintaining the element of surprise or uncertainty during individual approach segments. A computational model for generating three-dimensional wind shears experienced by aircraft during severe convective atmospheric conditions has been developed by Bray⁴³ for flight simulator applications. A slightly modified version of the Bray model has been implemented on the NASA/Ames MVSF 727-200 simulator. This wind-field program consists of five wind-field data sets chosen to represent critical wind shear environments actually encountered by aircraft in previous accidents or hazardous take-off or landing situations. Since these data sets are for transport airplane flight profiles during take-off or landing, they cannot be used as such for helicopter applications. However, similar data sets can be generated from existing wind-field data bases that are specifically tailored to the types of helicopter flight profiles (e.g., 3° , 6° , 9° and 12° glide-

slope curved and descending approaches to a hover over a helipad) likely to be flown during ground-based simulations for TERPS enhancement.

Discrete Gust Models

The term "discrete gust" is used to denote a discrete or sudden change in the wind velocity.³⁷ In simulation, discrete gust components can be used independently or in conjunction with other wind components (i.e., mean winds and turbulence) to generate any desired temporal features (e.g., patchiness and intermittency) or wind shear spatial characteristics encountered during thermal inversions and thunderstorm conditions.

Two types of discrete gust models are presented in the flying qualities literature. The standard discrete gust model described in all the military specifications documents may be used for any of the three gust velocity components, and by derivation, any of the three angular components. It has a "one-minus-cosine" shape given by

$$\begin{aligned} v &= 0 & : x < 0 \\ v &= \frac{v_m}{2} \left(1 - \cos \frac{\pi x}{d_m} \right) & : 0 \leq x \leq d_m \\ v &= v_m & : x > d_m \end{aligned}$$

The second type, called a ramp gust model is an approximation to the "one-minus-cosine" discrete gust velocity model and is given by the equation:

$$\begin{aligned} v &= 0 & : x < 0 \\ v &= \frac{v_m}{d_m} x & : 0 \leq x \leq d_m \\ v &= v_m & : x > d_m \end{aligned}$$

Sudden large gust disturbances including specific wind shear profiles can be generated on a computer by combining single discrete gust inputs (either the "one-minus-cosine" or ramp forms) applied in sequence at a finite number of points in time. Furthermore, as discussed later in this section, a stream of elemental discrete ramp gust components with a prescribed amplitude (v_m) distribution can be used to generate turbulence velocity time histories that display the intermittency feature described earlier.⁴⁴

Turbulence Models

The basic approach toward generating simulated turbulence time histories should be to choose a representation that best describes the known temporal, spectral and probability distribution characteristics observed in or extracted from real-world meteorological or flight test data. One obvious approach is to use recorded time histories of turbulence velocity obtained through processing data from flight tests under controlled experimental conditions. Specifically, test data must be obtained where: (a) the vehicle's flight path and airspeed are chosen to match the flight conditions to be simulated, and (b) the three wind speed components can be extracted by processing (e.g., using a Kalman filter/smoothing) the airspeed measurements provided by the airborne system and the ground speed estimates derived from the ground-based tracking radar data. This approach provides accurate time histories of turbulence velocity as long as the simulated flight path and airspeed profiles are identical to the flight test profiles from which these data were obtained.

However, simulations are usually conducted before, instead of after, an actual flight test program. That is, in fact, the motivation behind this study, the objective of which is to determine the merits and feasibility of using simulators instead of actual flight tests for non-standard operational TERPS evaluation. For such situations, it is essential to have some analytical method for computer generation of realistic turbulence velocity time histories.

Unfortunately, as is usually the case, the situation is not as clear-cut as it appears. Any ground-based flight simulation is only as good as the fidelity of the individual modules (i.e., vehicle dynamics, atmospheric disturbance models, navigation/guidance signal models and visual/motion simulation) that comprise it. Therefore, before one can substitute a simulator for flight tests, it is mandatory to first make sure that the simulator facility itself provides a faithful replica of the real-world flight test scenario. Validation of a simulator facility is an interactive process and involves several iterations between flight test data and simulator predictions. Therefore, before one can use confidently a simulator-based approach for developing helicopter TERPS criteria for non-standard situations (i.e., non-standard navigation aids, approach profiles, landing sites and display/control augmentation) it is necessary to verify that the simulator-based results match actually-recorded pilot performance and workload data from earlier flight tests (e.g., data from NASA/FAA flight test program for evaluating straight-in^{1, 2} and curved descending approaches.^{3 - 5}

Hence, one task in this effort is to prepare recommendations for candidate simulator-based TERPS evaluation of standard ILS/MLS straight-in approaches (3° G/S for ILS and 6°, 9°, 12° G/S for MLS) on fixed-base NASA/ARC simulators. The purpose of this simulation test plan is to duplicate the scenario flown in an earlier NASA/FAA flight test program to determine the operational limitations of flying straight-in MLS approaches using "raw data" or "angle only" information.^{1, 2} It would be desirable in such a simulation

to mimic or duplicate as fully as possible the flight test conditions encountered by the pilot in the actual flight tests. This would mean, that actual flight test data be used to extract the wind field (ie., mean winds/wind shear and turbulence time histories), the MLS navigation error time histories and any other pertinent flight information that is relevant for improving the fidelity of the piloted fixed-base simulation.

Thus, using recorded turbulence velocity time histories can be a definite advantage in the verification/validation of a simulator facility. Since a piloted simulation consists of an integration of several individual modules, it is difficult, if not impossible, to identify which of the modules is incorrect from closed-loop results. By using actual data for as many modules as possible, the problem of validating the remainder of the simulation modules becomes easier. In subsequent experiments, the modules for which actual data is used can be replaced one at a time with computer model-based time histories to complete the simulator validation process.

In summary, using the recorded time history turbulence model does have advantages for purposes of simulator validation using flight test data. However, analytical models must be used in any operational simulator-based effort for evaluating helicopter terminal instrument procedures for non-standard situations. The following paragraphs discuss the merits of the different analytical models for turbulence presented in the literature.

Two types of analytical or computer models of atmospheric turbulence have been used in previous simulation efforts. They are: (1) the Gaussian models, and (2) the non-Gaussian models.

Gaussian Models The Gaussian models, as the name implies, assume that each of the three components of turbulence u_g , v_g and w_g , has Gaussian probability distribution characteristics, and a power spectral density that can be described by a Dryden or von Karman spectrum in the temporal frequency domain ω

$$\phi(\omega) = \frac{1}{V} \phi(\Omega) \Big|_{\Omega = \omega/V}$$

where $\phi(\Omega)$ are shown in Table 12.

Two methods can be used to implement a Dryden or von Karman Gaussian model on a computer. They are (a) a sum-of-sinusoids representation, and (b) a Gaussian white noise through a linear filter representation.

In the sum of sinusoids representation, each of the turbulence components is modeled as

$$\eta(t) = \sum_{i=1}^N \eta_i \cos(\omega_i t + \phi_i)$$

- η = u_g , v_g or w_g
 N = number of sinusoids
 η_i = amplitude of the i^{th} frequency component (ft/s)
 ω_i = frequency of the i^{th} frequency component (rad/s)
 ϕ_i = phase of the i^{th} frequency component (rad) obtained from a uniform distribution over the interval $[0 - 2\pi]$ radians.

The N frequencies ω_i are equispaced $\delta\omega$ apart over the temporal frequency range of interest $[\omega_{\min}, \omega_{\max}]$ defined for the turbulence power spectrum $\phi_\eta(\omega)$. The corresponding N amplitudes η_i are chosen such that the power of the sinusoid at ω_i approximates the area under the power spectrum $\phi_\eta(\omega)$ over the frequency bin $[\omega_i - \frac{\delta\omega}{2}, \omega_i + \frac{\delta\omega}{2}]$. Thus,

$$\frac{\eta_i^2}{2} = \phi_\eta(\omega_i) \delta\omega$$

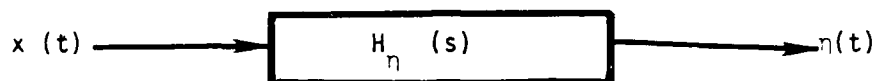
The number of frequency components N chosen should be large enough to result in a Gaussian probability density function for the computer-generated turbulence time histories. In previous simulation investigations, the number of sinusoids N used to fit the spectrum has been too low (≤ 15) with the resulting time histories being too predictable from the pilot's viewpoint. This error was further compounded by the choice of arbitrary ϕ_i values (i.e., either 0 or π radians) used to generate the sample time histories instead of a random phase selection from a uniform distribution over the $[0-2\pi]$ radians interval. As many as 30 to 70 sinusoidal components may be needed depending upon the shape of the turbulence power spectrum (e.g., in reference 45, it is shown that at least 30 and preferable 70 components be used to generate realistic DD963 ship motion time histories over a 1200 s interval for the six deck motion degrees of freedom). By using different sets of values of (ϕ_i ; $i = 1 \sim N$), a large but finite number of samples of turbulence time histories can be generated for use in a simulation. As a result, pilots cannot learn to anticipate the disturbances and the element of surprise or uncertainty in the expected turbulence can be maintained. Furthermore, even though the turbulence time history is random-appearing to the pilot, the signal generated is deterministic with power concentrated only at the known N component frequencies ω_i . This fact makes it possible to compute more accurate input-output models for the aircraft-dynamics and the human pilot than would be possible with a truly random Gaussian turbulence model. In summary, the sum-of-sinusoids model for generating Gaussian turbulence if used properly, can be an extremely useful approach for piloted simulation

investigations, especially where post-experimental analysis of the data gathered is a major part of the study effort.

The Gaussian white noise through a linear filter representation is based upon the fact that any continuous Gaussian random process $\eta(t)$ with a rational power spectral density function of the form

$$\phi_{\eta}(\omega) = H_{\eta}(s) H_{\eta}(-s) \Big|_{s=j\omega} = \left| H_{\eta}(j\omega) \right|^2$$

can be generated as the output of a linear filter $H(s)$ driven by white noise $x(t)$ with unity spectral density $\phi_x(\omega) = 1$ as shown below.



The filter $H_{\eta}(s)$ must have more poles than zeros in order to be realizable. The Dryden power spectral density $\phi_{\eta}(\omega)$ ($\eta = u_g, v_g$ or w_g) is rational in form and hence an appropriate linear filter $H_{\eta}(s)$ can be determined (by spectral factorization of the Dryden spectral density) and used to generate the corresponding turbulence time history $\eta(t)$. In contrast, the von Karman power spectral density formulation is non-rational (as evidenced by the non-integer powers 5/6 and 11/6 in the denominator function); therefore it cannot be represented exactly in terms of a linear filter with a finite number of poles and zeros. In practice, however, any non-rational spectrum including the von Karman formulation can be approximated as closely as desired by a linear filter $H_{\eta}(s)$ with a sufficient number of poles and zeros in the transfer function. The resulting filter model is higher order and complex because of the large number of poles (i.e., order of the denominator polynomial of $H_{\eta}(s)$) required to fit the von Karman spectrum.

The continuous linear filter model for Gaussian turbulence must be discretized for implementation on a digital computer. The digital linear filter formulation can be derived using one of several approaches (e.g., Z-transform, Tustin transformation or transition matrix method). Among the two spectral models, the Dryden linear filter model is the most commonly used form for pilot-in-the-loop as well as non-real-time computer simulations. At NASA/Ames, a Dryden turbulence filter model is implemented for real-time simulations, in a subroutine called BWIND. The model parameters, however, would have to be adjusted to match the specific form of the Dryden spectra given earlier in Table 12.

The Gaussian models, because of the simplicity of their implementation have been used, almost exclusively, in most piloted simulation efforts. However, starting in the late Sixties and the early Seventies there has been considerable discussion and concern about the lack of realism in turbulence time histories generated with a Gaussian disturbance model.^{40,41,46-51} This assessment is based upon a detailed examination of actual recorded turbulence

considerable discussion and concern about the lack of realism in turbulence time histories generated with a Gaussian disturbance model.^{40,41,46-51} This assessment is based upon a detailed examination of actual recorded turbulence data which shows that the Gaussian assumption is not valid under most circumstances (see earlier discussion on temporal characteristics). This assumption that the lack of realism is related to the use of a Gaussian model structure has led flying qualities engineers to develop and investigate several forms of non-Gaussian turbulence models, as described in the following material.

Non-Gaussian Models Three types of non-Gaussian models have been proposed in the literature. They are:

1. The University of Washington (UW) model^{40,41}
2. The Royal Aircraft-Establishment (RAE) model⁴⁴
3. The Netherlands National Aerospace Laboratory (NLR) model⁵¹

The motivation behind the development of these non-Gaussian turbulence models has been to generate time histories that reveal the features of patchiness and intermittency observed in actual recorded data. These two characteristics can be attributed to the non-Gaussian probability density functions of the measured turbulence velocity, and its derivative, respectively. A useful measure of non-Gaussian distribution is the fourth order central moment or kurtosis. A Gaussian distribution has a kurtosis value of 3. If turbulence velocity has a Gaussian distribution, then the derivative of turbulence velocity (or turbulence increments) must also have a Gaussian distribution⁴¹ and both must have a kurtosis value of 3 each. Measured values of kurtosis as large as 6 have been found for actual turbulence velocities reflecting the observed patchiness in turbulence. Furthermore, analysis of actual data shows that the kurtosis of the velocity increment distribution is greater than the kurtosis of the velocity itself, indicating the strong presence of intermittency.

The UW model^{40,41} was developed to generate patchy turbulence velocity time histories that have a non-Gaussian distribution with values of kurtosis between 3 and 9 and a Dryden spectrum. A block diagram of the UW model is shown in Figure 36. The non-Gaussian representation for turbulence $g(t)$ is of the form

$$g(t) = a(t) \cdot b(t) \cdot \frac{R}{\sqrt{R^2+1}} + c(t) \frac{1}{\sqrt{R^2+1}}$$

where $a(t)$, $b(t)$, and $c(t)$ are Gaussian signals obtained by passing independent Gaussian white noise sources η_1 , η_2 , η_3 through linear filters with transfer functions $H_a(s)$, $H_b(s)$, and $H_c(s)$, respectively. These filters are chosen (i.e., structures and parameters) so that the signals $d(t)$, $c(t)$, and $g(t)$ have Dryden spectral densities. The parameter R has no impact on the

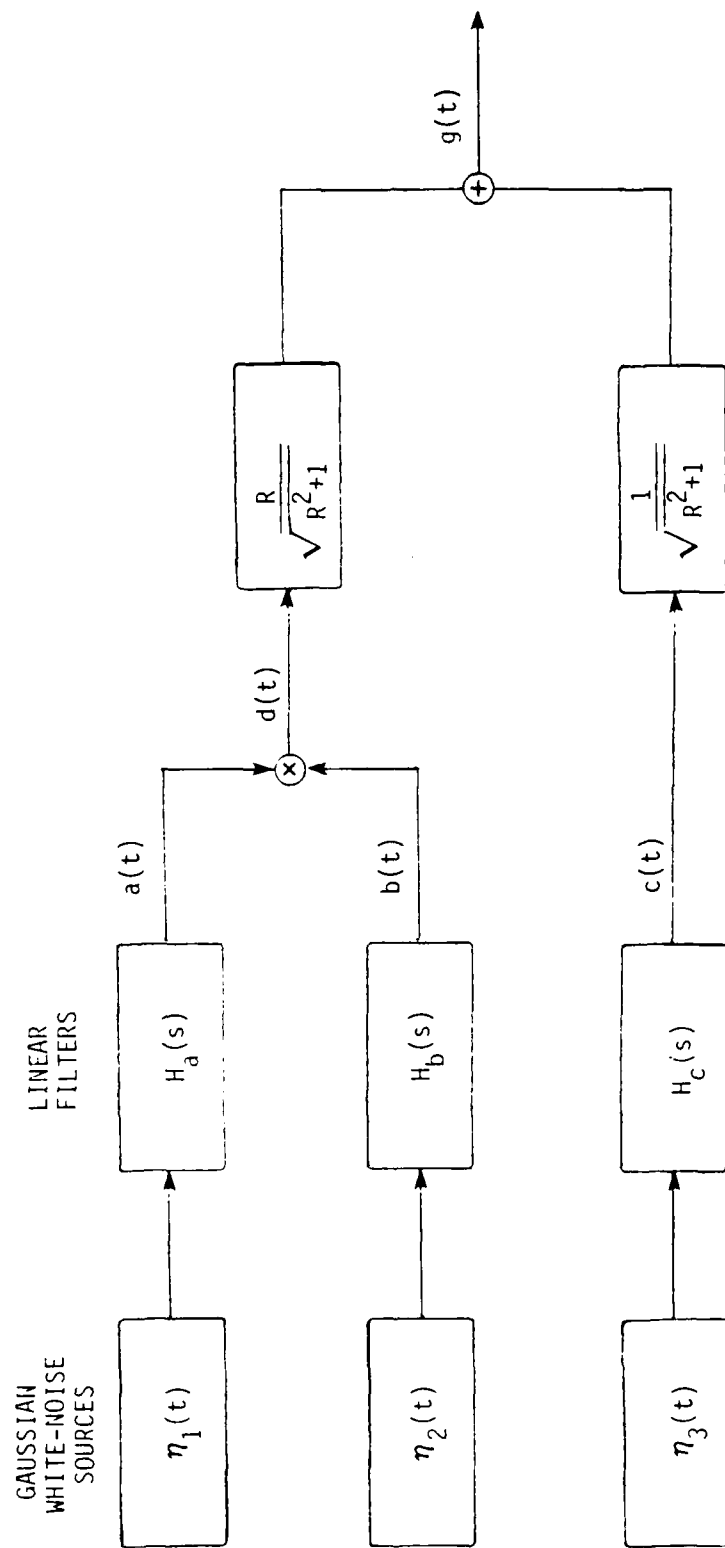


Figure 36. The University of Washington (UW) Model

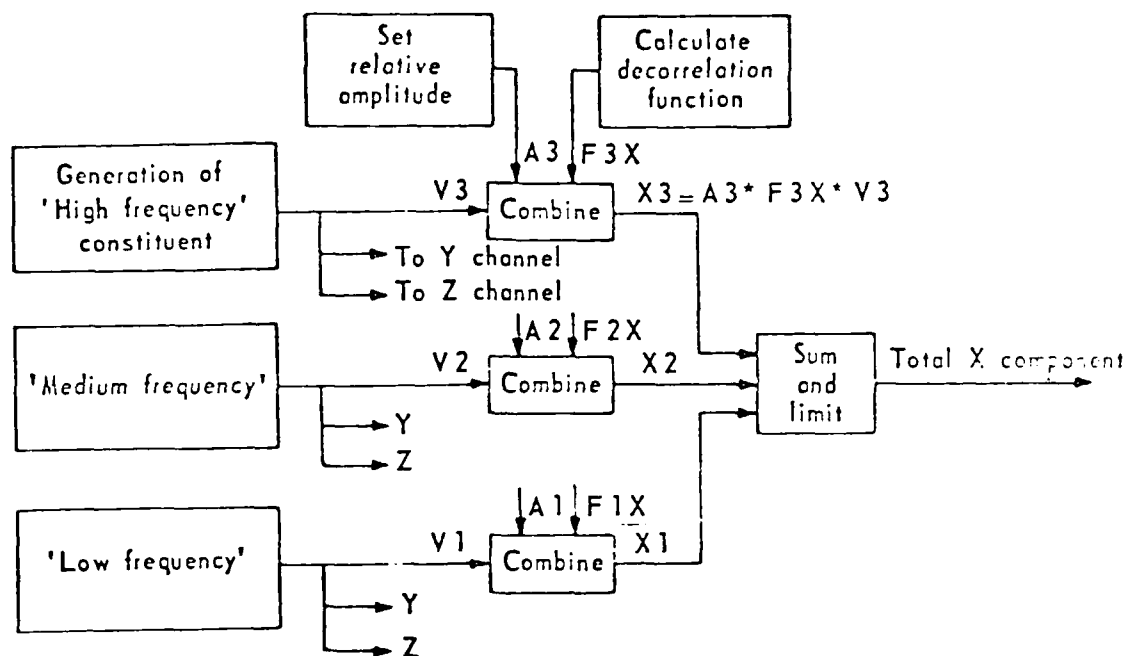


Figure 37. The Royal Aircraft Establishment (RAE) Model

spectral densities of the signals $c(t)$, $d(t)$ and $g(t)$. However, the parameter R can be used to control the probability distribution function of $g(t)$. A value of $R=0$ gives a purely Gaussian distribution for $g(t)$ and $R = \infty$ produces $g(t)$ with a so-called modified Bessel function of the second type and order zero. Thus for values of R between 0 and ∞ , a full range of non-Gaussian distributions for $g(t)$ can be generated. Reference 41 shows how each of the filters $H_a(s)$, $H_b(s)$ and $H_c(s)$ must be chosen to simulate the three components of Dryden turbulence u_g , v_g and w_g .

Patchiness in the turbulence velocity time history $g(t)$ is introduced by the process of modulating the random Gaussian function $a(t)$ by a "patch inducing" function $b(t)$. Work by van de Moesdijk⁴⁸ on this non-Gaussian model, suggests that the average length or duration of patchiness may be controlled by varying the ratio of the cut-off frequencies (i.e., bandwidths) or filter $H_a(s)$ and filter $H_b(s)$, without affecting the power spectral density or the probability distribution function of $g(t)$.

Although this model reproduces turbulence time histories with patchiness characteristics, it is not as successful in generating the appropriate intermittency behavior observed in actual data. Specifically, the UW non-Gaussian model does not properly model the velocity increment distribution of atmospheric turbulence. The UW model generates velocity increment kurtosis values that are consistently smaller than the corresponding velocity kurtosis magnitudes. This is contrary to measured data which show that the kurtosis values for turbulence velocity increments are consistently larger than those for the turbulence velocity itself. Therefore, the UW model is recommended only where accurate modeling of non-Gaussian turbulence velocity distribution is needed.

A block diagram of the RAE model as developed by Tomlinson is shown in Figure 37. The model was developed to generate turbulence velocity time histories that display the "intermittent" behavior observed in actual data. Documents describing the RAE model are not too easy to follow as far as the details are concerned. Therefore, the best way to summarize the model features is to paraphrase the description provided in the original reference 44, as follows: "Three independent time-sequences of velocity fluctuation (i.e., each sequence having a different characteristic gust gradient and thus containing power at different dominant frequencies, loosely termed 'high,' 'medium,' and 'low.'" Three sequences, as shown in Figure 38 were considered to provide sufficient coverage of the frequency range of interest to manual flight. Each sequence feeds all three aircraft axes (x, y, z). To remove the perfect correlation that exists at this stage, a decorrelation procedure is applied, involving random switching. Within each channel, the relative amplitudes A_1 , A_2 , A_3 of each constituent are adjusted to give a power spectrum curve with the desired slope at high frequencies (corresponding to the von Karman spectra), and the three constituents are summed to give the total component in one axis. A final, overall scale factor is applied externally to give a selected root-mean-square intensity.

On a proportion of occasions, controlled by the single parameter F , the distribution returns a zero gust and so provides the desired property of intermittency. An individual sequence $x_3(t)$ may then look like that shown in Figure 39. Note the intervals (e.g., after the first ramp gust) during which only zero gusts are occurring.

Although F is a parameter which defines the global intermittency, the relative proportion of non-zero gusts is also varied locally to each constituent. According to this model, F is the proportion of zero gusts generated by the defined distribution, so that $1-F$ is a proportion of non-zero gusts. To provide a relatively decreasing probability of non-zero gusts, in moving from the high frequency constituent to the low, $1-F$ is divided locally by 1 , $\sqrt{2}$ and 2 . This adjustment is necessary to insure that all gusts are part of the same family, and to compensate for the absence of a still higher frequency constituent.

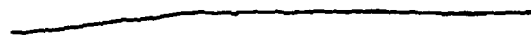


a. High Frequency Constituent

→ Time



b. Mid Frequency Constituent



c. Low Frequency Constituent

Figure 38. High, Medium and Low Frequency Constituents

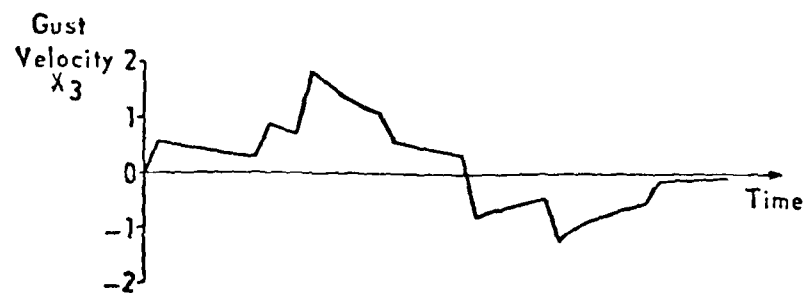


Figure 39. "High" Frequency Component X_3 , $F = 0.8$

The global intermittency parameter F is set such that $0 \leq F \leq 1$. For $F = 0$, the intermittency is minimal. When the value of F is increased (e.g., see Figure 39 for $F = 0.8$), remembering that F is roughly the fraction of zero gusts, intermittency is increased by virtue of the occurrence of relatively long intervals between individual gust constituents.

The RAE non-Gaussian model is based upon the use of discrete ramp gust components (as opposed to random Gaussian white noises) to generate the desired turbulence time histories. The model formulation is highly empirical and therefore subject to differences in interpretation during data analysis. Furthermore, the RAE model only describes the intermittency observed in actual turbulence data, and therefore should not be used where simulation of patchiness is an important consideration.

The NLR model for turbulence⁵¹ represents an attempt to remedy the major deficiencies of the UW and RAE models - namely, the inability to simulate intermittency in the UW model, and patchiness in the RAE model. A block diagram of the NLR turbulence model is shown in Figure 40. The proposed model structure is a hybrid combination of the UW (see Figure 36) and RAE (see Figure 37) model block diagrams. The UW model for patchy turbulence as given by

$$g(t) = a(t) \cdot b(t) \frac{R}{\sqrt{R^2+1}} + c(t) \cdot \frac{1}{\sqrt{R^2+1}},$$

is modified by noting that for relatively long average patch durations the filters $H_a(s)$ and $H_c(s)$ are almost identical, and hence $a(t)$ can be replaced by $c(t)$. Thus, with this substitution

$$g(t) = c(t) \frac{1 + R \cdot b(t)}{\sqrt{R^2+1}}.$$

However, $c(t)$ is still Gaussian and the resulting turbulence time history only patchy. Both intermittency and patchiness can be generated by replacing the Gaussian signal $c(t)$ with the intermittent signal $i(t)$ generated by the RAE model. Thus

$$g(t) = i(t) \cdot m(t)$$

$$\text{where } m(t) = \frac{1 + R \cdot b(t)}{\sqrt{R^2+1}}$$

The NLR model thus simulates turbulence velocity time histories that show evidence of both patchiness and intermittency. This model was evaluated by the NLR⁵¹ for an ILS approach and landing task on a four-degree-of-freedom moving base flight simulator. Results of this limited evaluation program

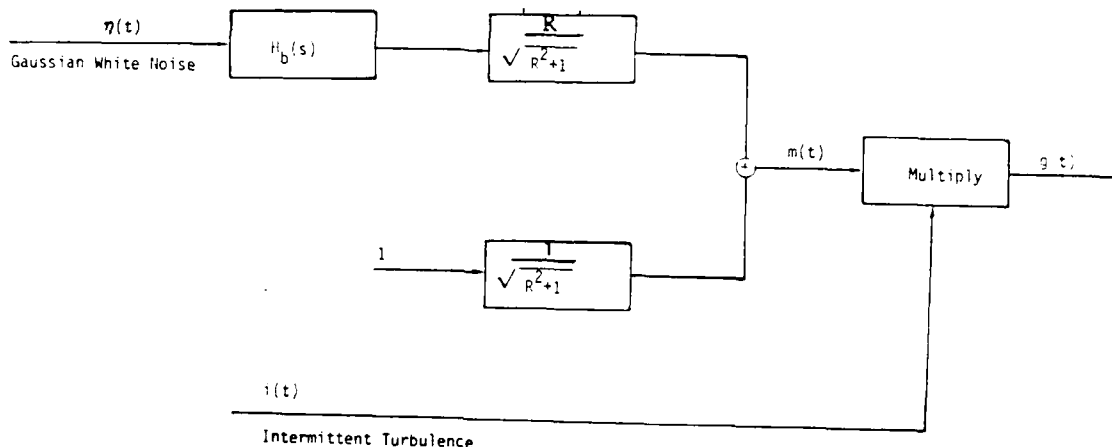


Figure 40. Block Diagram, Representing the Generation of Patchy and Intermittent Turbulence

indicate that "pilot opinion of the realism of turbulence improves from poor for the Gaussian model to fair for a model containing either patchiness or intermittency to good for a model with both characteristics." Further independent evaluation of this model, both analytical as well as simulation, should be conducted to determine its practical usefulness for helicopter applications.

Discussion of Disturbance Models

The models presented above represent only a small fraction of the proposed formulations for describing atmospheric disturbances. Furthermore, there is no universal agreement or consensus in the research community as to which model is best for use in piloted simulation investigations. In order to identify the reasons for this dilemma, it is first necessary to understand that the simulation of a helicopter flying through a turbulent atmosphere consists of three tasks. The first task is to establish an adequate data base of the atmospheric disturbances that this vehicle may encounter for the simulated mission/scenario. This is fundamentally a meteorological activity; however, existing data may not be suitable for the particular application (e.g., curved descending and decelerating approaches to a hover) which may cover a large

range of airspeeds and altitude. The second task is for the engineer to interpret the validity of the existing data, and, if acceptable, to use this data for developing analytical disturbance models. Errors can occur in the selection of a valid data base or in the analytical methods used in model development (or both) resulting in inappropriate or incorrect (or both) turbulence models. The third task is to define the type of helicopter model most appropriate to the investigation, and to determine how best to integrate the wind model with it. This is especially important for helicopters flying at speeds below 60 knots, including hover. At such low speeds, the assumption of instantaneous gust penetration may not hold and it may be necessary to allow for gradual penetration of the gust field. Under these circumstances, a finite-element individual blade rotor model must be used to accommodate for the variation of the wind velocity encountered by each blade. The fourth and final task is to select a motion drive system (i.e., washout filters, gains, maximum travel limitations, etc.) for the ground-based simulator that reproduces as nearly as possible the linear and angular motions that would be sensed by the pilot if he were to fly the helicopter for the same flight profile in actual flight.

An error in performing any of the above four tasks can lead to a misinterpretation of the results. This is particularly true when the issue is the subjective fidelity or "sense of realism" of the simulated atmospheric disturbances. As mentioned earlier, the problem is one of identifying or distinguishing the "parts from the sum." To illustrate the problem, if one is given only the sum of two real numbers, say $x + y = 5.0$, then it is not possible, based upon this information alone, to determine uniquely the values of individual numbers x and y . An infinitely large number of pairs (x_i, y_i) satisfies the given constraint. Thus, one could have an accurate wind model that would be rated poorly by the pilot because of deficiencies in (a) the way the wind model is integrated with the helicopter model, (b) the helicopter model, and (c) the motion drive simulation.

Many investigations focus only on one of the elements (e.g., wind model fidelity) in the overall closed-loop simulation. This can lead to conclusions which are erroneous because of errors in the simulation modules which are assumed to be correct. This may be the case with regard to the issue of whether or not patchy and intermittent turbulence characteristics are important and should be simulated to ensure a realistic wind simulation. It is felt that inadequacies in simulating other aspects of the flying task may have contributed to and exaggerated the importance of non-Gaussian turbulence characteristics in achieving simulation realism. Furthermore, the use of non-Gaussian turbulence models in simulations has yielded mixed results, with some studies⁵² showing that they gave an improved sense of realism to the simulation and others⁴⁰ showing no preference over the Gaussian models.

It should be noted that the military specifications for the flying qualities of both piloted airplanes and rotorcraft³⁵⁻³⁹ provide no specific guidelines with regard to the choice of Gaussian or non-Gaussian turbulence

models. Their only recommendation is to use a model that is "consistent with the objectives of the ground-based simulation and the fidelity of the total system representation." Unfortunately, this leaves a lot to be desired, since what is meant by "consistent with the objectives of the simulation" and "fidelity of the total system representation" is subject to interpretation by the person(s) responsible for the conduct of the simulation.

APPENDIX C

VISUAL SIMULATION

The "ideal" visual system simulation can be defined to be one that provides the pilot in a simulator cockpit the extra-cockpit visual scene that would be seen during actual flight. By definition, such an ideal system, if it can be built, would represent the ultimate degree of realism in visual cueing fidelity achievable in a ground-based (both objective and subjective) flight simulator. Unfortunately, duplicating the "exact" visual scene as seen by the pilot in actual flight is not practically feasible with current technology. One obvious approach to simulate the visual scene as seen by the pilot in an actual cockpit is to somehow record (or store) the scene continuously using a video camera (or equivalent image recording device) during flight for all possible flight profiles (i.e., trajectories, velocities and attitudes). The sequence of real-world images seen through each cockpit window can be stored in computer memory and could be replayed to generate the extra-cockpit scene corresponding to the simulated flight profile. However, this would impose a tremendous computational burden on the digital computer (memory storage and data retrieval requirements) for real-time piloted simulations. At best, a discrete set of extra-cockpit window scenes can be stored on a computer to minimize the storage requirements. Image interpolation and scene reconstruction algorithms may be used to generate the missing frames and create a continuous-looking extra-cockpit scene corresponding to the simulated flight profile. This latter approach may become economically and practically feasible in the future with anticipated advances in image processing algorithms and high-speed computers (e.g., VHSIC and fifth generation computers).

It should be noted, however, that this approach using recorded scenes was among the first to be tried in earlier visual simulations for constrained or limited scenarios during pilot training procedures. Even now, this method of visual scene generation provides a simple low-cost approach for locomotive and automobile simulations, where the vehicle path is restricted by virtue of the train tracks or roadway.

At the present time, two methods for visual scene generation are most prevalently used. They are: (1) the Terrain Model Board (TMB) system and (2) the Computer Generated Imagery (CGI) system.

The TMB system uses a camera mounted over a scaled model board for a given section of the earth terrain to present the pilot with a visual image of the outside world. The camera must be driven relative to the model in the same way as the aircraft moves relative to the real world, in order to create a realistic dynamic image of the outside world. Model boards as large as 2,000 square feet with terrain detail scale of 1500:1 are currently in use at various government (i.e., U.S. Air Force, NASA, etc.) and commercial (i.e. Boeing) facilities. For example, NASA's Ames Research Center has two terrain model boards (called Visual Flight Attachment, VFA-02 and VFA-07, respectively) in operational use.

The VFA-07 terrain model contains several different types of landing sites, all scaled at 600:1, including a CTOL runway, a STOL runway, and several VTOL or helicopter landing pads. There is also a 400:1 scale aircraft carrier that has pitch, roll and heave capabilities controlled by the digital computer.

The VFA-02 terrain model contains two different earth scenarios. One half of the board contains a color model of the area around a STOL port scaled at 600:1. The other half has a color model of the hill country near the Hunter-Liggett Army Base in California, at a scale of 400:1, thus making it more suitable for simulation of low-level helicopter operations.

The terrain board scene as seen by the camera is presented to the pilot on a single monitor through a collimating lens system that focuses the image at infinity. The central computer which solves the aircraft equations of motion performs additional calculations of where the pilot's eye point is relative to the earth and sends this information to the camera drive system. The camera, in turn, should follow the model board (in position and attitude) so as to match (except for scale) the pilot's eye point with respect to the outside world.

Improvements in modeling materials and lighting technology have made it possible to develop extremely sophisticated terrain model board systems. Furthermore, degradations in the visual scene caused by weather conditions, such as fog, rain or snow, can be superimposed on the camera image before presentation on the cockpit monitor.

However, in spite of the high level of sophistication achieved in building model boards, fundamental problems remain which preclude the extensive use of TMB systems for important helicopter flying tasks such as nap-of-the-earth, and decelerating approach to a hover. The problems arise because of the basic structure of the TMB system; namely, (a) the fixed scale (e.g., 600:1) of the terrain model and (b) the hardware limitations of the electromechanical servo-mechanism used to drive the camera relative to the board.

The fixed scaling of the terrain board defines the size of the earth segment and the level of detail that can be simulated for presentation to the pilot. A large scaling (e.g., 600:1) makes it possible to include a large portion of the earth's surface on a fixed size board (e.g., a 2000-square-foot board can accommodate 4.8 million square feet of earth terrain). However, for such a size board, the level of detail contained in the visual scene presented to the pilot is limited and not adequate for simulating low altitude helicopter flying tasks. This lack of scene detail is particularly apparent in the simulation of the visual scene following breakout at the IFR/VFR transition point (i.e., corresponding to decision heights of 50, 100, 150, and 200 feet prior to landing). The ability of the pilot to sense the aircraft's position and velocity (both translation and rotation) relative to the outside world is further compromised because of the narrow field-of-view provided by the single television monitor.

The problems caused by the limitations of the camera servomechanism drive system can be more serious. The purpose of the servo-drive system is to move the camera such that the camera motion in all six degrees of freedom follows accurately the position commands from the central digital computer. The ability of the servomechanism to perform this command following task can be affected by a number of factors including the design itself and other hardware constraints such as feedback potentiometer resolution, gear backlash, friction and servomotor limitations in the maximum accelerations, velocities, and displacements that can be produced. As a result, camera motion can be jerky and its position can lag a constant distance behind the commanded position, for constant velocity rate commands. This means that the visual scene presented on the cockpit monitor will lag behind what the pilot should actually see by a constant distance (or equivalent time) for a constant speed flight. This discrepancy can cause havoc in the simulation of low level flight-scenarios, such as the piloted simulator investigation of helicopter decelerating approaches to a hover under poor visibility conditions. In such a simulation, the pilot must fly a steep decelerating approach to a decision height (50, 100, 150 or 200 feet) under IFR conditions, and after transition to VFR conditions, bring the helicopter to a hover over the prescribed helipad. At decision height, because of position tracking errors in the camera servo system, the visual scene presented to the pilot could lag by as much as 0.33 seconds (i.e., an along track distance of 0.33 times the vehicle ground speed) behind what he should be actually seeing. If the pilot is unaware of this tracking error, it can lead him to substantially underestimate or overestimate the vehicle position and ground speed with respect to the helipad and to accept or reject a given IFR/VFR decelerating approach profile (i.e., trajectory, speed profile and decision height) for the wrong reasons.

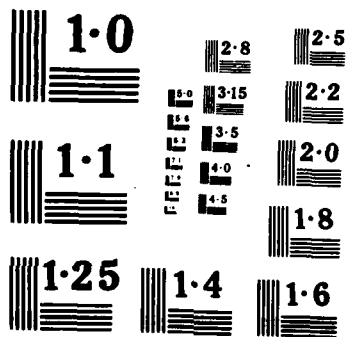
These problems can be ameliorated with proper design of the camera motion drive system; albeit at greater cost. Even if these improvements are made, the TMB system is limited to simulating scenarios already available on the terrain board. Much work and time is needed to create additional model boards for new scenarios. The CGI system developed in the early 70s, revolutionized the visual simulation industry, by promising an approach that is purely software based and independent of any hardware limitations (except computer hardware).

The basis of CGI is the modeling of geometric features using stored mathematical functions called edges. Edges are combine^d to form faces which can be further organized to form scenes. Efficient generation of complex shapes, such as trees, houses or rivers, can be accomplished by creating a library of such objects or cells. Additional scene characteristics such as color, contrast, brightness, texture and field-of-view can also be realized as needed.

The NASA-Ames Research Center employs a Singer-Link DIG1 computer-graphics system for use on the large amplitude Vertical Motion Simulator (VMS) system. Four windows are provided in the cab; the three primary windows are

AD-A169 947 TECHNICAL REQUIREMENTS FOR BENCHMARK SIMULATOR-BASED 2/2
TERMINAL INSTRUMENT. (U) ANALYTICAL MECHANICS
ASSOCIATES INC MOUNTAIN VIEW CA A V PHATAK ET AL.
UNCLASSIFIED MAY 86 AMA-86-2-1 NASA-CR-177407 NAS2-11973 F/G 17/7 NL





of the conventional 46° by 34° format, and the lower "Chin" window is 24° by 34° . Although, the CGI four window arrangement gives a vast improvement in the field of view as compared to the single-forward-window scene provided by the TMB system, considerable deficiencies still remain in the quality and realism of the computer generated scenery, primarily due to a non-optimum distribution of the field of view (i.e., window arrangement) and a severe dearth of near-field detail (i.e., resolution, contrast, texture gradients, etc.). These problems are further compounded by the presence of a large time delay (approximately 3 frames or 100 msec for a frame rate of 30 Hz) in the simulated scene which, as discussed earlier, can destroy the sense of realism or fidelity that the pilot may bestow to the "real-time" visual simulation.

However, it appears that improvements in computer-graphics and computer hardware technologies should be able to overcome the above problems and make it possible to generate any conceivable visual scenario without much difficulty. A considerable amount of effort would be necessary to validate such a visual simulation; that is, to accept the CGI visual simulation as the equivalent of the actual real-world scenario. The traditional approach based upon a pilot's subjective opinion or commentary should not be considered as sufficient to validate the computer-generated dynamic visual scene. Previous experience indicates that pilots are not able to identify sources of cue deficiency and in some cases can give the wrong or misleading commentary. An objective comparison of the CGI visual scene content against actual scene images should be conducted to ensure that the CGI imagery is a valid representation of the real-world scenario being simulated.

APPENDIX D

MOTION SIMULATION

The purpose of motion simulation is to provide the pilot on a ground-based simulator the sense of motion that would normally be present during actual flight. The simulator, being a ground-based facility must, of course, be constrained in its movement to stay within some finite airspace. Consequently, the motion of the simulated cockpit or cab cannot be identical to its counterpart in actual flight and must be modified such that the resulting motion cues perceived by the simulation pilot are as close to those sensed in natural flight.

The human pilot can perceive motion through cues (sensory feedback) sensed by the vestibular system, consisting of two special organs: (a) the Semicircular Canals for sensing the three angular velocity components and (b) the Otoliths for sensing the three translational accelerations (specific forces). Certain characteristics of these organs make it feasible to modify the actual motion on the simulator while attempting to maintain the perceived motion cues as near to real flight as possible. Known dynamic response characteristics of the vestibular system are described in terms of transfer function models as shown in Figure 41,⁵³ and may be summarized as follows:

- o The Semicircular Canals sense the angular velocities (in head coordinates) of motion above a threshold level of 0.03 rad/s, over the frequency range of $\omega_1 < \omega < \omega_2$ rad/s.
- o The Otoliths sense the specific forces (on the head) above a threshold level of 0.005g, over the frequency range $\omega > \omega_0$ rad/s.
- o Sensory signals or cues due to angular velocities and accelerations are "washed out" over a period of time and are not "sensed" (i.e., zero sensory signal) in the steady-state. This is because of the "washout" or "high-pass" filter structure of the transfer function models for the two organs.
- o The Otoliths sense specific forces. Hence the pilot is unable to distinguish between forces due to sustained acceleration and gravity.

The design of motion-drive systems for moving-base simulators take advantage of the above-mentioned vestibular properties and, in particular, of the washout filter characteristics of the two organs. Washout circuits are used to generate the linear acceleration and rotational velocity drive commands to the moving cab simulator. Tilting of the cab is implemented to provide the small low-frequency and steady-state components of linear accelerations.

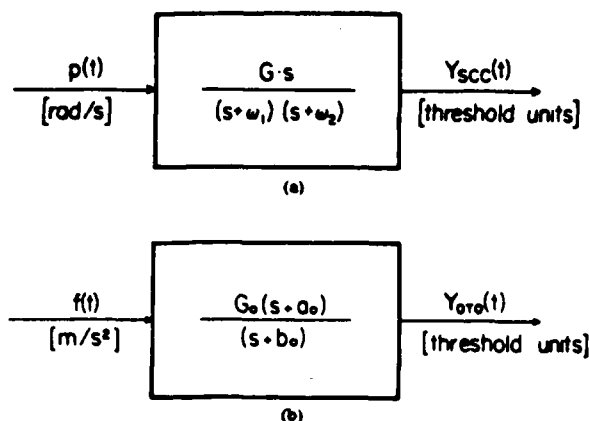


Figure 41. Transfer Function Model of Human Motion Sensing Organs

- a) Semicircular canal model. $p(t)$ is roll rate; $Y_{scc}(t)$ denotes the normalized firing rate. G is 7559 s/rad, ω_1 is 0.17 rad/s, ω_2 is 200 rad/s.
- b) Otolith model. $f(t)$ is specific force; $Y_{oto}(t)$ denotes the normalized firing rate. G_o is 2.16 s²/m, a_o is 0.076 rad/s, and b_o is 0.19 rad/s. [53]

The design of these filters, for the various motion axes of the simulator, is significantly complicated because of the coupling between translation and rotation. For example, sustained longitudinal and lateral specific forces can be achieved by tilting the cab; however, in order to keep the associated angular velocity below the detection threshold, the simulator must provide initial translational acceleration which is washed out with time as gravity begins providing the desired specific force. Using the same idea, a change in angular velocity should be accompanied by an initial translational acceleration which attempts to cancel the gravitational component resulting from the tilt angle. Thus the coupling between translation and rotation requires the design of coordinated washout filters.^{54,55} Most existing moving base simulators use coordinated washout filters to drive the motion system.

Modern simulators are equipped with a synergistic motion system (i.e., a system with as many actuators as degrees of freedom but where motion in each degree of freedom is achieved through a combination of actuator extensions) which provides six independent degrees of freedom; 3 rotational motions--pitch, roll, and yaw, and 3 translational motions--longitudinal, lateral and vertical. NASA's Vertical Motion Simulator (VMS) at Ames Research Center uses such a synergistic motion drive system, and was specifically designed to provide unusual fidelity of cockpit motion in the helicopter maneuvers associated with approach and landing, hover, and nap-of-the-earth tasks.

Two other types of motion systems currently in use are represented by designs such as the LAMARS (Large Amplitude Multi-Mode Aerospace Simulator)

located at Wright-Patterson Air Force Base and the DFS (Dynamic Flight Simulator) at the Naval Air Development Center. The LAMARS motion system consists of a thirty-foot long beam which is gimballed and driven by hydraulic actuators. From its horizontal position it can provide ± 10 degrees of vertical or lateral motion. The cockpit gimbal system mounted on the forward end of the beam provides angular rotation of ± 25 degrees in pitch, roll and yaw. The DFS motion drive system uses a human centrifuge cab mounted on a two-gimbal system at the far end of a 50-foot long arm, and is specifically tailored to simulate a broad range of transient (up to 10 g/s between 1.5g and 15g) and sustained multidirectional g-profiles.

However, because of the helicopter's unique flying capabilities, rotorcraft simulators must be able to reproduce the variety of motion cues that may not be present in fixed-wing aircraft. Simulators such as the VMS at NASA-Ames Research Center were built specifically for rotorcraft simulation scenarios and provide an ideal environment for studying the effects of motion cues on various helicopter terminal instrument procedures. Therefore, to serve as an example of what is needed, the capabilities of the VMS facility are described below.

The VMS cab, as shown in Figure 42, sits on a platform that is driven by two separate but complementary motion systems--a 6 degrees-of-freedom small motion system (SMS) for small rotational and translational motions, and a 2 degrees-of-freedom large-motion system (LMS) for large vertical and horizontal cab motions (longitudinal or lateral, depending upon the orientation of the cab). The simulator cab is mounted on the SMS which is used to provide the three rotational (pitch, roll and yaw) and one horizontal component of motion through the use of six hydraulic servo actuators. The two other translational motions are frozen and instead are provided by the LMS. The SMS is synergistic, since it achieves motion in any one degree-of-freedom through a combination of actuator extensions and nonlinear rotations (because the cab acceleration and angular velocity are nonlinear functions of the actuator positions, velocities and accelerations). The SMS is mounted on the LMS which has two degrees of freedom, horizontal and vertical. It consists of a horizontally-driven carriage along a beam which, in turn, can be moved vertically. Alternative orientations of the cab allow either fore-and-aft or lateral motion to be driven by the LMS. Table 13 lists the maximum displacement, velocity and acceleration limits of the VMS for each of the six degrees-of-freedom.

The VMS motion drive program is shown in Figure 43. The definitions of the variables and parameters used in Figure 43 are given in Table 14. The primary inputs from the aircraft simulation program are the body axes accelerations a_{xp} , a_{yp} , a_{zp} sensed by the pilot, and the aircraft body-axes rotational rates, p_b , q_b , r_b . These inputs are transformed to the simulator drive axes before they are used to drive the simulator motion servo-actuator.

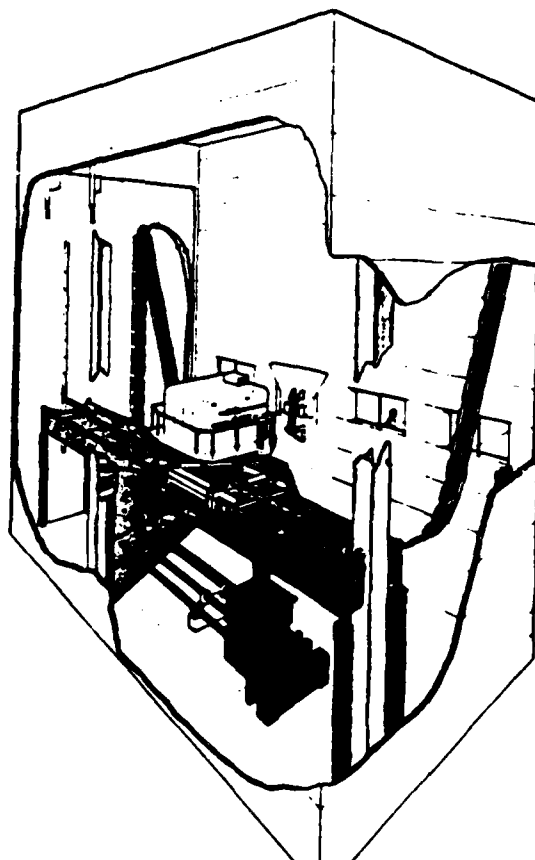


Figure 42. The VMS Simulator

As indicated in the block diagrams, the six simulator axes acceleration inputs \ddot{X}_{in} , \ddot{Y}_{in} , \ddot{Z}_{in} , \dot{P}_{in} , \dot{Q}_{in} , \dot{r}_{in} , are subjected to second order high pass "washout" filters of the form

$$\frac{\text{Simulator Acceleration}}{\text{Aircraft Acceleration}} = \frac{G.s^2}{s^2 + 2\zeta\omega s + \omega^2}$$

where G is the filter gain (≤ 1.0), ζ is the damping ratio (set at 0.7), ω is the break frequency, and s is the Laplace transform variable. The choices of the washout filter gains and break frequencies are dependent on the maneuver amplitudes in the simulated task. Two sets of parameters designated by the symbols F (fast) and S (slow) are defined in the motion drive program, and listed in Table 14. Below a given speed (or any other appropriate variable), defined as V_{WOL} , the 'S' values govern the output of the motion drive

$$\begin{bmatrix} p_b \\ q_b \\ r_b \end{bmatrix} = \begin{bmatrix} 1 & 0 & \theta_a \\ 0 & 1 & -\theta_a \\ 0 & \theta_a & 1 \end{bmatrix} \begin{bmatrix} p_{in} \\ q_{in} \\ r_{in} \end{bmatrix}$$

$$\begin{aligned} X_{in} &= a_{xp} - g * \theta_a \\ Y_{in} &= a_{yp} - Z_s * \theta_s \\ Z_{in} &= a_{zp} + g / \cos \theta_a \end{aligned}$$

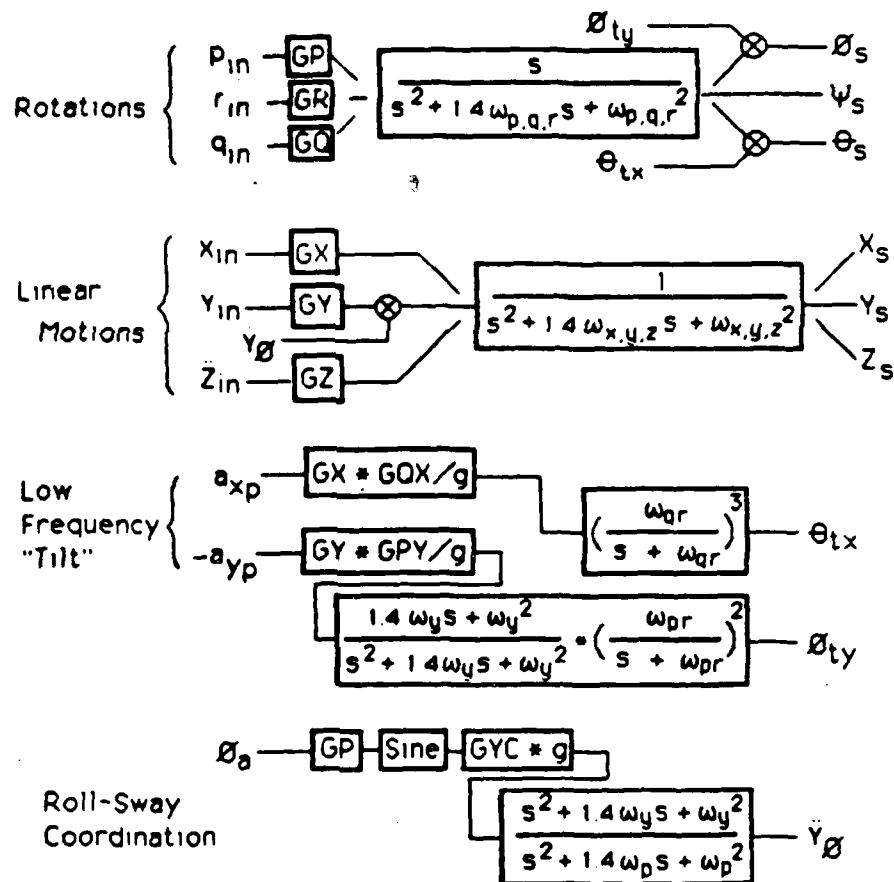


Figure 43. VMS Motion-Constraint or Washout Logic

Table 13. VMS Motion System Specifications [56]

Motion	Total Displacement	Maximum Velocity	Maximum Acceleration
LMS Horizontal	12.0 m	2.5 m/s	4.5 m/s ²
LMS Vertical	17.0 m	5.0 m/s	7.0 m/s ²
SMS Roll	40°	20 o/s	60.0 o/s ²
SMS Pitch	40°	20 o/s	60.0 o/s ²
SMS Yaw	40°	20 o/s	60.0 o/s ²
SMS Horizontal	1.0 m	-	-

logic, while for speeds above V_{WOF} , the 'F' values apply. Linear interpolation between the two sets applies between V_{WOL} and V_{WOF} . Thus, minimum motion constraints (i.e., low values of ω and G near unity) can be effected for low amplitude maneuvering during hover or landing, and motion constraints can be imposed for cruise flight conditions.

In establishing constraint parameter values, the objective is to reproduce faithfully as much of the vehicle motion spectrum as possible without unduly exercising the "hard" limits built into the linear motion logic. The two sets of parameter values given in Table 14 are meant to represent normal low speed and high speed flight conditions, and, as such, may not be optimum for individual simulation scenarios. If changes are warranted, the following rules-of-thumbs are recommended:

1. Attempt to maintain translational washout filter gains G_X or G_Y and G_Z to be no less than 0.6, constraining motion further when necessary by increasing the ω_x or ω_y and ω_z .
2. Try to maintain rotational ω 's at 0.5 or lower, never exceeding 0.8, and further constrain as necessary by reducing the G 's.
3. When pitch and roll responses of the cockpit are not accompanied by coordinating linear accelerations, it is desirable to constrain the angular motion to no more than six degrees.
4. If the benefits of the large vertical travel of the VMS are to be realized in precision vertical-longitudinal tasks, ω_z should be set at 0.3 or less.

Table 14. Definitions of VMS Motion Logic Variables

P_b	aircraft body-axis roll rate, rad/sec		
q_b	aircraft body-axis pitch rate, rad/sec		
r_b	aircraft body-axis yaw rate, rad/sec		
a_{xp}	pilot-perceived longitudinal acceleration, m/sec ²		
a_{yp}	pilot-perceived lateral acceleration, m/sec ²		
a_{zp}	pilot-perceived vertical acceleration, m/sec ²		
g	acceleration due to gravity, m/sec ²		
ϕ	roll attitude, rad		
θ	pitch attitude, rad		
ψ	yaw angle, rad		
θ_{tx}	pitch tilt to simulate a_{xp} , rad		
ϕ_{ty}	roll tilt to simulate a_{yp} , rad		
Y_ϕ	simulator lateral acceleration for roll coordination, m/sec ²		

Motion Logic Variables		Example Values	
		Low Speed (S)	High Speed (F)
GP	roll gain	0.7	0.3
GQ	pitch gain	0.5	0.5
GR	yaw gain	0.5	0.7
GX	longitudinal gain	0.5	0.5
GY	lateral gain	1.0	0.6
GZ	vertical gain	1.0	0.5
ω_p	roll washout frequency, rad/sec	0.5	0.7
ω_q	pitch washout frequency, rad/sec	0.5	0.5
ω_r	yaw washout frequency, rad/sec	0.4	0.6
ω_x	longitudinal washout frequency, rad/sec	3.0	3.0
ω_y	lateral washout frequency, rad/sec	0.4	0.5
ω_z	vertical washout frequency, rad/sec	0.2	0.6
GQX	pitch tilt gain	0.6	0.6
GPY	roll tilt gain	0.6	0.6
GYC	lateral-roll coordination ratio	1.0	1.0
ω_{qr}	pitch-tilt-lag-filter frequency, rad/sec	2.0	2.0
ω_{pr}	roll-tilt lag-filter frequency, rad/sec	3.0	3.0

APPENDIX E HELICOPTER DYNAMICS

Four types of mathematical models for the helicopter dynamics have been used in real-time, piloted, ground-based simulations. They are:

1. 6-DOF Linearized Model
2. 6-DOF Quasi-static Nonlinear Model
3. 9-DOF Tip-Path Plane Dynamics Nonlinear Model
4. Blade Element Rotor Dynamics Nonlinear Model

These models differ in their treatment of the rotor system as described below.

6-DOF Linearized Model

The 6-DOF linearized model is the simplest of all models and is based on a linearization of the full set of nonlinear equations of motion representing the helicopter dynamics, at the prescribed trimmed flight condition (i.e., constant airspeed V_0 , flight path angle γ_0 , etc.). However, such a model is only good for the prescribed flight condition (e.g., given airspeed) and can only be used for steady flight maneuvers such as a fixed-speed and constant flight path angle approach to a landing. For flight profiles requiring changing airspeeds and flight path angles, as in deceleration to a hover, the linearized model can be modified such that the model parameters (i.e., the linearized stability and control derivatives) are made functions of the vehicle airspeed and flight path angle. This can be achieved by: (1) determining the linearized models for several trimmed or "frozen point" flight conditions (i.e., airspeeds, flight path angles, etc.) along the reference flight path, and, (2) using interpolation methods with airspeed and flight path angle as independent variables to define the vehicle dynamics between two frozen point conditions. Such a mathematical model has been used at NASA/ARC⁵⁷ in a piloted simulator investigation of the effects of control system and display variations on an attack helicopter mission. Unfortunately, linearized models, by definition, are accurate only for small perturbations from the trimmed flight conditions, and can be easily misused. Substantial effort is needed to develop and validate such linearized models for selected reference flight profiles prior to their being used in a piloted simulation investigation.

6-DOF Quasi-Static Nonlinear Model

The 6-DOF quasi-static nonlinear helicopter simulation uses force and moment equations for the various components of the helicopter. The model employs a quasi-static main rotor representation, uniform inflow over the rotor disc, and simple expressions for the contributions of the fuselage, tail rotor, and empennage. Interference effects between components are not

represented. The body-axis forces and moments contributed by the fuselage aerodynamics model, the quasi-static main rotor model, the tail rotor model and the empennage model are summed to produce three aerodynamic forces and three aerodynamic moments acting at the helicopter's center of gravity. The quasi-static main rotor representation is based upon the assumptions that only the first harmonic motion of the rotor blades is important and that the blade coning and flapping angles are quasi-static. Because of these assumptions, rotor forces and moments depend only upon the body axes (translational and rotational velocities) and do not contribute additional main rotor degrees of freedom. Two such models have been developed for use on the NASA/ARC simulators: (1) a UH-1H model⁶ and (2) an SH-3G model.⁵⁸ Both of these models are adequate for constant-cruise speed (≥ 60 knots) flight conditions; however, use of these models for low speed flight including hover should be carefully scrutinized.

9-DOF Tip-Path Plane Model

Quasi-static rotor models do not explicitly account for dynamic effects of the rotor degrees of freedom, which can be important in non-steady helicopter maneuvers. The tip-path plane dynamics model for the helicopter⁵⁹ at NASA/ARC, describes the flapping dynamics (i.e., rotor forces and moments) of the main rotor in terms of three rotor degrees of freedom representing the blade coning angle and two blade flapping angles, respectively. The overall 9 DOF mathematical model (6 DOF rigid body dynamics and 3 DOF tip-path plane dynamics) includes several primary rotor design parameters such as flapping hinge restraint, flapping hinge offset, blade lock number, and pitch flap coupling. Therefore, this model provides a simplified rotor dynamics representation for use in real-time ground-based simulators with moderate computational speed and capacity.

Blade-Element Model

In this model, the main rotor dynamics are based on a blade element analysis in which total rotor forces and moments are developed from a combination of aerodynamic, mass and inertia loads acting on each simulated blade. Each blade is partitioned into a finite number of equal annuli area segments, which results in the minimum number of segments and distributes the segments toward the higher dynamic pressure areas.

The total forces acting on the blade are derived from the total acceleration and velocity components at the blade together with control inputs. Individual blade segment aerodynamic lift and drag forces are computed as a function of the local segment angle of attack and Mach number by using data stored in the form of "look-up" tables. Total rotor forces and moments are summed with the contributions of the other components at the vehicle center of gravity and integrated to determine the vehicle velocity and position.

The blade element model, if implemented properly, comes closest to describing the true dynamic characteristics of the helicopter. However, these models impose a heavy computational burden on present day computers, and some approximations are necessary for real-time piloted simulation applications. Compromises take the form of limits on the number of simulated blades and the allowable number of finite blade segments. Oversimplification should be avoided because the resulting blade element model could be worse than the simplified 9 DOF tip-path plane rotor model or even the 6-DOF quasi-static model. Blade element models based on the Sikorsky General Helicopter (GENHEL) simulation are being used on the Ames VMS for simulating the RSRA, the UH-60A and the X-Wing aircraft.⁶⁰

Discussion of Models

Among the four types of models described above, the selection of a given model would depend upon the specific helicopter flying task to be investigated. As a rule, the 6 DOF quasi-static model should be adequate for most non-decelerating helicopter tasks (e.g., constant airspeed approach to a landing). However, for low-speed operations such as deceleration to a hover or nap-of-the-earth flight, more accurate models such as the 9-DOF tip-path plane model or the blade element model are needed. These two types of models also allow for gradual penetration of the gust field (as opposed to instantaneous immersion in the quasi-static rotor models) which is extremely important at low airspeeds. Results by Dahl and Faulkner⁶¹ show significant differences in the vehicle response to the two types of gust penetration models. Consequently, the individual blade element or the 9 DOF tip-path plane rotor model with gradual gust penetration must be used whenever permissible.

APPENDIX F

PILOT MODELS FOR OFF-LINE TERPS EVALUATION

It has been strongly suggested in the past that models for the human pilot be used as part of an off-line model-based computer simulation for TERPS evaluation and operational enhancement. The ultimate goal would be to develop a pilot-model-based simulation tool and methodology for predicting closed-loop system performance (i.e., TSE, FTE, NSE), pilot workload and hence pilot opinion ratings during a prescribed helicopter terminal approach task. However, before this is possible, it is necessary to have developed and validated a pilot model that mimics the pilot's decision and control strategy during such terminal instrument procedures. A critical review of existing models for the human operator⁶² indicates that existing models for the human pilot are not suitable for describing pilot response behavior in realistic flying tasks--for example, during helicopter instrument and visual approach using raw data (i.e., standard cockpit instruments) alone, or raw data plus flight director guidance displays. At best, these models (e.g., the Quasi-linear Describing Function and Optimal Control Models) can be used as pseudo-autopilot substitutes for the human pilot during the troubleshooting and development period prior to the pilot-in-the-loop simulation experiments.

This does not imply that pilot models that are suitable for the helicopter instrument approach and landing task cannot be developed and validated. In order to do this properly, actual piloted simulation or flight test data obtained under realistic flight conditions must be used during the model development and validation process. Such an approach was attempted in a previous simulator investigation of helicopter IFR precision approach requirements,⁶³ the results of which show that a heuristic model for the pilot can be developed for the IFR approach scenario.

The best approach towards modeling pilot input-output behavior is to attempt to understand what the pilot actually does while performing a given flight task. Therefore, it is necessary to conduct systematic ground-based simulation and flight experiments for the specific TERPS piloting tasks. Data gathered from these experiments may then be used for developing and validating a cohesive pilot model structure and a model-based TERPS evaluation procedure.



REFERENCES

1. Peach, L. L., Bull, J. S., Anderson, D. J., Dugan, D. C., Ross, V. L., Hunting, A. W., Pate, D. P. and Savage, J. C., NASA/FAA Flight-Test Investigation of Helicopter MLS Approaches Preprint #80-55, American Helicopter Society 36th Annual Forum, Washington, D.C., May 1980.
2. Bjorkman, W. S., and Kidder, M. N., MLS Helicopter Approach Plots, Contract NAS2-10670 Report, Anal. Mechanics Assoc., Mountain View, CA, October 1982.
3. Swenson, H. N., Hamlin, J. R., and Wilson G. W., NASA/FAA Helicopter Microwave Landing System Curved Path Flight Test, NASA TM-85933, February 1984.
4. Phatak, A. V., and Lee, M. F., Navigation and Flight-Director Guidance for the NASA/FAA Helicopter MLS Curved Approach Flight Test Program, NASA CR-177350, May 1985.
5. White, J. S., NASA/FAA Curved Approach MLS Data Processing, AMA Report, #84-9, May 1984.
6. Talbot, P. D., and Corliss, L. D., A Mathematical Force and Moment Model of the UH1H Helicopter MLS Curved Approach Flight Test Program, NASA CR-177350, May, 1985.
7. Kayton, M. and Fried, W. R., Avionics Navigation Systems, Wiley, New York, 1969.
8. Savely, R. T., Navigation System Characteristics, JSC Note 72-FM-190, Johnson Space Center, Houston, TX, July 1973.
9. Anon., National Airspace System Plan - Facilities, Equipment, and Associated Development, Federal Aviation Administration, Washington, DC, April 1984.
10. Murphy, T. A., Realistic Localizer Courses for Aircraft Instrument Landing Simulators, NASA CR 172333, May 1984.
11. Hueschen, R. M., Microwave Landing System (MLS) Model for Advanced Cab Digital Simulation, ACF5-C358-SRD-016, Langley Research Center, Hampton, VA, Dec. 14, 1982.
12. Clark, W. F., Microwave Landing System Patterns and Paths, FAA/APM-403 Report, Federal Aviation Administration, Washington, DC, May 15, 1984.
13. Duff, W. G., and Guarino, C. R., Refinement and Validation of Two Digital Microwave Landing System (MLS) Theoretical Models, NASA CR-132713, Washington, DC, August 15, 1975.

14. Karmali, M. S., and Phatak, A. V., Analysis of MLS Range Navigation System Errors Using Flight Test Data, Report No. 82-19, Anal. Mechanics Assoc., Mountain View, CA, April 1982.
15. Steinmetz, G. G., and Bowles, R. L., Advanced Concepts Simulator Software Requirements - VOR/DME, ACFS-C358-SRD-015, NASA Langley Research Center, Hampton, VA, March 22, 1982.
16. Weseman, J. F., "Loran-C: Present and Future," Navigation, Vol. 29, No. 1, Spring 1982, pp. 7-21.
17. Frank, R. L., "Current Developments in Loran-C," Proceedings of the IEEE, Vol. 71, No. 10, October 1983, pp. 1127-1139.
18. Poppe, M. C., "The Loran-C Receiver, A Functional Description," Navigation, Vol. 29, No. 1, Spring 1982, pp. 56-68.
19. MacKenzie, F. D., "Certification of an Airborne Loran-C Navigation System," Navigation, Vol. 29, No. 1, Spring 1982, pp. 69-79.
20. Scalise, T. E., et al., West Coast Loran-C Flight Test, FAA-RD-80-28, Washington, DC, March 1980.
21. King, L. D., and McConkey, E. D., Alaska Loran-C Flight Test Evaluation, DOT-FAA-PM-83-4, Washington, DC, March 1983.
22. King, L. D., et al., Conus Loran-C Error Budget, DOT-FAA-PM-83-32, Washington, DC, December 1983.
23. Upton, H. W., et al., Investigation of Advanced Navigation and Guidance System Concepts for All-Weather Operations, NASA CR-166274, Washington, DC, September 1981.
24. Swanson, E. R., "Omega," Proceedings of the IEEE, Vol. 71, No. 10, October 1983, pp. 1140-1155.
25. Anon., Federal Radionavigation Plan, DOT-TSC-RSPA-84-8, Dept. of Transportation, Washington, DC, 1984.
26. King, L. D., and McConkey, E. D., Conus Omega/VLF Data Collection, DOT-FAA-PM-83-35, Washington, DC, December 1983.
27. Parkinson, B. W., and Gilbert, S. W., "NAVSTAR: Global Positioning System - Ten Years Later," Proceedings of the IEEE, Vol. 71, No. 10, October 1983, pp. 1177-1186.
28. Milliken, R. J., and Zoller, C. J., "Principle of Operation of NAVSTAR and System Characteristics," Navigation, Special Issue on GPS, Vol. 1, 1980.
29. Denaro, R. P. and Cabak, A. R., Simulation and Analysis of Differential Global Positioning System for Civil Helicopter Operations, NASA CR 166534, Washington, DC, December, 1983.

30. Beser, J., and Parkinson, B. W., The Application of Navstar Differential GPS to Civil Helicopter Operations, NASA CR 166169, Washington, DC, June 1981.
31. McCall, D. L., A Study of the Application of Differential Techniques to the Global Positioning System for a Helicopter Precision Approach, NASA CR 177326, Washington, DC, November 1984.
32. Edwards, F. G., and Loomis, P. V. W., "Civil Helicopter Flight Operations Using Differential GPS," Forty-First Annual Meeting of the Institute of Navigation, Annapolis, MD, June 1985.
33. Esposito, R. J., "Initial FAA Tests on the NAVSTAR GPS Z-Set," Navigation, Special Issue on GPS, Vol. 2, 1984.
34. Campbell, S. D., and LaFrey, R. R., "Flight Test Results for an Experimental GPS C/A-code Receiver in a General Aviation Aircraft," Navigation, Special Issue on GPS, Vol. 2, 1984.
35. Chalk, C. R., and Radford, R. C., Mission-Oriented Requirements for Updating MIL-H-8501, Calspan Proposed Structure and Rationale, USAAVSCOM TR-85-A-7, January 1984.
36. Anon Military Specification Flying Qualities of Piloted Airplanes, MIL-F-8785C, November 1980.
37. Moorhouse, D. J., Woodcock, R. J., Background Information and Users Guide for MIL-F-8785C, Military Specification - Flying Qualities of Piloted Airplanes, AFWAL-TR-81-3109, July 1982.
38. Hoh, R.H., et al., Proposed MIL STANDARD and Handbook - Flying Qualities of Air Vehicles, Vol. I. Proposed MIL Standard, Vol. II Proposed MIL Handbook, AFWAL-TR-82-3081, November 1982.
39. Anon Military Specification Helicopter Flying and Ground Handling Qualities; General Requirements For, MIL-H-8501A, 7 September 1961.
40. Reeves, P. M., Campbell, G. S., Ganzer, V. M. and Joppa, R. G., Development and Application of a Non-Gaussian Atmospheric Turbulence Model for Use in Flight Simulators, NASA CR-2451, September 1974.
41. Reeves, P. M., Joppa, R. G. and Ganzer, V. M., A Non-Gaussian Model of Continuous Atmospheric Turbulence for Use in Aircraft Design, NASA CR-2639, January 1976.
42. McCarthy, J. The JAWS Project, JAWS Interim Report for Third Year's Effort (FY-84) and Recent Reports from the JAWS Project, JAWS NCAR Report No. 01-85, October 1984.
43. Bray, R. S., A Method for Three-Dimensional Modeling of Wind-Shear Environments for Flight Simulator Applications, NASA TM-85969, July 1984

44. Tomlinson, B. N., Developments in the Simulation of Atmospheric Turbulence, Royal Aircraft Establishment Tech. Memorandum FS46, Flight Simulation/Guidance Systems Simulation, AGARD, CP-198, June 1976.
45. Phatak, A. V., Karmali, M. S., and Paulk, C. H., "Ship Motion Pattern Directed VTOL Letdown Guidance," 1983 American Control Conference, San Francisco, June 1983.
46. Reeves, P. M. A Non-Gaussian Turbulence Simulation, AFFDL-TR-69-67, December 1969.
47. Jansen, C. J., A Digital Turbulence Model for the NLR Moving-Base Flight Simulator, Part I, National Aerospace Laboratory Memorandum VS-77-024-U, August 1977.
48. Van de Moesdijk, G. A. J., Non-Gaussian Structure of the Simulated Turbulence Environment in Piloted Flight Simulation, Delft University of Technology Memorandum M-304, April 1978.
49. Jewell, W. F., Heffley, R. K., Clement, W. F., and West, T. C., Lt. Col., "Simulator Studies of Powered-Lift Aircraft Handling Qualities in the presence of Naturally-Occuring and Computer-Generated Atmospheric Disturbances," AIAA 78-1362, June 1978.
50. Jones, J. G., "Turbulence Models for the Assessment of Handling Qualities During Take-Off and Landing," AGARD Meeting on Handling Qualities Criteria, AGARD-CP-106, June 1972.
51. Jansen, C. J., "Non-Gaussian Atmospheric Turbulence Model for Flight Simulator Research," J. Aircraft, V. 19, No. 5, May 1982, AIAA 80-1568R, pp. 374-379.
52. Moorhouse, D. J. and Jenkins, M. W. M., "A Statistical Analysis of Pilot Control During a Simulation of STOL Landing Approaches," AIAA Paper No. 73-182, January 1973.
53. Ariel D. and Sivan R. "False Cue Reduction in Moving Flight-Simulators," IEEE Trans. on Systems, Mass & Cybernetics, Vol. SMC-14, No. 4, July/August 1984.
54. Schmidt, S. F. and Conrad, B., Motion Drive Signals for Piloted Flight Simulation. NASA CR-1601, May 1970.
55. Study of Techniques for Calculating Motion Drive Signals for Flight Simulation, NASA CR-114345, July 1971.
56. Bray, R. S., Visual and Motion Cueing in Helicopter Simulation, NASA TM-86818, September 1985.
57. Aiken, E. W., A Mathematical Representation of an Advanced Helicopter for Piloted Simulator Investigations of Control-System and Display Variations, NASA TM-81203, July 1980.

58. Phillips, J. D., Mathematical Model of the SH-3G Helicopter, NASA TM-84316, December 1982.
59. Chen, R. T. N., A Simplified Rotor System Mathematical Model for Piloted Flight Dynamics Simulation, NASA TM-78575, May 1979.
60. Howlett, J. J., UH-60A Black Hawk Engineering Simulation Program: Vol. I - Mathematical Model, NASA CR 166309, December 1981.
61. Dahl, H. J. and Faulkner, A. J., "Helicopter Simulation in Atmospheric Turbulence," *Vertica*, Vol. 3, pp. 65-78, 1979.
62. Phatak, A. V., Review of Model-Based Methods for Pilot Performance and Workload Assessment, AMA Report No. 83-7, April 1983 (Prepared under Contract No. NAS2-11318 for NASA/ARC).
63. Phatak, A. V., Analytical Methodology for Determination of Helicopter IFR Precision Approach Requirements, NASA CR-152367, July 1980.

END

DT/C

8-86